LIQUID WATER TRANSPORT IN POLYMERIC FILMS AND MEMBRANES

A Dissertation

by

MELISSA CRUZ SANTOS

Submitted to the Office of Graduate and Professional Studies of
Texas A&M University
in partial fulfillment of the requirements for the degree of

DOCTOR OF PHILOSOPHY

Chair of Committee,	Yossef A. Elabd
Committee Members,	Jodie L. Lutkenhaus
	Micah J. Green
	Jaime C. Grunlan
Head of Department,	M. Nazmul Karim

May 2017

Major Subject: Chemical Engineering

ABSTRACT

Accurately measuring and understanding transport mechanisms of liquids in polymers is important for the development of materials used in applications such as packaging, water purification, and corrosion protection.

In this work, an *in situ* pressure-contact Fourier transform infrared attenuated total reflectance (FTIR-ATR) spectroscopy apparatus was designed and developed for accurately measuring liquid water transport in free-standing polymer films. This new technique allows time-resolved infrared data of liquid transport in free-standing films to be collected accurately without solution casting the film directly onto the ATR element. Liquid transport in a rubbery polymer, glassy polymer, and a crosslinked polymer was measured and compared using this technique. The *in situ* pressure-contact FTIR-ATR spectroscopy apparatus showed similar results to those obtained using the conventional solution-cast FTIR-ATR apparatus for the rubbery polymer. Liquid water diffusion in the rubbery polymer exhibited non-Fickian behavior. Non-Fickian behavior was observed for the glassy polymer which was attributed to diffusion-relaxation and difference between the conventional solution-cast FTIR-ATR apparatus and the pressure-contact apparatus. Liquid water diffusion in the crosslinked polymer exhibited Fickian behavior and was attributed to the suppressed polymer strain response to the diffusant.

Diffusion in glassy polymers can be difficult to measure because of their nonequilibrium nature (*i.e.*, T_g, of the polymer is much higher than the experimental

temperature. In this work, the effect of glass transition temperature, T_g, on liquid water diffusion behavior in polymer-ionic liquid (IL) mixtures was investigated. Liquid water transport in glassy polymer-ionic liquid mixtures of varying IL content (0 to 50 w/w % IL) was studied to determine the effect of changing the glass transition temperature, T_g, on diffusion behavior. The results of this study showed that as IL content increased and T_g decreased, the liquid water diffusion behavior became more Fickian. This is because as T_g decreases, the free volume of the polymer increases, and the polymer approaches equilibrium.

Liquid water transport in polymers is also important for separations applications such as water purification. Recent research has focused on a promising hybrid technology, reactive electrochemical membranes (REMs) which act both as a membrane and a reactive electrochemical surface for the electrochemical degradation of pollutants However, they are limited by morphology, and therefore conductive REMs with tailored porosities are needed. In this study porous, flexible reactive electrochemical membranes (REMs) for water purification were synthesized by a novel simultaneous electrospinning/electrospraying (E/E) technique. The fabricated E/E REMs were durable, highly porous, and conductive membranes, performing comparably to carbon nanotube flow-through reactors, which are among the highest performing in literature. Further studies exploring the use of FTIR-ATR spectroscopy for CO_2 separations studies, and for studying surface interactions of membranes fabricated via simultaneous E/E will be discussed.

ACKNOWLEDGEMENTS

First and foremost I would like to thank my advisor, Dr. Yossef Elabd for the opportunity to work with his research group for the past five years. His knowledge, constant guidance, encouragement, and mentorship, has made all of this possible. He has challenged me to grow as a scientist and researcher. I would also like to thank the members of the Elabd Research Group, both past and present for all of their help and support. I thank the members of my dissertation committee for taking the time to meet and review my work. I also thank my collaborators for their work on various projects. Lastly, I would like to thank my family and my friends for their never ending encouragement and support.

CONTRIBUTORS AND FUNDING SOURCES

Contributors

This work was supervised by a dissertation committee consisting of Professor Yossef Elabd, Professor Jodie Lutkenhaus, and Professor Micah Green of the Department of Chemical Engineering, and Professor Jaime Grunlan of the Department of Mechanical Engineering.

The crosslinked polymer samples in Chapter 2 were provided by Beverly Bendikson of PPG Coatings Innovation Center. The differential scanning calorimetry (DSC) experiments in Chapter 3 were conducted by Rui Sun (Elabd Research Group) of the Department of Chemical Engineering. The membrane filtration studies and electrochemical experiments in Chapter 4 were conducted by Professor Brian Chaplin and his student Yin Jing of the Department of Chemical Engineering at the University of Illinois, Chicago, and Lei Fan of the College of Civil Engineering and Architecture at Zheijang University, and were published in 2015.

All other work conducted for this dissertation was completed by the student independently.

Funding Sources

Graduate study was supported in part by the U.S. Army Research Laboratory under Grant W911NF-13-2-0046 and by the financial support of the National Science Foundation (1447172). The FE-SEM acquisition was supported by the NSF grant DBI-0116835, the VP for Research Office, and the TX Eng. Exp. Station.

TABLE OF CONTENTS

Page

LIST OF FIGURES

Page

LIST OF TABLES

Page

CHAPTER I

INTRODUCTION

The diffusion of small molecules in polymers is of interest for a variety of applications such as coatings, [1-2] packaging,[3-4] desalination,[5-6] drug delivery[7-8], contact lenses,[2, 8] and fuel cells.[9] Accurately measuring and understanding transport mechanisms in polymer films and membranes is important for the development of materials used for these applications.

More specifically, the diffusion of liquids (*i.e.*, sorption kinetics) in free-standing polymer films is of interest for many applications such as coatings,[1-2] packaging,[3-4] and contact lenses.[2, 8] However, accurately measuring liquid transport in free-standing polymer films is not well understood because of limited studies demonstrating the accurate measurement of liquid transport in free-standing films and technical limitations of current methods to measure transport in free-standing films. Therefore, techniques that can accurately measure the diffusion of liquids in free-standing polymer films of different chemistries would be desirable for optimal material design of products. In this work, a technique to accurately measure liquid water diffusion in free-standing polymer films was designed and developed. Liquid water diffusion in free-standing polymer films of both rubbery and glassy polymers was explored. Results obtained using this technique was compared to results obtained with traditional methods used for measuring liquid transport in free-standing films.

A fundamental understanding of transport mechanisms of liquids in glassy polymers was also explored. Liquid diffusion in glassy polymers can be complex due to their nonequilibrium nature (*e.g.,* glass transition temperature is much higher relative to the experimental temperature). This work aimed to understand transport mechanisms of liquid water in glassy polymers on a molecular level. Additionally, since the nonequilibrium nature of glassy polymers is due to the fact that their glass transition temperature is much higher relative to the experimental temperature, changing the glass transition temperature *via* the addition of ionic liquid to glassy polymers was explored. Liquid water diffusion in polymer-ionic liquid mixtures was studied to determine the effect of glass transition temperature on liquid water diffusion behavior.

Liquid transport in polymer membranes is also important for the development of materials and products for separations applications, such as water purification.[10] Multiple technologies in a treatment train are usually required to effectively treat a broad range of water contaminants.[11] In order to reduce the cost and complexity of water treatment, the development of novel technologies that can incorporate multiple treatment methods into a single technology is needed.[11] Reactive electrochemical membranes (REMs) are a promising hybrid technology, which act both as a membrane and a reactive electrochemical surface for the electrochemical degradation of pollutants. While past studies on REM performance have demonstrated their potential use for wastewater purification, one of the limitations of this technology is the rigid morphology of the REM.[12-13] To expand the potential REM, fabrication of flexible REMs with tailored porosities is desired. This research in this dissertation focused on the demonstration of

the use of simultaneous electrospinning/electrospraying for the fabrication of flexible, durable, and highly conductive reactive electrochemical membranes (REMs) for water purification.

In this dissertation, measuring and understanding transport mechanisms in polymer films and membranes, and the development of polymer membranes for water purification was investigated. The following sections provide a review of previous work on transport of liquid water in polymer films and membranes, as well as an overview of the work in this dissertation.

1.1. Liquid Transport in Free-Standing Polymer Films

Liquid transport in polymers is primarily important for the development of materials for a variety of applications[1-5, 8-9, 14]However, there are limited studies demonstrating accurate measurement of liquid transport in free-standing polymer films.[15-16] Unlike transport experiments for polymers that involve gases or vapors as diffusants, conventional gravimetric techniques that measure the diffusion of liquids in solid state polymers (*e.g.*, films) typically involves an *ex situ* pat-and-weigh technique that can possess low sensitivity and high experimental error.[17] This gravimetric experiment typically consists of submerging a free-standing polymer film into the liquid, manually removing the film, blotting excess liquid from the surface of the film, weighing the film, re-submerging the film in the liquid, and then repeating this process multiple times to collect gravimetric data as a function of time (*i.e.*, sorption kinetic data). [15, 17] In order to collect accurate early-time data, this sequence must be repeated many times over a short

time interval. Equilibrium sorption is determined by the long time steady state value of the amount of water sorbed by the film. Figure 1.1 shows the liquid sorption kinetics of water in a free-standing film of poly(lactide) (PLA).[15] While the data appears to be adequately described by the Fickian model (solid line), the inset in the graph, which highlights the early time data, demonstrates the difficulty in obtaining accurate sorption data using this gravimetric technique. Figure 1.1 highlights the low sensitivity and high experimental error of this *ex situ* technique, especially when attempting to collect many data points over a short time interval.[15, 17] This *ex situ* gravimetric technique can introduce significant error when attempting to collect accurate early-time data when diffusion is fast, the film is thin, the mass of the film is low, or the sorption of the liquid is low. Additionally, another disadvantage of this technique is the lack of detailed information (molecular phenomena) about the diffusion process. Other techniques that have been used to measure diffusion in polymers, include laser interferometry, ellipsometry, inverse gas chromatography (IGC), NMR imaging, Rutherford backscattering spectrometry (RBS), forward recoil spectrometry (FRS), elastic recoil detection (ERD), various microscopic techniques, and light scattering techniques.[18-19] However, most of these techniques are expensive, are difficult to operate and cannot monitor the diffusion process directly and/or continuously.[18-19] Therefore, facile techniques that can accurately measure the diffusion of liquids in free-standing polymer films would be desirable for optimal design of many products and processes.

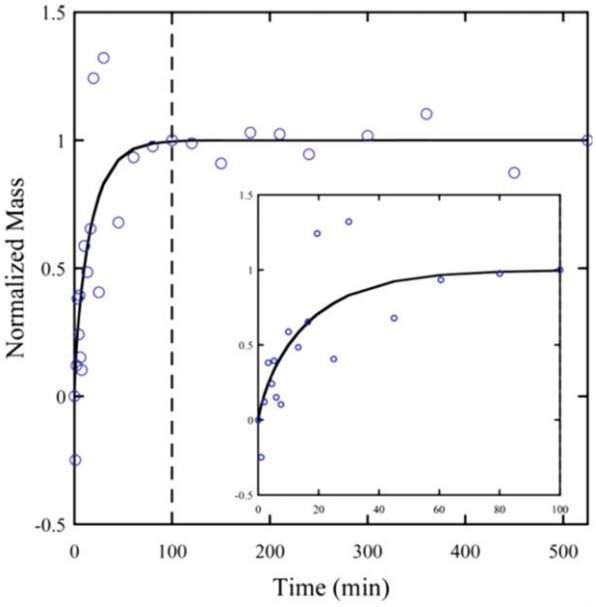

Figure 1.1 Liquid water sorption kinetics (gravimetry) in PLA 4032D film at ~25 °C, where the solid line represents a regression to the Fickian model. The inset is a magnified view of the early time data (first 100 min). Figure adapted from ref. [15].

1.1.1 Time-Resolved FTIR-ATR Spectroscopy for Adhered Films

One technique that can accurately measure the diffusion of liquids in polymers is time-resolved Fourier transform infrared-attenuated total reflection (FTIR-ATR) spectroscopy.[19] Time-resolved Fourier transform infrared-attenuated total reflectance (FTIR-ATR) spectroscopy is a highly sensitive, noninvasive, *in situ* technique that has been used frequently in literature to accurately measure the diffusion of liquids in polymers. FTIR-ATR spectroscopy has the ability to accurately measure diffusion in polymers because traditionally polymers are solution-cast onto the surface of the ATR element. This adhesion creates intimate contact between the polymer and crystal, allowing for the accurate collection of time-resolved infrared data. FTIR-ATR

spectroscopy differentiates itself from other conventional techniques in that it provides molecular level contrast between diffusant(s) and polymer in real time.[17, 19-20] This technique can be used to capture phenomena such as multicomponent diffusion, polymer relaxation, and polymer-penetrant interactions.[15, 17, 19-23]

A schematic of a conventional multibounce ZnSe FTIR-ATR apparatus is shown in Figure 1.2. In the illustration shown in Figure 1.2, an IR beam travels from the IR source, is modulated by an interferometer, and enters the ZnSe crystal at a 45° angle. It is internally totally internally reflected multiple times before it exits on the opposite side of the ZnSe crystal and is quantified by a detector.[19] At the interface between the ATR element and the polymer, an exponentially decaying electromagnetic wave is propagated into the polymer. This electromagnetic wave is called the evanescent wave (shown in Figure 1.2). At this interface, the IR absorbance of chemical bonds associated with the polymer and the diffusant(s) are measured *via* the evanescent wave.

In order to measure diffusion (*i.e.*, sorption kinetics) in a polymer film, a polymer film is first solution cast and annealed onto the ATR element. The diffusant(s) are then introduced directly on top of the solution-cast film (opposite the polymer-crystal interface). Diffusion is measured *via* the continuous collection of spectra at frequent intervals at the interface between the solution-cast polymer and the ATR element (in the evanescent wave region also referred to as the depth of penetration) over a specified period of time. The continuous collection of molecular data allows for the accurate collection of early time data and information on sorption kinetics of a diffusant in a polymer film on a molecular level.

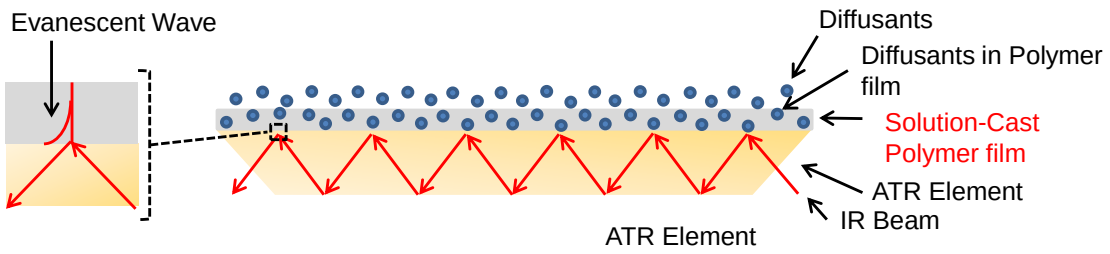

Figure 1.2 Schematic of FTIR-ATR apparatus.

An example of data from Elabd *et al.*[21] of time-resolved FTIR-ATR spectroscopy is shown in Figure 1.3. Figure 1.3a shows the infrared spectra of methyl ethyl ketone (MEK)/butanol (BOH) liquid mixture (0.5 mole fraction) diffusing into a poly(isobutylene) (PIB) film that was solution cast onto the ATR crystal. The figure shows that as time increases, the infrared spectra of the C=O region (associated with MEK) increases as well.

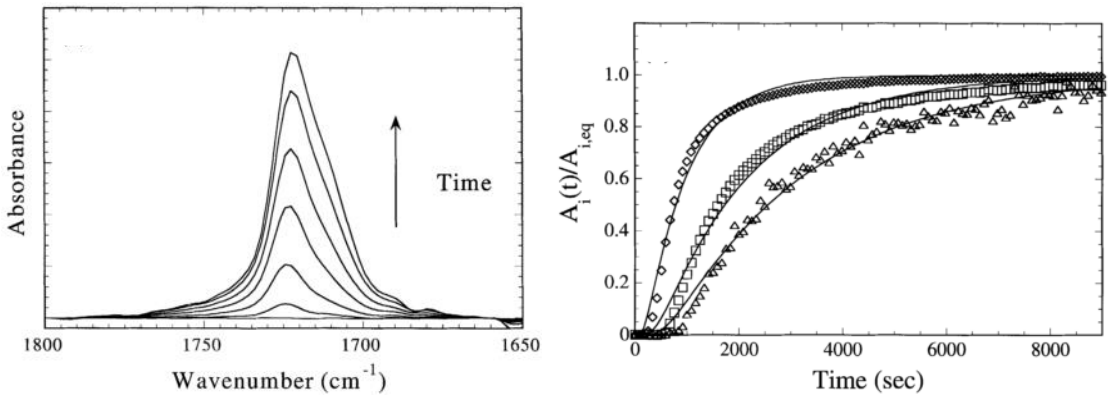

Figure 1.3 (a) Time resolved carbonyl (C=O) absorbance spectra associated with MEK for 0.5:0.5 mole fraction methyl ethyl ketone (MEK):butanol (BOH) in poly(isobutylene) (PIB) and (b) MEK , 1722 cm^{-1} (◊), BOH cluster, 3330 cm^{-1} (Δ), and MEK-BOH complex, 1711 cm^{-1} (□) regressed to the Fickian model (solid line). Figure adapted from ref. [21].

Figure 1.3b shows the time-resolved normalized absorbance for MEK, BOH cluster and MEK-BOH complex in PIB. The solid line represents a regression to the Fickian model for the determination of diffusion coefficients. Comparing the data shown in Figure 1.3b to the data in Figure 1.1 demonstrates the accuracy in data collection (especially early-time kinetic data) achieved using FTIR-ATR spectroscopy. The data in Figure 1.3 also demonstrates the ability of FTIR-ATR spectroscopy to measure diffusion on a molecular level and hence measure multicomponent diffusion of liquid mixtures in polymer films.

Traditionally time-resolved FTIR-ATR spectroscopy experiments rely on polymers to be solution-cast onto the surface of the ATR element. The adhesion between the polymer film and the ATR element generated during the solution casting/annealing process creates intimate contact between the polymer and crystal for accurate collection of time-resolved infrared data. This technique is therefore traditionally limited to polymers that can be solution-cast onto the surface of the ATR element. Accurate measurements of

liquid diffusion in free-standing commercially available or pre-fabricated polymer films that cannot be solution-cast onto an ATR element is of interest for a variety of industrial applications, and therefore, a technique that can accurately measure liquid diffusion in free-standing polymer films without directly solution casting the film onto the ATR element is highly desired.[24-25]

1.1.2 Time-Resolved FTIR-ATR Spectroscopy for Free-Standing Films.

Several studies have attempted to explore using FTIR-ATR spectroscopy to study liquid transport in free-standing films.[25-28] Yi *et al.*[25, 27] studied liquid water and acetone diffusion in free-standing films of poly(propylene) using FTIR-ATR spectroscopy and used the pressure of the penetrant fluid (pumped at a high flow rate) to create the intimate contact between the polymer and ATR element.[27] The schematic of the ATR flow cell they used is shown in Figure 1.4.[27] The penetrant fluid (liquid diffusant) was continuously pumped through the flow cell, and the pressure of the penetrant fluid was used to create the intimate polymer-crystal contact usually provided by adhering or solution casting the polymer film to the ATR element. The results of their work demonstrated the need to maintain and control adequate pressure of the penetrant fluid to achieve accurate absorption of chemical bonds associated with the polymer and the liquid diffusants.

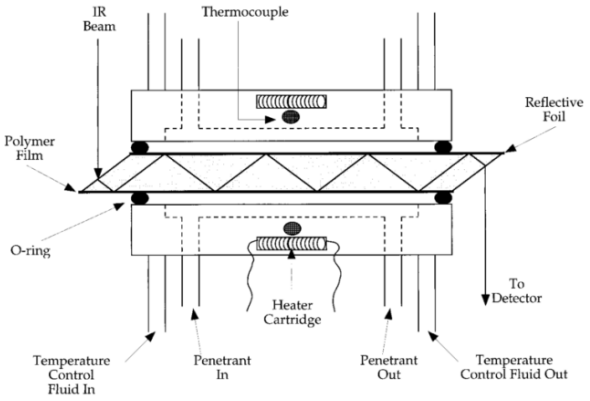

Figure 1.4 Schematic of ATR flow cell. Figure adapted from ref. [27].

Balik *et al.*[28] studied gas and liquid diffusion in free-standing films of high density poly(ethylene) (HDPE), low density poly(ethylene) (LDPE), and poly(styrene) (PS). Using the ATR diffusion cell shown in Figure 1.5, diffusion of CO_2 in PS, and liquid amyl acetate and limonene in HDPE and LDPE were studied. Similar to the ATR cell used by Yi *et al.*,[25, 27] the pressure of the liquid penetrant/diffusant fluid was used to maintain the intimate contact between the ATR element and the free-standing polymer film. For gas diffusion experiments, pressurized gas in a sealed chamber above the ATR cell was used to maintain the intimate contact between the ATR element and the free-standing film.[28] They compared their results to those obtained with gravimetry. It is important to note that although they studied diffusion of liquid amyl acetate in HDPE, they were only able to compare their results to acyl acetate vapor diffusion in HDPE (gravimetry), demonstrating the lack of methods to accurately measure liquid transport in free-standing polymer films. Their work demonstrated the importance of exerting

pressure on the free-standing polymer film in order to create the intimate polymer-crystal contact usually obtained *via* solution casting.

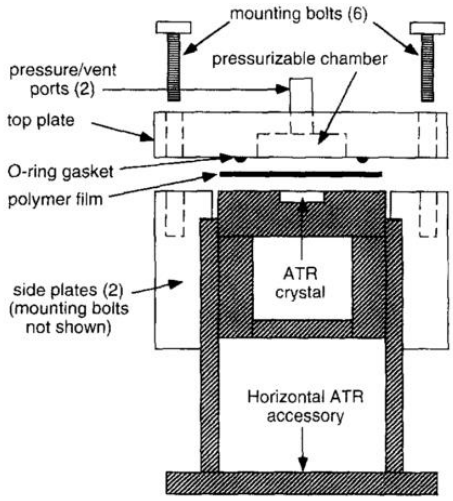

Figure 1.5 End view of horizontal ATR accessory, where the infrared beam is perpendicular to the plane of the paper. Figure adapted from ref. [28].

Wang *et al.*[26] studied liquid water diffusion in a low density poly(ethylene) (LDPE) free-standing film using FTIR-ATR spectroscopy and two-dimensional correlation analysis. The LDPE film was placed between the ATR element and a piece of filter paper saturated with water. It is unclear how intimate contact between the polymer film and the ATR element was generated in this study.[26] While these studies[25-28] have shown the possibility of accurately measuring liquid transport in free-standing polymer films using FTIR-ATR spectroscopy, to date, no studies have compared their data with those obtained with conventional solution-cast FTIR-ATR spectroscopy. Additionally, these studies have mainly focused on transport in glassy polymers. Although several previous

studies have explored FTIR-ATR spectroscopy to study liquid diffusion in free-standing films, to our knowledge, studies have not been conducted comparing liquid diffusion in solution-cast and free-standing polymer films using FTIR-ATR spectroscopy.

1.2 Transport Behavior in Glassy Polymers

Glassy polymers are characterized as being in a nonequilibrium state because the glass transition temperature, T_g, of the polymer is much higher than the experimental temperature. Due to their nonequilibrium nature, water sorption in glassy polymers results in time-dependent relaxation and anomalous diffusion behavior, which can be difficult to measure and quantify.[29-30] Understanding the molecular interactions between diffusants and glassy polymers would aid in the development of materials for applications such as packaging[3-4] and fuel cells.[9] Glassy polymers have limited chain mobility and free volume due to the pseudo-frozen state of the polymer chains.[31] Transport in glassy polymers is more complex compared to that in rubbery polymers due to their nonequilibrium nature.[31] Figure 1.6 shows a schematic of the polymer specific volume plotted as a function of temperature, illustrating the nonequilibrium nature of glassy polymers.[32]

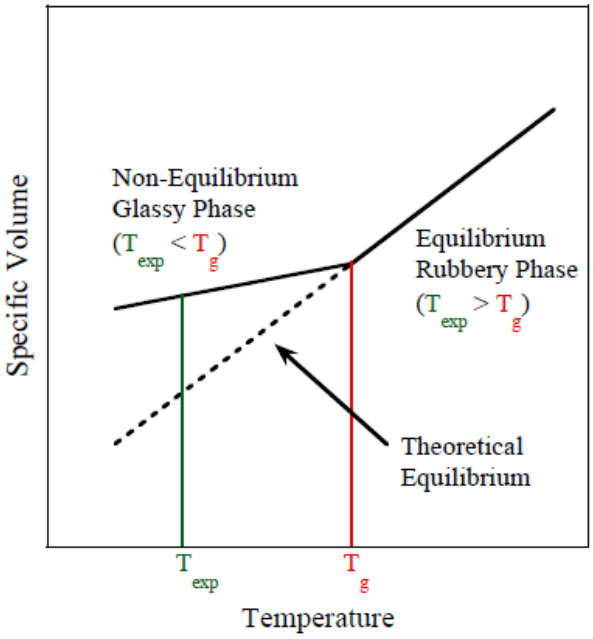

Figure 1.6 Schematic diagram of polymer specific volume plotted as a function of temperature. T_g and T_{exp} refer to the glass transition temperature and experimental temperature, respectively. Figure adapted from ref. [32-33].

Relaxation of the polymer volume is a fast process when the polymer in an equilibrium state (*i.e.*, rubbery phase; at a temperature above the T_g).[33] The instantaneous response to an imposed stress (mechanical or chemical), usually corresponds to an observed Fickian diffusion in the polymer. However, when a polymer is cooled below its T_g, the specific volume deviates from the theoretical equilibrium, and the polymer chains are left in a pseudo-frozen (nonequilibrium) state.[33] Therefore, unlike a rubbery polymer, the specific volume of the polymer is not constant, but is a function of time, and an instantaneous response to an external stress is not observed. [33] Since the nonequilibrium nature of the glassy phase results in a time-dependent relaxation process of the polymer volume, the diffusion of small molecules is often observed to be non-Fickian, or

anomalous.[34] This means that diffusion in a glassy polymer is dictated by both a concentration gradient and time-dependent polymer relaxation.

1.2.1 Water Sorption in Glassy Polymers

Gravimetric studies on the diffusion of liquid water in poly(methyl methacrylate) (PMMA) showed non-Fickian behavior.[35] The anomalous behavior observed was attributed to time-dependent long relaxation times of the polymer.[35] Stannett *et al.*[36-37] studied water vapor diffusion in poly(acrylonitrile) (PAN) films *via* gravimetry. They concluded that the observed non-Fickian behavior was due to time-dependent polymer relaxation and water clustering. These early studies highlight the effect that nonequilibrium nature of glassy polymers has on non-Fickian or anomalous transport.

Hallinan *et al.*[23, 38] used FTIR-ATR spectroscopy to study water vapor sorption in Nafion. Integral sorption experiments, which consisted of changing the vapor activity from 0% to a specific value (*i.e.*, 100% RH) were conducted. Results from integral sorption experiments when the value was changed from 0% to 100% RH showed a fast initial uptake of water, followed by a slower, gradual uptake of water over longer experimental times. The time-dependent relaxation behavior was eliminated by conducting differential sorption experiments, which consisted of changing the vapor activity in smaller steps (*i.e.*, 20 to 40 % RH). Results from differential sorption experiments showed that the stress imposed by water on the Nafion membrane was much smaller during these small step changes in humidity compared to the large changes in humidity for the integral sorption experiments. Figure 1.7 shows a plot of the

normalized absorbance of the O-H stretching band for water vapor diffusion in Nafion. As seen in Figure 1.7, the water vapor diffusion was Fickian for each water vapor activity, except 100% RH. Due to the large integral sorption step, the stress imposed by the water at 100% RH, was significant enough to induce relaxation in the polymer chains. The stress imposed by water vapor at 100% RH led to non-Fickian diffusion, which has also been observed by other studies on water diffusion in Nafion.[39-40]

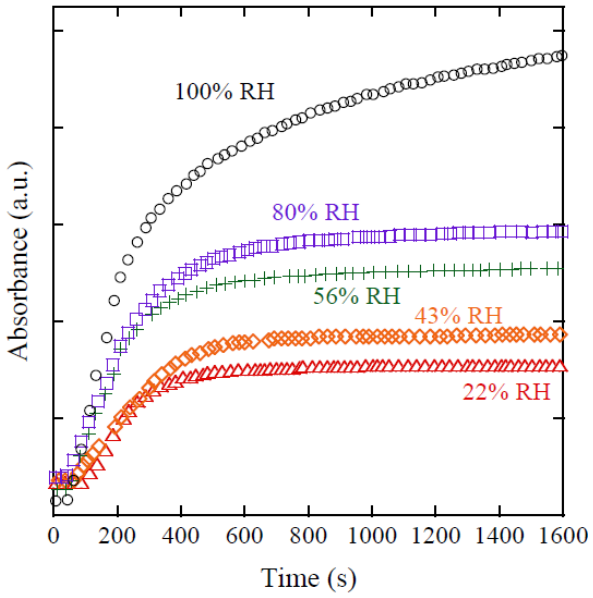

Figure 1.7 Time-resolved absorbance of the water O-H band during water vapor diffusion in Nafion. Each experiment started from dry conditions (0 % RH) to a relative humidity of 22 % (Δ), 43 % RH (◊), 56 % (+), 80 % (□), and 100 % (○). Figure adapted from ref. [38].

Davis *et al.*[41] also observed anomalous diffusion for water vapor sorption in poly(lactide) (PLA) using FTIR-ATR spectroscopy. Figure 1.8 shows that the water sorption kinetics in PLA at 35 °C in response to an external differential change in water vapor activity of 0.54 to 0.75 exhibits anomalous diffusion. While similar anomalous

diffusion behavior has been observed by other investigators,[30, 42-43] for the water diffusion behavior shown in Figure 1.8, two phenomena are observed. These phenomena occur over two distinct time periods over the entire experimental time and this is referred to as two-stage sorption kinetics. The inset in Figure 1.8 shows that at early times, Fickian-like or pseudo-Fickian behavior is observed. This can be regressed to Fick's second law to obtain a diffusion coefficient for this first period of time. However at longer experimental times, the glassy polymer relaxes due to its nonequilibrium state, with more water diffusing gradually over time.

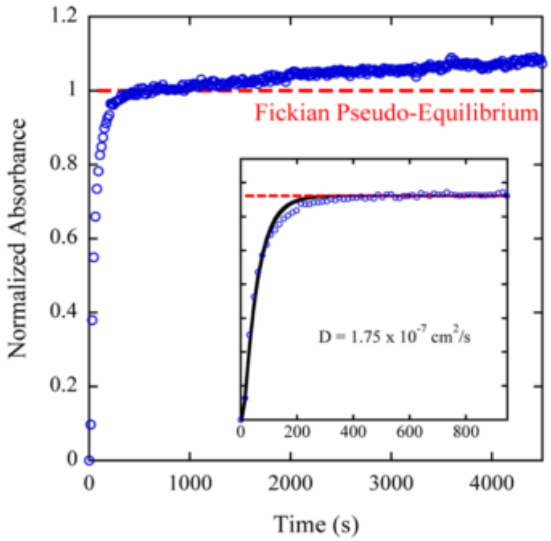

Figure 1.8 Water vapor sorption kinetics in PLA at 35 ˚C measured with time-resolved FTIR-ATR spectroscopy in response to an external differential change in water vapor activity of 0.54 to 0.75. The inset corresponds to a magnified view of the early time data, where the solid line corresponds to a regression to the solution to Fick's second law. The dashed lines correspond to pseudoequilibrium values. Figure adapted from ref. [41].

Davis *et al.*[44] also observed anomalous behavior for water vapor sorption in PMMA. As shown in Figure 1.9a, the O-H stretching region of water in PMMA (*ca.* 3000 and 3700 cm^{-1}) increases broadly with time. Additionally, they observed the presence of two bands for the water dimer (*ca.* 3450 cm^{-1} and *ca.* 3350 cm^{-1}), indicating self-associated hydrogen-bonded water clusters.[44-45] At higher water vapor activities, they observed that a broader infrared band was present between *ca.* 3100 and 3350 cm^{-1}, confirming the presence of larger, hydrogen-bonded water clusters.[44, 46] The water clustering that occurs during water vapor diffusion in PMMA can affect water sorption kinetics. Figure 1.9b shows the water sorption kinetics in PMMA at 35 °C *via* quartz spring microbalance (QSM), where the black line indicates a regression to Fick's second law. Water diffusion in PMMA has previously been observed to be non-Fickian or two-stage, the diffusion of water in PMMA shown in Figure 1.9b is Fickian. The data can appear Fickian if the time scale of the sorption step is fast in reference to the polymer film thickness. At longer experimental times, two-stage kinetics would be observed.

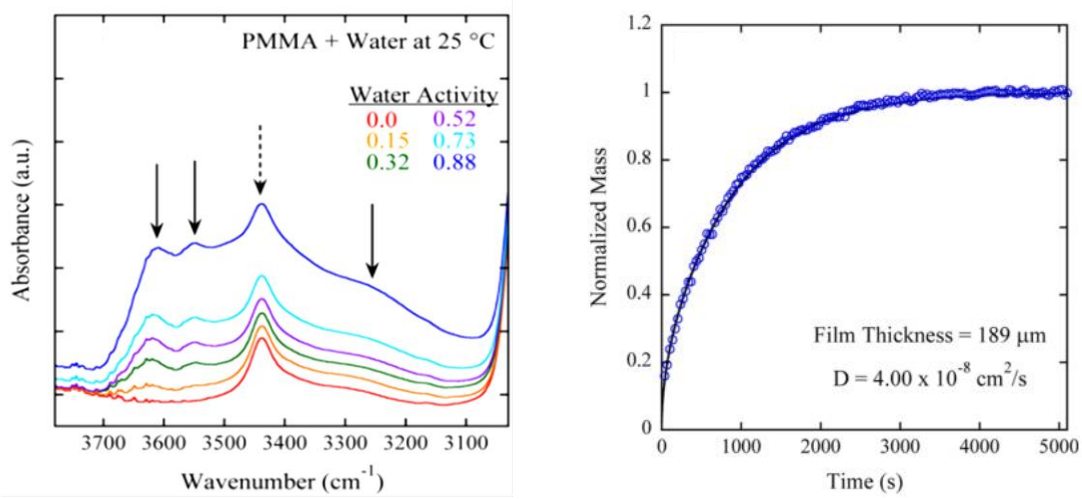

Figure 1.9 (a) FTIR-ATR spectra of the O-H stretching region of water in PMMA (25 ˚C), and (b) water sorption kinetics (quartz spring microbalance (QSM)) in PMMA at 35 C in response to an external differential water vapor activity step change of 0.11 – 0.33. The solid black line represents a regression of the experimental data to Fick's second law. Figure adapted from ref. [44].

The anomalous diffusion behavior observed in glassy polymers is indicative of the fact that diffusion in a glassy polymer is dictated by both a concentration gradient and time-dependent polymer relaxation. In order to reconcile the two phenomena, Reiner[47] introduced the Deborah number, a dimensionless number that relates the time of relaxation, τ_R, to the time of observation (or the time of diffusion), τ_D, to describe the rheological behavior of solids and fluids (eq 1.1).

$$De = \frac{\tau_R}{\tau_D} \tag{1.1}$$

Vrentas and Duda[43, 48] used the Deborah number to characterize the anomalous diffusion behavior observed with glassy polymers, where the polymer-solvent system is described as a system of two viscous fluids, and polymers are viscoelastic fluids. τ_R, the

characteristic time of the polymer, or the relaxation time of the polymer is a quantity that is constant for a given material regardless of thickness.[41] τ_D, the diffusion time, is calculated using eq 1.2:[15, 49]

$$\tau_D = \frac{L^2}{D} \tag{1.2}$$

where L^2 is the polymer film thickness and D is the diffusion coefficient of a solvent in the polymer film. Unlike τ_R, τ_D can change as L changes. When the Deborah number is small (De <<1), polymer relaxation occurs instantaneously relative to diffusion. Polymer relaxation is much faster than diffusion, making diffusion behavior essentially Fickian. When De >>1, the diffusion time is much smaller than the polymer relaxation time. This means that the time of observation, or the diffusion time, is much smaller than the polymer relaxation time, causing Fickian behavior to be observed.[33, 49] When De ≈1, polymer relaxation and diffusion occur on similar time scales, where solvent movement and rearrangement of polymer chains occur simultaneously.[49] This simultaneous diffusion and time-dependent relaxation behavior is referred to as anomalous or non-Fickian diffusion behavior. Understanding the coupled phenomenon of diffusion and polymer relaxation is critical to more accurately measuring and quantifying water diffusion in glassy polymers.

1.2.2 Liquid Water Sorption in PMMA

While many studies have explored gas and vapor sorption in polymer films of varying composition and thickness, there are limited studies on liquid sorption in glassy polymer

films. Understanding liquid diffusion in glassy polymers is critical for the development of materials for various products and processes. Liquid water diffusion in PMMA primarily is of importance for transport applications such as contact lenses.[2, 8] As mentioned previously, Davis *et al.*[44] studied water vapor sorption in PMMA, and observed pseudo Fickian behavior at short experimental times. They acknowledged that water clustering may influence water sorption kinetics.

Goodelle *et al.*[16] investigated liquid water and water vapor sorption in PMMA films of varying thicknesses using fluorescent rotor probe. They observed that at early stages of the experiment, water vapor sorption in PMMA exhibited Fickian behavior, but deviated from Fickian behavior at late stages of the experiment. Additionally, with the exception of the thinnest film studied (3 μm), they observed that water vapor diffusion data collapsed onto the same curve. This agrees with water vapor sorption behavior observed by Davis *et al.*[41] and their studies on water vapor sorption in PLA. However, when they analyzed the data for liquid water sorption and plotted the data versus time normalized by length squared (t/L^2), they observed that the liquid water diffusion data did not collapse onto the same curve (Figure 1.10a). Additionally, they calculated diffusion coefficients and observed that calculated diffusion coefficients were not the same regardless of thickness (Figure 1.10b). These results are surprising, because diffusion is dependent on a concentration gradient, and not film thickness. However, Goodelle *et al.* [16] were not able to determine why liquid water diffusion in PMMA films of varying thicknesses exhibits this behavior.

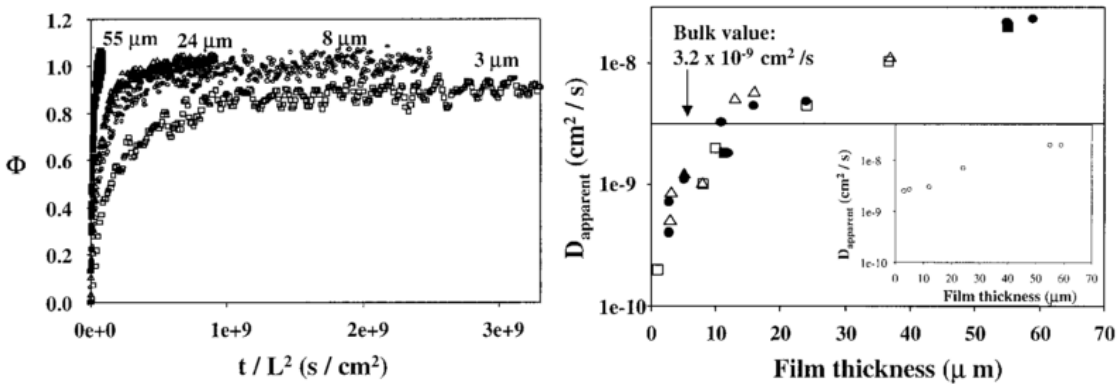

(a) (b)

Figure 1.10 (a) Liquid water sorption kinetics in PMMA films of various thicknesses plotted versus time normalized by length squared (t/L^2), and (b) Fickian diffusion coefficients fit to water sorption kinetic data, where the solid black circles correspond to liquid water diffusion coefficients. Figure adapted from ref. [16].

In order to elucidate the transport mechanisms of liquid water in PMMA, Sundfors *et al.*[50] studied liquid water sorption in copolymers of methyl methacrylate with n-butyl acrylate, decyl acrylate and isodecyl acrylate using FTIR-ATR spectroscopy. They studied liquid water diffusion in PMMA/poly(isodecyl acrylate) (PIDA) at two different film thicknesses, 80 and 324 µm. Figure 1.11a shows the infrared spectra of the O-H stretching region for water in PMMA/PIDA, where the spectra increases with increasing time. Figure 1.11b shows a plot of the experimental data for water diffusion (indicated by the solid line) plotted versus time. To describe the sorption kinetics, they attempted to deconvolute the peaks under the O-H stretching region in order to derive fast and slow diffusion data and coefficients. Figure 1.11b shows the mathematically derived fast (•) and slow (■) diffusion data, along with the sum (Δ) plotted with the experimental data.

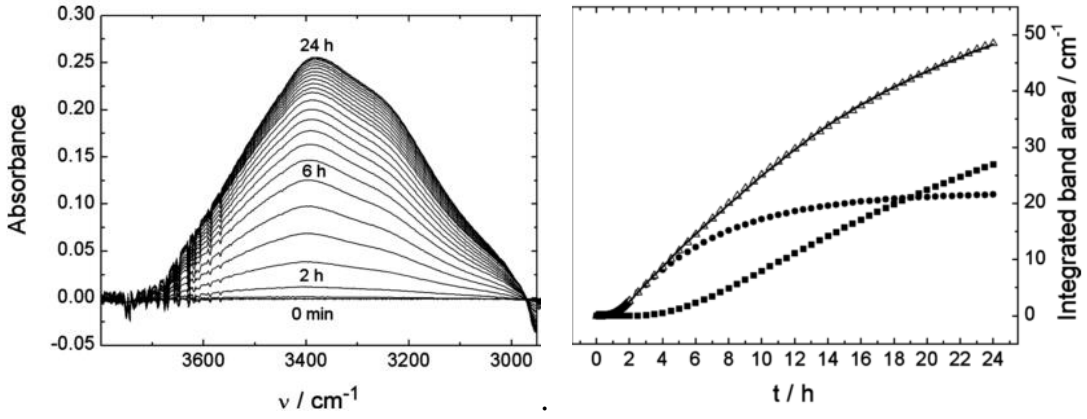

(a) (b)

Figure 1.11 (a) FTIR-ATR spectra of the O-H stretching region in PMMA:PIDA (b) Liquid water sorption kinetics, where the solid line indicates experimental data. Mathematically simulated fast (•) and slow (■) diffusion, and their sum (Δ) are also plotted. Figure adapted from ref. [50].

While they observed that the diffusion coefficients obtained for fast diffusion were the same for both film thicknesses (80 and 324 μm), the diffusion coefficients obtained for slow diffusion for both film thicknesses were not the same. This indicates the unique nature of liquid water as a diffusant, and the need to better understand liquid diffusion of water in glassy polymer films.

1.2.3 Effect of Ionic Liquid (IL) on the Glass Transition Temperature of Polymers and Subsequent Impact on Transport

The nonequilibrium nature of glassy polymers is attributed to the fact that the glass transition temperature, T_g, is much higher relative to the experimental temperature, leading to anomalous, or non-Fickian diffusion. Since the T_g has a direct effect on

diffusion behavior, understanding how T_g affects diffusion (sorption kinetics) can lead to a better understanding of diffusion behavior in glassy polymers. One way to examine the effect of different T_gs on diffusion behavior is to add ionic liquid (IL) to a glassy polymer, because the addition of IL to a glassy polymer can lower its T_g. Research has focused on the use of ILs because their unique physiochemical properties make them attractive for applications, such as supercapacitors, solar cells, fuel cells, sensors, and membranes for gas separations.[51-56] Gwee *et al.*[57] studied the effect of T_g on ion transport in polymer-IL mixtures. Ionic conductivity was low at low IL content because of the presence of the polymer, but at high IL content, ionic conductivity approaches that of that bulk IL.[57] However, plasticization of the polymer results from increasing IL content.[57] This is because as IL content increases, the T_g decreases, causing the polymer-IL mixture to transition from a glassy to a rubbery mixture. Figure 1.12a shows a plot of the glass transition temperatures of PMMA-IL versus the mole ratio of IL to MMA, demonstrating that a IL content increases, the T_g decreases.[57] Gwee *et al.*[57] found that there was a sharp increase in conductivity in polymer-IL mixtures that contained approximately 0.15 mol ratio IL (Figure 1.12b). As shown in Figure 1.12a, the T_g of this polymer-IL mixture is at room temperature, which was the temperature of the conductivity experiments. The significant increase in conductivity for the PMMA-IL mixtures is due to the transition from a glassy to a rubbery state where the free volume and segmental motion of the PMMA chains increases, impacting transport.

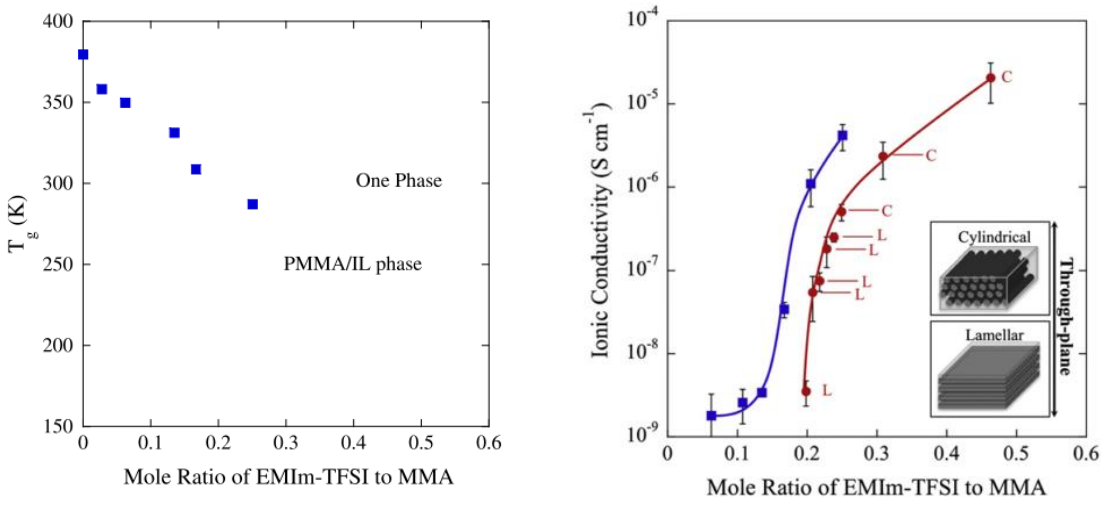

(a) (b)

Figure 1.12 (a) Glass transition temperatures of PMMA-IL (IL = EMIm-TFSI) cast from dimethylacetamide (DMAc) and annealed for 2 days at 110 °C. (b) Through plane conductivity of PMMA-IL (■) and toluene-cast poly(styrene-b-MMA)-IL (●) films at room temperature as a function of IL to MMA mole ratio. The two insets show schematics of the two idealized block copolymer morphologies and the direction of measured ion transport. The labels C and L represent cylindrical, and lamellar morphologies, respectively. The solid lines are trend lines to help guide the eye. Figure adapted from ref. [57].

In addition to impacting ion transport, ILs in polymer-IL mixtures have also impacted water transport properties.[58] Magana *et al.*[58] studied the impact of imidazolium tetrafluoroborate ILs on the water vapor transport properties of Pebax copolymer. They observed that the T_g of the Pebax-IL films decreased with increasing IL content, however every T_g observed was well below the experimental temperature (25 °C), indicating that every Pebax-IL mixture was not in the glassy state. Figure 1.13 shows the water sorption isotherms of the Pebax-IL (IL = EMIm-BF_4) films, where water sorption increase as IL content in the Pebax-IL films increases.[58] The increase in water sorption is

due to the fact that as IL increases, T_g decreases, causing the Pebax-IL mixture to approach an equilibrium state (*i.e.*, rubbery phase) where the free volume and segmental motion of the Pebax chains increases, facilitating increased water transport.

The effect of water vapor on ionic liquid materials and water vapor uptake in ionic liquid materials has been explored in literature.[53, 55, 58-62] However, understanding the molecular interactions between water and polymer mixtures of varying T_gs would be of interest for the development of materials for various applications. [26] Both of these studies highlight the effect that T_g has on polymer morphology and transport of small molecules in glassy polymer-ionic liquid mixtures. Although these studies examined small molecule transport in polymer-ionic liquid mixtures, and understanding of the molecular changes and diffusant/polymer interactions that occur as T_g changes would be important for the development of materials for applications such as membranes for gas (*i.e.*, CO_2) separations. [55-56]

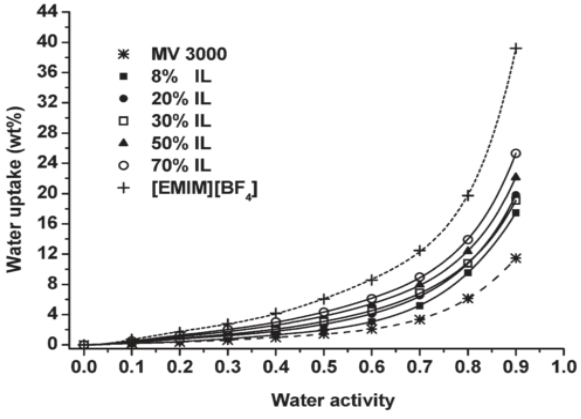

Figure 1.13 Water sorption isotherms of Pebax-IL films. Figure adapted from ref. [58].

1.3 Reactive Electrochemical Membranes (REMs) for Water Purification

Effective treatment methods are needed to combat the increasing range of contaminants in water.[11] Recent research has focused on finding an innovative solution *via* membrane filtration and electrochemical methods for the removal of contaminants from water.[63] Increased industrial activity in the last 50 years has contributed to the increase in contamination of water sources, namely with organic pollutants. [63] Organic pollutants are a major environmental concern because they must all be removed or degraded into non-toxic compounds.[63-64] Efforts to reduce water pollution include restrictions and legislation to reduce industrial effluents and reclamation of water *via* wastewater treatment plants.[63] Wastewater treatment mainly involves three main stages: primary, secondary and tertiary treatment. Primary and secondary treatments are mainly concerned with the removal of particulates, sludge and suspended biological matter. Current tertiary treatment methods to treat organic pollutants in industrial wastewater, include sedimentation, coagulation, flocculation, sludge treatments, and membrane filtration and oxidation and reduction processes.[63-65] Recently, membrane filtration combined with electrochemical advanced oxidation processes (EAOP) has been explored to create a hybrid technology known as reactive electrochemical membranes (REMs).[12-13] REMs serve both as a membrane for filtration, but also as a reactive electrochemical surface (anode) that can oxidize contaminants *via* water oxidation (eq 1.3) to produce hydroxyl radicals ($OH^{\bullet}$).[12-13] A direct electron transfer reaction (eq 1.4) also occurs on the anode surface where an electron is transferred from the contaminant (R) to the anode.[12-13]

$$H_2O \rightarrow OH^{\bullet} + H^{+} + e^{-} \quad (1.3)$$

$$R \rightarrow (R^{\bullet})^{+} + e^{-} \quad (1.4)$$

Traditional methods for integrated membrane and EAOP processes involve parallel plate reactors where water diffuses between the anode and cathode (Figure 1.14a).[66] However, reaction rates are dependent on the 100 µm boundary layer that develops at the electrode surface. Additionally, this configuration only provides modest increases in oxidation. Early studies done by Sharifian and Kirk[67] and De Sucre and Watkinson[68] studied oxidation of phenol using PbO_2 packed bed reactor anodes. De Sucre and Watkinson focused on the effects of different parameters, such as current density, initial phenol concentration, and anode particle size on phenol oxidation and total organic carbon (TOC) removal.[68] Sharifian and Kirk focused on characterizing phenol oxidation by monitoring three byproducts, p-benzoquinone, maleic acid, and CO_2.[67] Both studies used divided cell experiments, where the anode and cathode are separated by a conductive membrane. An anolyte solution, consisting of a salt, phenol and water is pumped into the anodic side into the divided cell. On the cathodic side of the divided cell, a catholyte solution, consisting of a salt (same as the anolyte) and water is pumped into the cathodic side and into the divided cell. A potential is applied and the effluent is pumped out of the divided cell, and is either analyzed or recycled back into the cell.

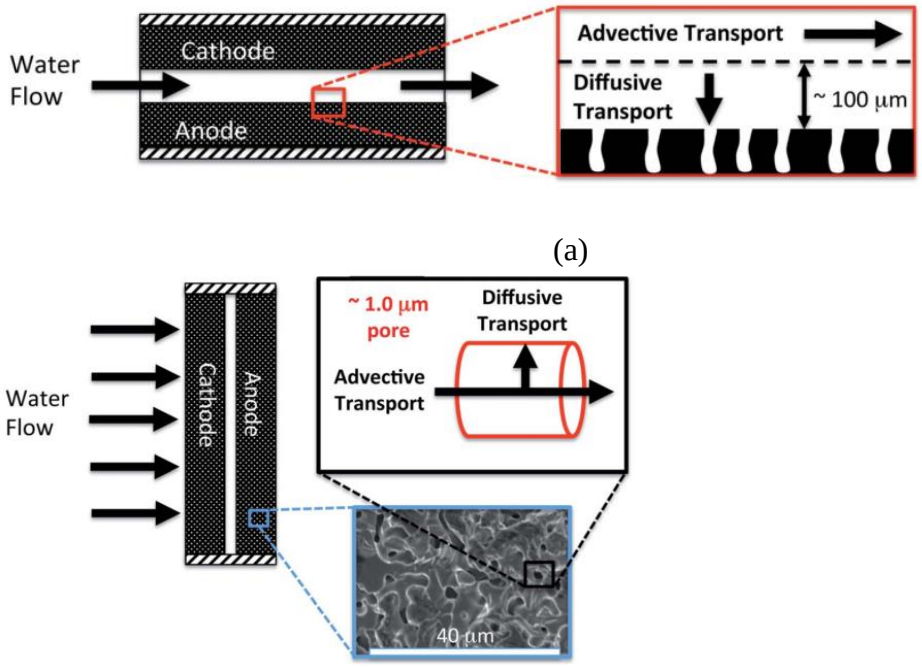

Figure 1.14. Schematic of a (a) traditional flow-by apparatus, where water flows through 100 µm thick diffusion zone, where the inset shows the diffusion zone, and (b) flow-through operation apparatus where water diffuses radially through 1 µm pores. Inset shows SEM image of porous Ti_4O_7 REM and magnified pore image. Figure adapted from ref. [66].

In order to overcome diffusional limitations, a flow-through apparatus has been explored where water diffuses through the cathode and anode (Figure 1.14b).[66] Murphy *et al.*[69] implemented a membrane configuration that allowed feed to flow through both the anode and the cathode. Murphy and coworkers used a proton exchange membrane (PEM) reactor apparatus, where a Nafion 117 membrane was sandwiched between platinum electrodes and titanium current collectors. [69] Their results show that a higher current density allowed for oxidation of organic compounds that are often difficult to degrade. Based on their studies they recommended further studies on the reaction rates

of phenol oxidation, and increasing energy efficiency by using highly porous electrocatalysts that are electroactive for oxidation of phenols. They discussed other potential metal oxides that such as SnO_2 and mixtures of Ti_4O_7 and Ti_5O_9. [69]

Yang *et al.*[65, 70] used a TiO_2/carbon membrane as an electrocatalytic membrane reactor (ECMR) to reduce membrane fouling and water purification. Membrane performance was assessed using oily wastewater. The anode allowed for the production of hydroxyl radicals via electrolysis, which helped to decompose the organic contaminants directly into CO_2 and H_2O. The electrolysis created both gas and liquid microflows that prevented contaminants from adsorbing onto the membrane, and the electrocatalytic activity of the anode directly degraded the organic foulants into CO_2 and H_2O. They observed that at low permeate fluxes, longer residence times were achieved, leading to full degradation of contaminants, demonstrating the synergistic effect of combining membrane filtration with electrocatalytic oxidation processes. [65, 70]

However, the main challenges for oxidation *via* REM are the selection of an anode material and ensuring that the resulting products are harmless and biodegradable. Recently there has been increased interest in Ti_4O_7 and past studies on Ti_4O_7 include applications for the oxygen reduction reaction for zinc-air rechargeable batteries[71-72] and PEM fuel cells.[73] Ti_4O_7 is also known by its trademark name, Ebonex®. This material was discovered in the early 1980s.[74] It was developed when researchers put TiO_2 rods in H_2 at approximately 1000 °C for a few hours. The resulting product was a dark blue ceramic that was electrically conductive, with a conductivity value between 10^2 and 10^3 S/cm.[74] However, it is a very brittle material, and it is difficult to manufacture large

sheet forms of Ti_4O_7.[74] Usually Ti_4O_7 is often modified with other metals, such as Ru and Pt as a support to increase stability.[74] In addition, there are few literature studies on Ti_4O_7 because it competes with lead alloy anodes, which are much more stable and common in electrochemical reaction studies.[74] The renewed interest in Ti_4O_7 is due to its high conductivity and its resistance to oxidation and corrosion. [71-74] Furthermore, the use of Ti_4O_7 for batteries, fuel cells, or electrochemical membranes is cost effective because TiO_2, the precursor for Ti_4O_7, is inexpensive. It is these characteristics of Ti_4O_7 that make it an excellent candidate as an anode material for electrochemical membranes for water purification.

Zaky and Chaplin[12-13] explored the use of Ti_4O_7 as a REM material for water purification. Figure 1.15 shows a schematic of the Ti_4O_7 REM that they used. The REM was operated in cross-flow filtration mode, where the feed water was pumped through the REM, allowing for $OH^{\bullet}$ generation and direct electron transfer between the anode and the contaminant molecules. They studied the removal of *p*-methoxyphenol as a model organic contaminant. They demonstrated that the Ti_4O_7 REM was active for direct anodic oxidation and $OH^{\bullet}$ generation for the efficient degradation and removal of phenolic compounds. However, due to its rigid cylindrical structure, the Ti_4O_7 REM had a limited morphology and therefore a more flexible but durable and highly conductive REM was needed. REMs with tailored porosities and morphologies greatly expands their potential applications for water treatment. Although studies have explored the use of different materials for REMs, there are limited studies that demonstrate the fabrication of REMs with tailored porosities and morphologies. Additionally, there are limited studies

on REMs of different materials and morphologies which can perform comparably with carbon nanotube flow through reactors, which are among the highest performing in literature. [75,76-77]

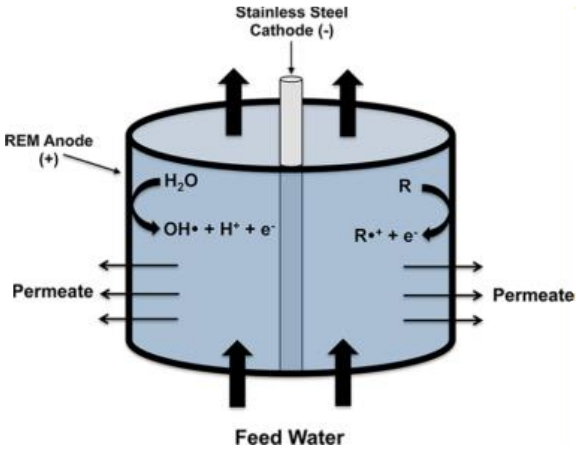

Figure 1.15 Schematic of Ti_4O_7 REM apparatus for water purification. Figure adapted from ref. [13].

1.4 Outline and Summary of Research

In this work, liquid water transport in polymer films and membranes was investigated and is classified into two categories: (1) understanding liquid water transport mechanisms on a molecular level, and (2) the development of membranes for water purification.

Accurately measuring and understanding transport mechanisms in polymer films and membranes is important for the development of polymeric materials used for these applications such as coatings, [1-2] packaging,[3-4] and desalination.[5-6] However, technical limitations of current methods to measure transport in polymers, and the nonequilibrium

nature of glassy polymers pose challenges for measuring water sorption in polymers. Chapter II addresses the need for a method to accurately measure liquid transport in free-standing polymer films without incurring significant error or solution-casting the film onto a substrate. Past studies on measuring liquid transport in free-standing polymer films have concentrated on glassy polymers. An apparatus (pressure-contact time-resolved FTIR-ATR spectroscopy) was developed to accurately measure liquid transport in free-standing films of a rubbery polymer, a glassy polymer, and a crosslinked polymer. Liquid diffusion in solution-cast and free-standing polymer films using FTIR-ATR spectroscopy was also compared. Although previous studies have explored FTIR-ATR spectroscopy to study liquid diffusion in free-standing films, to our knowledge, studies have not been conducted comparing liquid diffusion in solution-cast and free-standing polymer films. Additionally, a new transport model (diffusion-compression model) was developed to adequately describe the non-equilibrium water sorption kinetics observed using this apparatus for water in free-standing PMMA films.

Anomalous, or non-Fickian diffusion behavior is observed in glassy polymers due to their nonequilibrium state causing difficulties to arise when measuring liquid diffusion in glassy polymers, especially on a molecular level. Chapters III expands on the initial study of liquid water in glassy polymers conducted in Chapter II. Since the nonequilibrium nature of glassy polymers is due to the fact that their glass transition temperatures (T_gs) are much higher relative to the experimental temperature, in Chapter III, the addition of ionic liquid to glassy polymers was explored to examine the effect of T_g on liquid water diffusion behavior. The addition of ionic liquid to a glassy polymer

lowers the T_g of the polymer, allowing it to approach an equilibrium state. Liquid water transport in glassy polymer-ionic liquid mixtures was studied *via* FTIR-ATR spectroscopy to determine the effect of T_g on liquid water diffusion behavior.

Liquid transport in polymer membranes is also important for separations applications, such as water purification.[10] In addition to examining liquid transport at a molecular level, polymer membranes for water purification were designed and developed. Effective water treatment technologies need to treat a broad range of water contaminants, which typically is accomplished by using multiple technologies in a treatment train.[11] In order to reduce the cost and complexity of water treatment, research has focused on the development of novel technologies that can incorporate multiple treatment methods into a single technology.[11] Reactive electrochemical membranes (REMs) are a promising hybrid technology that act both as a membrane and a reactive electrochemical surface for the degradation of pollutants. Chapter IV describes the fabrication and performance of durable, conductive and flexible REMs for water purification and the degradation of phenolic pollutants. Simultaneous electrospinning/electrospraying was used for the fabrication of flexible, durable, and highly conductive reactive electrochemical membranes (REMs) for water purification. The electrochemical properties and water filtration performance of these E/E REMs were evaluated using electrical impedance spectroscopy (EIS), cyclic voltammetry (CV), and cross-flow filtration experiments. Chapter V concludes with a summary of the contributions of this research towards diffusion of small molecules in polymer films and membranes, as well as proposed future directions for the work proposed in this dissertation.

CHAPTER II

DIFFUSION OF LIQUID WATER IN FREE-STANDING POLYMER FILMS USING PRESSURE-CONTACT TIME-RESOLVED FOURIER TRANSFORM INFRARED ATTENUATED TOTAL REFLECTANCE SPECTROSCOPY

2.1 Introduction

The diffusion (*i.e.*, sorption kinetics) of water in polymers is of interest for a variety of applications.[1-9] However, there are limited studies that demonstrate accurate measurements for the diffusion of *liquid* water in polymers.[15-16, 35, 78-83] Unlike transport experiments for polymers that involve gasses or vapors as diffusants, conventional gravimetric techniques that measure the diffusion of liquids in solid-state polymers (*e.g.*, films) typically involves a tedious *ex situ* pat-and-weight technique that can possess low sensitivity and high experimental error.[17] Therefore, techniques that can accurately measure the diffusion of liquids in polymer films would be desirable for optimal design of products for various applications.

One technique that can accurately measure the diffusion of liquids in polymers is time-resolved Fourier transform infrared attenuated total reflection (FTIR-ATR) spectroscopy.[19] FTIR-ATR spectroscopy differentiates itself from other conventional techniques in that it provides molecular level contrast between diffusant(s) and polymer in real time.[17]

Traditionally, time-resolved FTIR-ATR spectroscopy experiments rely on polymers to be solution-cast onto the surface of the ATR element. The adhesion between the polymer film and the ATR element generated during the solution casting/annealing process creates intimate contact between the polymer and crystal for accurate collection of time-resolved infrared data. This technique is therefore traditionally limited to polymers that can be solution-cast onto the surface of the ATR element. Accurate measurements of liquid diffusion in free-standing commercially available or pre-fabricated polymer films that cannot be solution-cast onto an ATR element is of interest for a variety of industrial applications, and therefore, a technique that can accurately measure liquid diffusion in free-standing polymer films without directly solution casting the film onto the ATR element is highly desired.[24-25]

In this work, an apparatus (pressure-contact time-resolved FTIR-ATR spectroscopy) was developed to accurately measure liquid transport in free-standing films of a rubbery polymer (poly(isobutylene); PIB), a glassy polymer (poly(methylmethacrylate); PMMA), and a crosslinked polymer (epoxy/amine resin). Although several previous studies have explored FTIR-ATR spectroscopy to study liquid diffusion in free-standing films, to our knowledge, studies have not been conducted comparing liquid diffusion in solution-cast and free-standing polymer films using FTIR-ATR spectroscopy. In addition, a new transport model (diffusion-compression model) was developed to adequately describe the non-equilibrium water sorption kinetics for water in free-standing PMMA films.

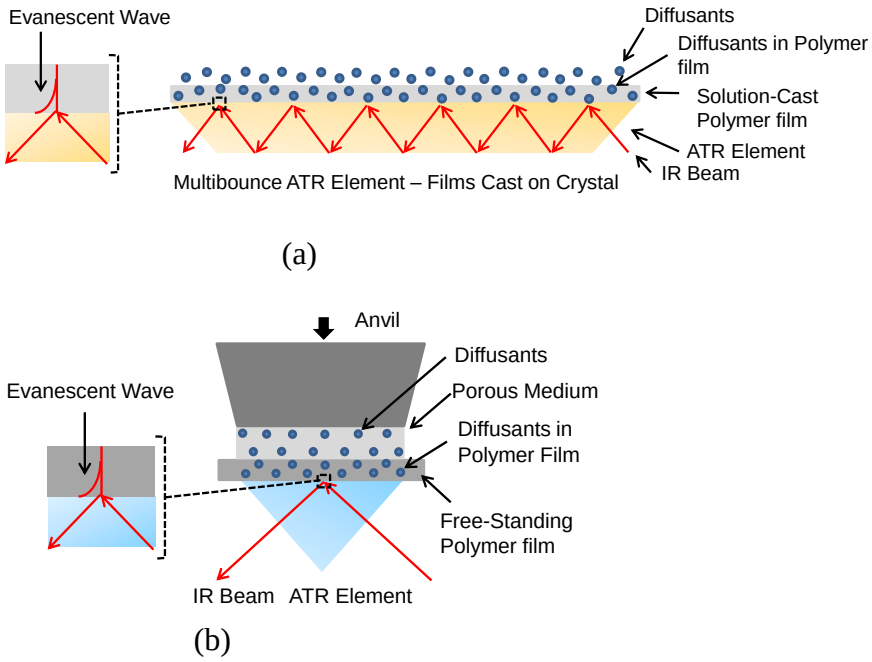

Figure 2.1 Schematic of (a) conventional multibounce FTIR-ATR apparatus with solution-cast film and (b) single-bounce pressure-contact FTIR-ATR apparatus with free-standing film. Evanescent wave highlighted in the magnified region.

2.2 Experimental

2.2.1 Materials

Poly(methyl methacrylate) (PMMA; M_w = 100,000 kg/mol, atactic beads) was purchased from Polysciences, Inc. and poly(isobutylene) (PIB; M_v = 4,700,000 g/mol, density = 0.92 g/cm^3, refractive index = 1.51) was purchased from Scientific Polymer Products. The epoxy/amine coating was supplied by PPG Industries. The solvent-based epoxy/amine formula consisted of epoxy resins, amine resins, clay, wollastonite, barium sulfate, talc, zinc pigments, titanium dioxide, and various solvents and additives, where the anti-corrosion pigments and additives (Part A) and the amines and solvents (Part B) were combined to create a free-standing epoxy/amine (1.13:1 ratio epoxy/amine)

coating.[84] Tetrahydrofuran (THF; anhydrous, ≥ 99.9% inhibitor-free), toluene (anhydrous, 99.8%), and acetone (ACS reagent, ≥ 99.5%) were purchased from Sigma Aldrich. Glass filter paper (G2, 0.66 mm thickness) was purchased from Fisher Scientific. Deionized water (resistivity *ca.* 16 MΩ cm) was used for all experiments.

2.2.2 Film Preparation

PMMA/THF and PIB/toluene solutions used for film fabrication were prepared by dissolving PMMA in THF at 5% w/w and PIB in toluene at 3% w/w and mixing for 24 h to ensure clear, homogenous solutions. Polymer films were then fabricated by drop casting each solution onto an ATR crystal surface for solution-cast time-resolved FTIR-ATR spectroscopy experiments or onto a Teflon petri dish (Applied Plastics Technology) for free-standing time-resolved FTIR-ATR spectroscopy experiments. The PMMA films were solution cast at room temperature for 24 h and then held under vacuum at room temperature for 24 h. The PMMA films were then annealed under vacuum at 70 °C for 3 h and then at 120 °C for an additional 3 h. PMMA films were physically removed from Teflon petri dishes to produce free-standing films for pressure-contact FTIR-ATR experiments. The PIB films were solution cast at room temperature for 48 h and then annealed under vacuum at 120 °C for 48 h. To produce free-standing PIB films for pressure-contact FTIR-ATR experiments, the PIB films were removed from the Teflon petri dishes using acetone and then annealed at 60 °C for an additional 1 h to remove any residual acetone. All polymers were annealed above their glass transition temperature (T_g = 119 and -65 °C for PMMA and PIB, respectively).

Complete solvent removal for both PMMA and PIB films were confirmed by FTIR analysis. Free-standing epoxy amine films were prepared by wrapping a 4" x 12" steel panel with DuPont™ Tedlar® polyvinyl fluoride film and securing on the back with masking tape. The panels were then baked at 166 °C for 15 min, and wiped with isopropyl alcohol. Part A and Part B were mixed, and after 1 hour, the coating was sprayed using a robotic spray system (Spraymation Compuspray with a Binks Model 95 spray gun). The panels were placed on racks for 30 minutes for solvent evaporation, and allowed to air dry at ambient conditions for 7 days. The free-standing epoxy amine films were removed from the Tedlar® film with the use of transparent tape and a razor blade. The thickness of each polymer film was measured before each experiment with a digital micrometer (Mituyo, 1 μm accuracy).

2.2.3 Time-Resolved FTIR-ATR Spectroscopy

Time-resolved infrared spectra were collected for all water diffusion experiments using an FTIR spectrometer (Nicolet 6700 Series; Thermo Electron). PMMA and PIB films were solution cast onto a multiple reflection, trapezoidal zinc selenide (ZnSe, refractive index = 2.4) ATR crystals (Specac, Inc.) with 45° beveled faces. A schematic of the conventional multibounce FTIR-ATR apparatus with solution-cast film is shown in Figure 2.1a. The polymer-coated ATR crystal was mounted and sealed in a horizontal, temperature-controlled ATR cell (Specac, Inc.) with a Kalrez gasket. Before each experiment, the space in the ATR cell above the polymer film (V = 550 μL) was filled with DI water *via* pipette and sealed to prevent evaporation. For pressure-contact time-resolved FTIR-ATR spectroscopy experiments, free-standing PMMA and PIB films

were placed onto a single-reflection diamond ATR crystal (surface area = 1.8 mm^2, refractive index = 2.4) within a Quest accessory (constant load capacity of anvil = 18 kg, Specac, Inc.). Two layers of glass filter paper (porous medium) were placed on top of the polymer film, and DI water was transferred onto the filter paper *via* pipette. Para film was used to cover and seal the entire apparatus to ensure that saturation was maintained, and the apparatus was held in place using the anvil from the Quest accessory to ensure pressure-contact between polymer film and ATR crystal. A similar apparatus was used for the epoxy/amine coatings, with an additional free-standing film of PMMA placed between the epoxy/amine coating and the filter paper. Due to the fragile nature of the epoxy/amine coating, the PMMA free-standing film was used to ensure the coating stayed intact for the duration of the experiment. At the center of the PMMA free-standing film, a hole smaller than the top surface area of the single-bounce ATR element was created in order to allow water to diffuse directly into the epoxy/amine coating. A schematic of the pressure-contact FTIR-ATR apparatus with free-standing film is shown in Figure 2.1b.

As water diffused from the water/polymer side to the polymer/crystal side, time-resolved spectra were collected in the region close to the polymer/crystal interface to quantify the diffusion of water through the polymer film. Spectra for all diffusion experiments were corrected by a background subtraction of the ATR crystal spectrum and were collected using a liquid nitrogen-cooled mercury-cadmium-telluride (MCT) detector with 32 scans per spectrum at a data spacing of 2 cm^{-1} resulting in spectrum collected every 19 seconds.

Time-resolved spectra were collected to determine the diffusion coefficient of water in the polymer film. The ATR experimental absorbance can be related to an analytical solution of a transient diffusion equation that adequately describes diffusion in a film with the appropriate set of initial and boundary conditions for this experiment. Unsteady-state diffusion of water in a film can be described by the following one-dimensional continuity equation (Fick's second law):

$$\frac{\partial C}{\partial t} = D_w \frac{\partial^{2C}}{\partial z^2} \tag{2.1}$$

where C is the concentration of the water, t is the time, z is the distance, and D_w is the effective concentration-averaged diffusion coefficient of water in the polymer. The initial and boundary conditions for the ATR experiment are:[19]

$$C = C_0 \text{ at } 0 < z < L \text{ and } t = 0 \tag{2.2}$$

$$\frac{dC}{dz} = 0 \text{ at } z = 0 \text{ and } t > 0 \tag{2.3}$$

$$C = C_{eq} \text{ at } z = L \text{ and } t > 0 \tag{2.4}$$

where L is the polymer film thickness, C_0 is the initial concentration of water (zero for all experiments), and C_{eq} is the final equilibrium concentration of water in the polymer. For the ATR system, z = 0 is the polymer-crystal interface and z = L is the water-polymer interface. The analytical solution to equation 1 with these initial and boundary conditions (eqs 2.2-2.4) is given:

$$\frac{C(t,z) - C_0}{C_{eq} - C_0} = 1 - \frac{4}{\pi} \sum_{n=0}^{\infty} \frac{(-1)}{2n+1} \exp\left[-D_w f^2 t\right] \cos\left[fz\right] \tag{2.5}$$

$$f = \frac{(2n+1)\pi}{2L} \tag{2.6}$$

Using a differential form of the Beer-Lambert law that incorporates the evanescent wave that propagates into the polymer from the ATR experiment, the concentration of water can be related to absorbance of water (collected from the ATR experiment):

$$A = \int_0^L \varepsilon^* C \exp\left(-2z/d_p\right) dz \tag{2.7}$$

where A is the ATR absorbance value, ε^* is the molar extinction coefficient (which is considered constant under the assumption of weak IR absorption for this study), and d_p is the depth of penetration for the IR radiation in the polymer (eq 2.8 below).

$$d_p = \frac{\lambda}{2\pi n_1 \sqrt{\sin^2\theta - \left(n_2/n_1\right)^2}} \tag{2.8}$$

In eq 2.8, n_1 is the refractive index of the polymer, n_2 is the refractive index of the ATR crystal, θ is the angle of incidence, and λ is the wavelength of absorbed light. For these experiments, the depth of penetration is *ca.* 1 μm, which is the sampling distance into the polymer from the polymer-crystal interface. Substituting eq 2.5 into eq 2.7 and integrating yields the following expression:[15, 23]

$$\frac{A(t)-A_0}{A_{eq}-A_0} = 1 - \frac{\left(8/d_p\right)}{\pi\left[1-\exp\left(-2L/d_p\right)\right]} \sum_{n=0}^{\infty} \frac{1}{2n+1} \times \left(\frac{\exp\left(-D_w f^2 t\right)\left[f \exp\left(-2L/d_p\right) + (-1)^n \left(2/d_p\right)\right]}{\left(\left(2/d_p\right)^2 + f^2\right)} \right) \tag{2.9}$$

where A(t), is the ATR absorbance at time t, A_0 is the initial ATR absorbance, and A_{eq} is the ATR absorbance at equilibrium. Eq 2.9 can be regressed to the experimental ATR absorbance data obtained (A(t)) to determine the diffusion coefficient of water (D_w; the only adjustable parameter) for the case when Fickian diffusion is observed.

2.3 Results and Discussion

2.3.1 Water Diffusion in Poly(isobutylene) (PIB)

Figure 2.2 shows the infrared spectra of solution-cast and free-standing PIB films before exposure to water, *i.e.*, fingerprint region of the polymer. The key infrared bands that appear in Figure 2.2 are listed in Table 2.1.[85-87] The intensity of the infrared spectra for the solution-cast PIB film is higher than the intensity of the infrared spectra for the free-standing PIB film. The multiple bounces (six) for ZnSe ATR crystal produces a higher overall signal intensity for the solution-cast film compared to the single-bounce diamond ATR crystal for the free-standing film. Also, notice that diamond does not absorb IR light in the range from approximately 2000-2500 cm^{-1} and therefore the features in this part of the spectra should be neglected.

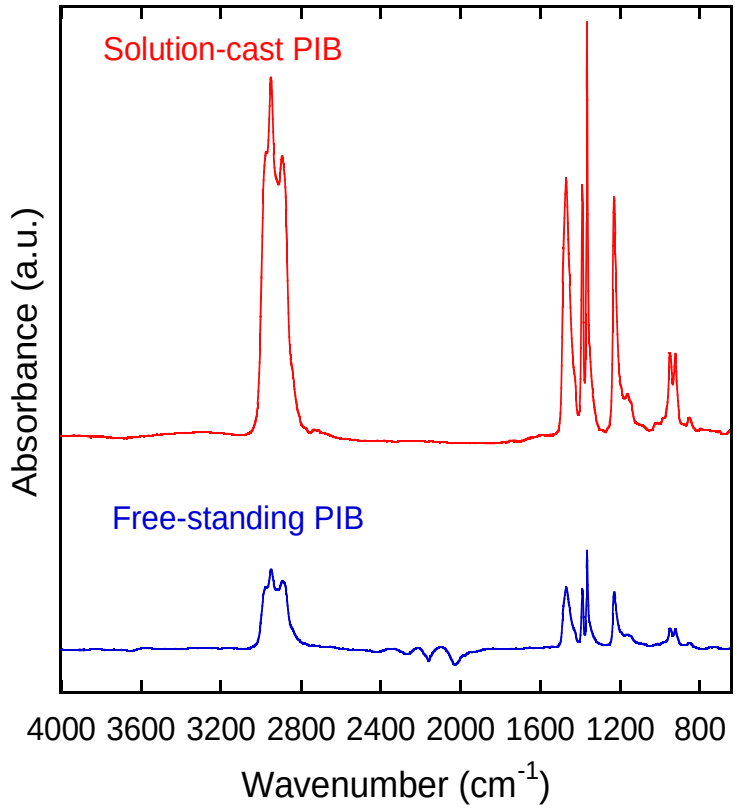

Figure 2.2 Infrared spectra of solution-cast and free-standing films of PIB measured with multi-bounce ZnSe ATR crystal and single-bounce diamond ATR crystal, respectively. Spectra are offset for clarity.

Table 2.1 Infrared Band Locations of PIB.

Bond Vibration	Band Location (cm^{-1})	References
CH stretching	2980, 2950, 2890, 2720	85
CH bending	1465	85
CH_3 swinging	1385	85-87
CH_3 swinging	1360	85-86
CH bending	1225, 1160, 950	85
C-C stretching	920	85

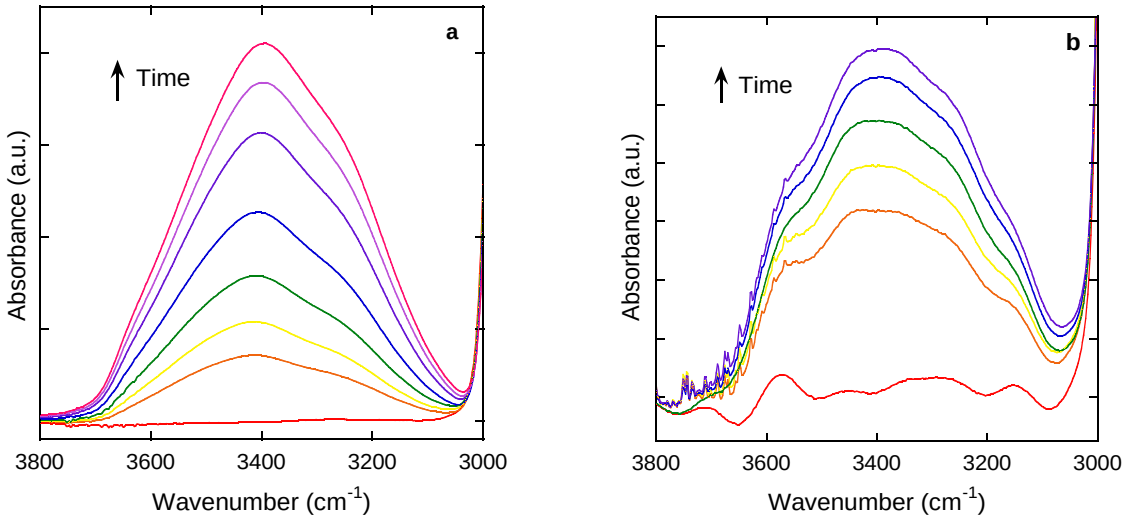

Figure 2.3 Infrared spectra of the water O-H stretching region at selected times showing water diffusion in PIB for (a) solution-cast film and (b) free-standing film.

The time-resolved infrared spectra of liquid water diffusing in solution-cast and free-standing PIB films is shown in Figures 2.3a and b, respectively. Figures 2.3 shows the intensity of the infrared spectra of the water O-H stretching region increasing with time, indicating the diffusion of water into PIB. The integration of the data (O-H stretching region) in Figure 2.3 is plotted in Figure 2.4a to show the sorption kinetics of water in the polymer films. Note that the rate of water sorption is similar for the solution-cast and free-standing PIB films using the two different techniques. Figure 2.4b shows the data in Figure 2.4a versus normalized time (film thickness independent). Similar to Figure 2.4a, the rate of water sorption is similar between the two techniques, which was expected since both solution-cast and free-standing films are of similar thicknesses (the reason why rates are similar in Figure 2.4a, which is dependent on film thickness). Overall, the results from Figure 2.4 demonstrate that the pressure-contact ATR technique produces

similar results to the solution-cast ATR technique and therefore the pressure-contact technique may be suitable to measure accurate diffusion of liquids in free-standing rubbery polymer films.

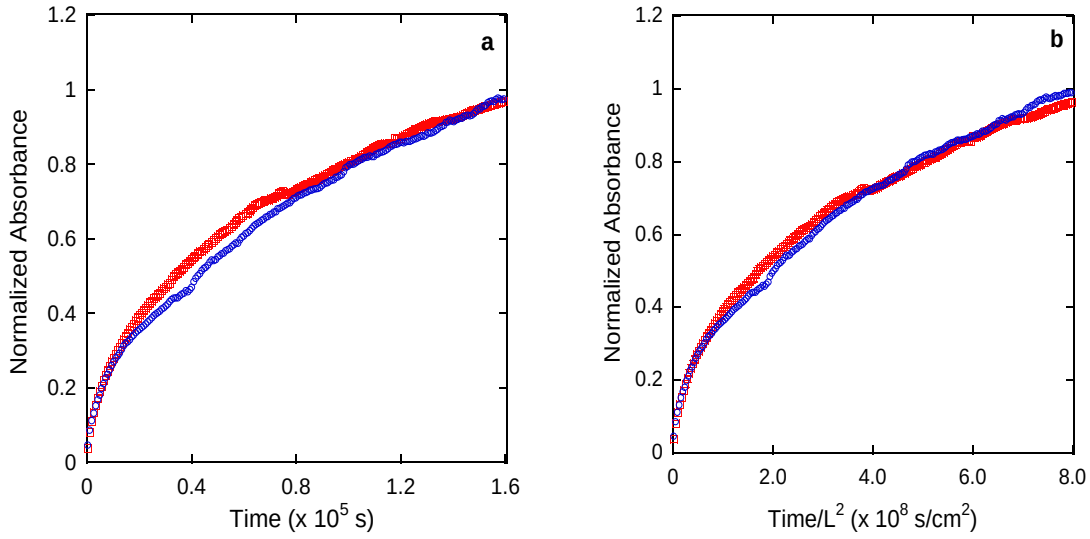

Figure 2.4 Time-resolved infrared spectroscopy data: normalized integrated absorbance of the water O-H stretching region in solution-cast PIB film (red squares) and free-standing PIB film (blue circles) at room temperature versus (a) time and (b) normalized time (*i.e.*, normalized by film thickness squared). The thicknesses of the solution-cast and free-standing PIB films were 140 and 145 μm, respectively. Absorbance was normalized by the absorbance at late time.

Figure 2.5 shows a regression of the data in Figure 2.4a to the ATR solution of the Fickian diffusion model (eq 2.9; represented by the solid line), where the diffusion coefficient was the only adjustable parameter. The poor regression shown in Figure 2.5 clearly indicates that the diffusion of liquid water in PIB is non-Fickian. This was initially unexpected since the glass transition temperature of PIB is well below the experimental temperature (room/ambient temperature) and Fickian behavior is typically

observed for the diffusion of small molecules in rubbery polymers. However, several past studies have also shown non-Fickian behavior specifically for the diffusion of liquid water in rubbery polymers.[50, 88-89] Gao *et al.*[88-89] observed non-Fickian behavior for the diffusion of liquid water in silicone rubber films. They attributed the non-Fickian behavior to the presence of two states of water, 'free' and 'bound' water, and their interactions with silicone rubber.[88-89] Sundfors *et al.*[50] used conventional FTIR-ATR spectroscopy to study liquid water diffusion in silicone rubber mixtures. Similar to results by Gao *et al.*, Sundfors *et al.* also observed non-Fickian behavior for liquid water diffusion in silicone rubber.[50, 88-89] Their results showed that liquid water diffusion in silicone rubber was slow and they attributed this to the clustering behavior in water due to self-associating hydrogen bonding.[50] Therefore, it appears that there is something unique about water as a diffusant in rubbery polymers compared to other small molecule diffusants. Regardless of the non-Fickian behavior observed in this work and by others, the key result shown in Figure 2.4 still demonstrates that both techniques yield similar results and therefore the pressure-contact method may be suitable to accurately measure sorption kinetics of liquids in rubbery polymers for free-standing films. The measurement of diffusion in free-standing polymer films cannot be accomplished with the conventional time-resolved FTIR-ATR spectroscopy technique, which requires solution casting the polymer film onto the ATR crystal.

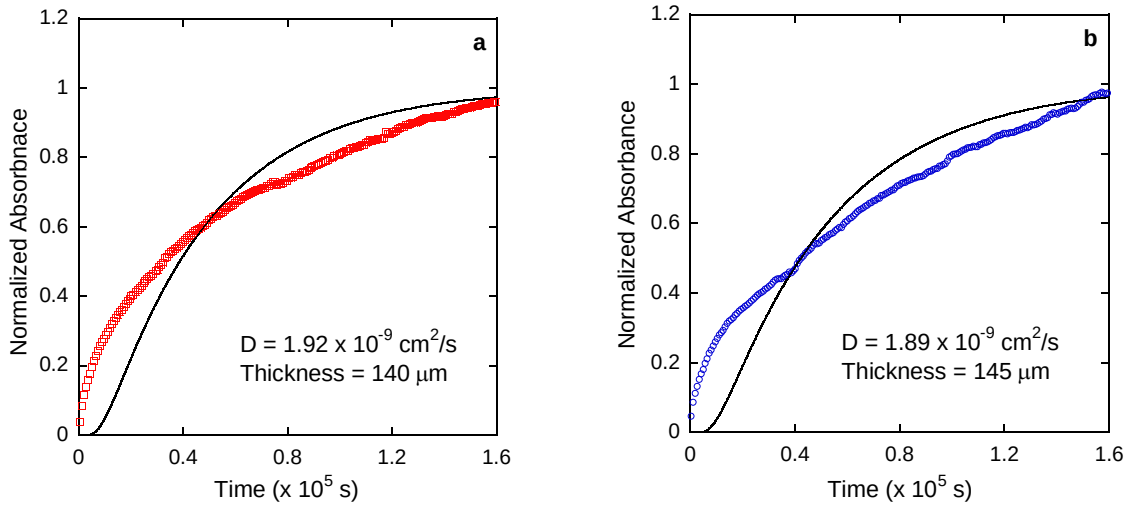

Figure 2.5 Time-resolved infrared spectroscopy data: normalized integrated absorbance of the water O-H stretching region in PIB at room temperature for the (a) solution-cast film and (b) free-standing film. The solid line represents a regression to the ATR solution of the Fickian model (eq 2.9).

In order to obtain a slightly more accurate diffusion coefficient for water in PIB, the data was regressed to late-time approximation of eq 2.9 developed by Fieldson and Barbari:[90]

$$\ln\left(1-\frac{A_t}{A_{eq}}\right)=\ln\left(\frac{4}{\pi}\right)-\frac{D\pi^2}{4L^2}t \qquad (2.10)$$

Figure 2.6 shows a regression of the ATR data in Figure 2.4 to eq 2.10, where the diffusion coefficient was the only adjustable parameter. Figure 2.6 shows that the diffusion coefficient for water in both the solution-cast and free-standing PIB films obtained from the late-time approximation method are similar. Since the pressure-contact ATR technique produces similar diffusion coefficients to those obtained using the solution-cast ATR technique, this is another confirmation that the pressure-contact

technique maybe be a suitable method for measuring diffusion of liquids in free-standing rubbery polymer films.

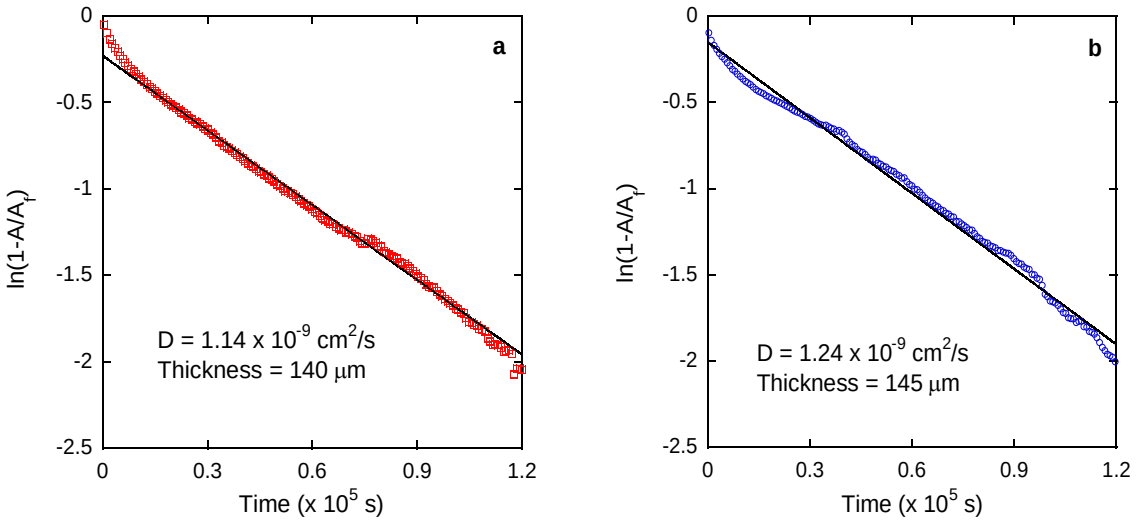

Figure 2.6 Time-resolved infrared spectroscopy data: normalized integrated absorbance of water O-H stretching region in PIB at room temperature for the (a) solution-cast film and (b) free-standing film. The solid line represents a regression to the late-time approximation of the ATR solution of the Fickian model (eq 2.10).

2.3.2 Water Diffusion in Poly(methylmethacrylate) (PMMA)

Figure 2.7 shows the infrared spectra of solution-cast and free-standing PMMA films before exposure to water. The infrared spectra shows all the key infrared bands associated with PMMA, which are also listed in Table 2.2.[91-99] Similarly to Figure 2.2, the intensity of the infrared spectra for the solution-cast PMMA film is higher than the intensity of the infrared spectra for the free-standing PMMA film.

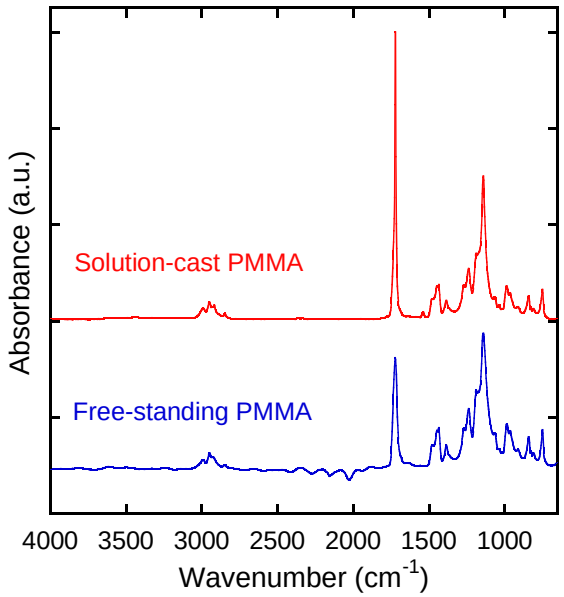

Figure 2.7 Infrared spectra of a solution-cast and a free-standing film of PMMA. Spectra are offset for clarity.

Table 2.2 Infrared Band Locations for PMMA.

Bond Vibrations	Band Location (cm^{-1})	References
CH stretching, CH_3 asymmetric stretching	2900, 2927, 2951, 2960	91-92, 94, 96-99
C=O stretching	1723	91, 93-99
OH bending/deformation	1650	91
CH_3 asymmetric stretching	1483	92, 97
CH_3, CH_2 stretching	1446	94-97
O-CH_3 deformation, CH_3 stretching	1434	92, 97-98
O-CH_3, CH_3 stretching	1386	92, 94, 97, 99
- C-O stretching, C-CH_3 stretching, and COC vibration	1062, 1143, 1195, 1238, 1272	92-99
CH_3, CH_2 stretching	841	94, 96-97, 99
C-C backbone skeletal vibration	750	96-97, 99

The time resolved infrared spectra of liquid water diffusing in solution-cast and free-standing PMMA films are shown in Figures 2.8a and b, respectively. Figures 2.8a and b show the intensity of the infrared spectra of the water O-H stretching region increasing with time, indicating the diffusion of water into PMMA.

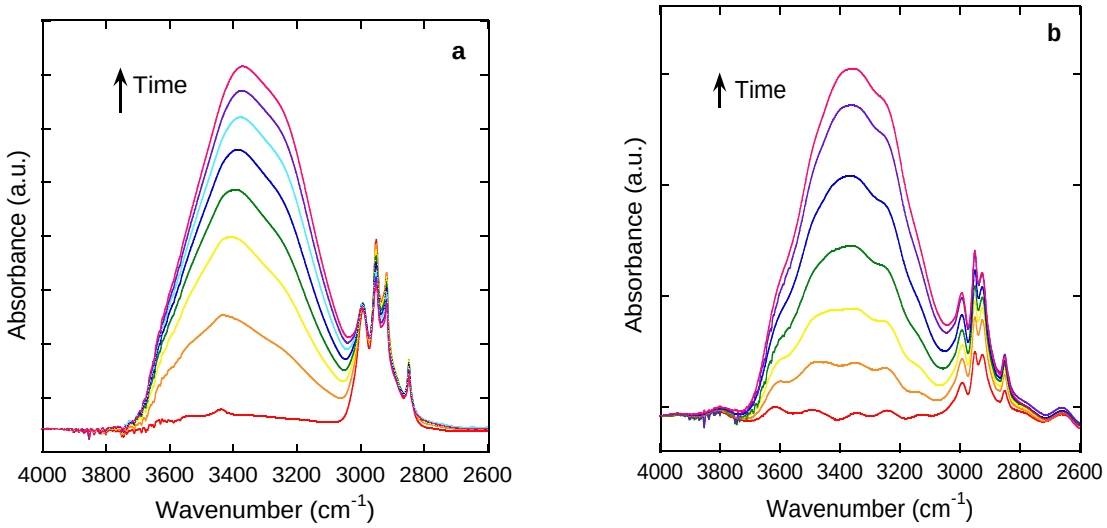

Figure 2.8 Infrared spectra of the water O-H stretching region at selected times showing water diffusion in PMMA for (a) solution-cast film and (b) free-standing film.

The integration of the data in Figure 2.8 is plotted in Figure 2.9 to show the sorption kinetics of water in the polymer films. However, unlike Figure 2.4a, the rate of water sorption is not similar when comparing the solution-cast film to the free-standing film using the two different techniques. Figure 2.9b shows the data in Figure 2.9a versus normalized time (film thickness independent). Similar to Figure 2.9a, the rate of water sorption is not similar between the two techniques, despite the fact that the solution-cast and free-standing films are of similar thicknesses.

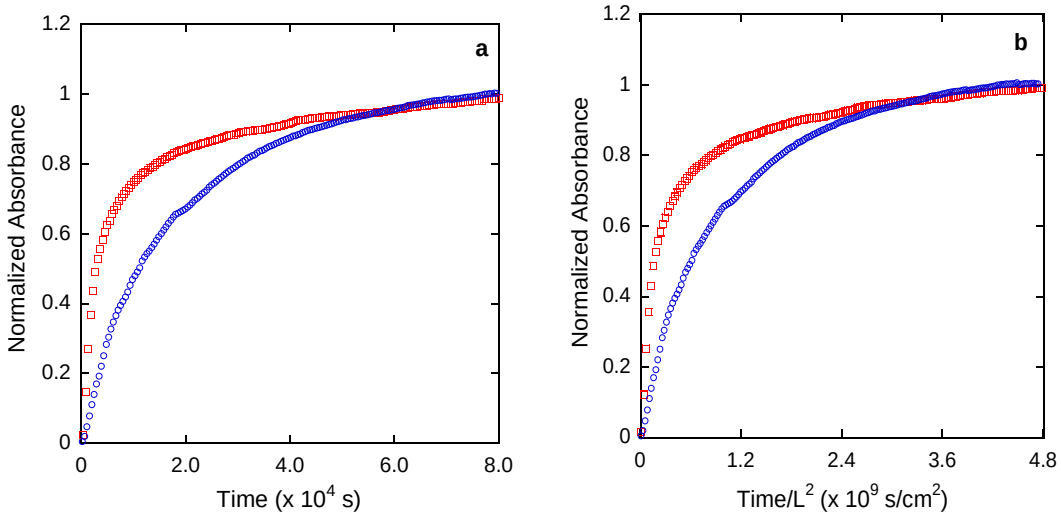

Figure 2.9 Time-resolved infrared spectroscopy data: normalized integrated absorbance of water O-H stretching region in solution-cast PMMA film (red squares) and free-standing PMMA film (blue circles) at room temperature versus (a) time and (b) normalized time (*i.e.*, normalized by film thickness squared). The thicknesses of the solution-cast and free-standing PMMA films were 40 and 43 μm, respectively. Absorbance was normalized by the absorbance at late time.

Figure 2.10 shows a regression of the data in Figure 2.9a to the ATR solution of the Fickian diffusion model (eq 2.9; represented by the solid line). The regression shown in Figure 2.10 clearly indicates that liquid water diffusion in PMMA is not adequately described by the Fickian model for either measurement technique. Although, diffusion in the free-standing film appears more Fickian than the solution-cast film. This non-Fickian result was expected as many studies have shown non-Fickian sorption profiles for the diffusion of small molecules in glassy polymers.[42] Prior work on the diffusion of water in PMMA using the solution-cast FTIR-ATR method have attributed this non-Fickian behavior to diffusion and polymer relaxation occurring on similar time scales in a

nonequilibrium system (*i.e.*, the glass transition temperature of the polymer is much higher than the experimental temperature), where diffusion is driven by the concentration gradient of the diffusant and polymer relaxation is a response to the stress imposed by the diffusant.[30, 42] This previous work explains the non-Fickian behavior observed, however the differences in sorption kinetics between the conventional solution-cast and free-standing pressure-contact FTIR-ATR methods are not readily apparent (noticeable by both the rates not matching in Figure 2.9 and the differences in diffusion coefficients in Figure 2.10). This difference may be attributed to the differences in the configuration of the apparatuses and their impact on polymer relaxation during water sorption.

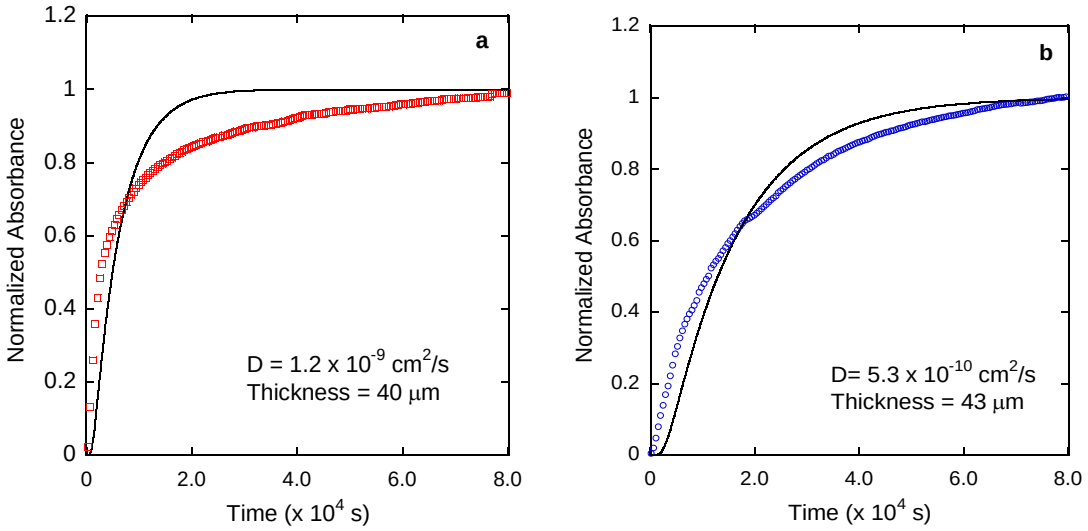

Figure 2.10 Time-resolved infrared spectroscopy data: normalized integrated absorbance of water O-H stretching region in PMMA at room temperature for (a) solution-cast film and (b) free-standing film. The solid line represents a regression to the ATR solution of the Fickian model (eq 2.9).

Figure 2.11 shows a schematic of the difference between the conventional solution-cast and pressure-contact FTIR-ATR apparatus. The conventional solution-cast FTIR-ATR apparatus (Figure 2.11a) shows that the polymer is solution-cast directly onto the ATR element, providing intimate polymer-crystal contact for accurate collection of time-resolved infrared data. The diffusant (water) is introduced over the polymer film, and the polymer film undergoes water-induced polymer relaxation upwards in the thickness direction because there is no constraint at the water/polymer interface. The free-standing polymer film in the pressure-contact FTIR-ATR apparatus (Figure 2.11b) is placed between the ATR element and a porous medium (filter paper). The diffusant is introduced to the porous medium and the apparatus was held in place with an anvil, which exerts pressure on the polymer film. The pressure exerted by the anvil provides the intimate polymer/crystal contact for accurate collection of time-resolved infrared data. As water diffuses through the polymer, the pressure exerted by the porous medium and the anvil keep the polymer film from relaxing similarly to the solution-cast FTIR-ATR technique, where there is a constraint at the water/polymer interface and therefore the polymer may undergo compression in the downward direction instead of relaxation in the upward direction.

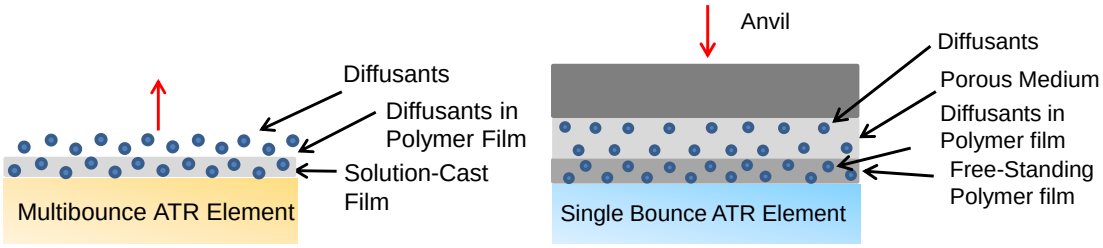

(a) (b)

Figure 2.11 Schematic of a) conventional solution-cast and b) free-standing pressure-contact apparatus illustrating relaxation in the upward direction and compression, respectively, in response to the stress imposed by the diffusant.

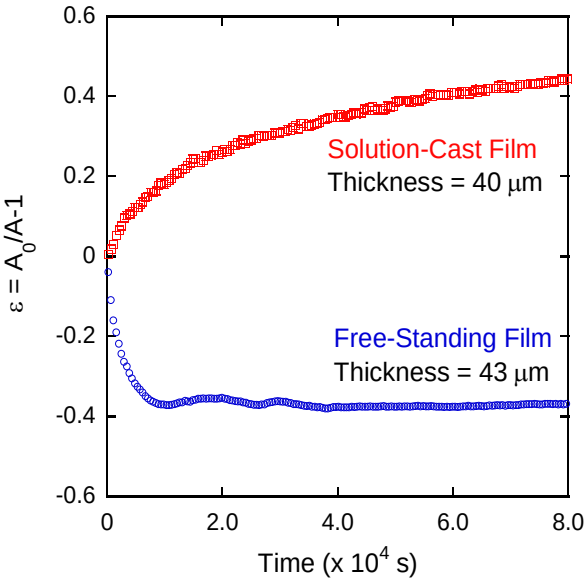

Figure 2.12 Time-resolved infrared spectroscopy data: normalized integrated absorbance of the CH_3 stretching region in PMMA for solution-cast film (red squares) and free-standing film (blue squares) versus time. The thickness of the solution-cast and free-standing PMMA films were 40 and 43 μm, respectively.

The impact of the apparatus configuration differences (Figure 2.11) is revealed in Figure 2.12. Figure 2.12 shows the absorbance of the CH_3 stretching region of PMMA

polymer backbone during water sorption for both the solution-cast and free-standing films. Absorbance is scaled to relate directly to volumetric polymer strain (eq 2.19). The strain for the solution-cast film increases with time, indicating water induced time-dependent relaxation of PMMA. However, the strain for the free-standing film shows a decrease in absorbance followed by a steady value, suggesting time-dependent compression of the PMMA film. Therefore, the differences in water diffusion behavior between solution-cast and free-standing PMMA (Figure 2.9) may be due to the differences in the glassy polymer response in the non-equilibrium state as shown in Figure 2.12. The data in Figure 2.12 was regressed to models that incorporate relaxation and compression, respectively, as described below, to more accurately describe water sorption kinetics for both solution-cast and free-standing PMMA films.

The non-Fickian behavior observed in Figure 2.10a has been previously observed and associated with diffusion and polymer relaxation occurring at similar time scales. The concentration gradient of the liquid water, the diffusant, is the driving force for diffusion, while polymer relaxation is the response to the stress imposed by the diffusant. For a rubbery polymer, the time scale for relaxation (rapid viscoelastic response with short-time equilibration) is much shorter than diffusion and therefore is not observed on the same time scale for diffusion (the experimental time scale) and therefore Fickian behavior results under this equilibrium framework. However, for a glassy polymer the time scale for relaxation (viscoelastic response with long-time viscous loss) can be on a similar time scale for diffusion and therefore both can be observed at the time scale of the experiment and non-Fickian behavior results under the nonequilibrium framework.

Based on the ability to observe diffusion and relaxation simultaneously in the same experiment, a mathematical model was developed that incorporates both phenomena using a minimal number of fitting parameters by Hallinan *et al.*[23] for their observation of diffusion-relaxation for water vapor diffusion in Nafion. Using the diffusion-relaxation model developed by Hallinan *et al.*,[23] the polymer relaxation data (absorbance of the CH_3 stretching region) for solution-cast PMMA can be regressed using a relaxation portion of the model to determine a relaxation time constant. Then, using the relaxation time constant from the relaxation portion of the model, the water diffusion data can be regressed to the diffusion-relaxation model to determine a diffusion coefficient, D. The relaxation portion of the model is based on a three-element viscoelastic model, which consists of a dashpot in series with a dashpot and spring in parallel. The dashpot is represented by Newton's law of viscosity, which expresses unrecoverable viscous loss:

$$\sigma = \eta \frac{\partial \varepsilon}{\partial t} \tag{2.11}$$

where σ is the stress, η is the dynamic viscosity, and ε is the stress. The spring can be described using Hooke's law and it expresses the elastic recoverable portion:

$$\sigma = E\varepsilon \tag{2.12}$$

where E is Young's modulus. The viscoelastic response is expressed using the spring and dashpot in parallel, and this two element model is referred to as the Kelvin (or Voigt) model. Based on mechanical creep deformation, constant stress, σ, is assumed and applied, and the strain is measured as a function of time:

$$\varepsilon = \frac{\sigma}{E}\left(1 - \exp\left(-\beta t\right)\right) \tag{2.13}$$

where β is the relaxation time constant. Additionally, based on mechanical creep deformation, the strain for a dashpot can be described as follows:

$$\varepsilon = \frac{\sigma t}{\eta} \tag{2.14}$$

Combining eqs 2.13 and 2.14 results in the three-element viscoelastic model:

$$\varepsilon = \frac{\sigma t}{\eta} + \frac{\sigma}{E}\left(1 - \exp\left(-\beta t\right)\right) \tag{2.15}$$

This model assumes that stress, σ, viscosity, η, and Young's modulus, E, are all constant. Additionally, polymer relaxation can be described by relating strain to infrared absorbance of the polymer using the Beer-Lambert law.

$$\varepsilon = \frac{\Delta V}{V} \approx \frac{1/C - 1/C_0}{1/C_0} \approx \frac{1/A - 1/A_0}{1/A_0} = \frac{A_0}{A} - 1 \tag{2.16}$$

Eq 2.16 proposes that the infrared absorbance of the polymer is inversely proportional to the strain imposed by liquid water diffusing into the polymer. Liquid water diffusing into the polymer results in an increase in volume in the sampling depth region. Since absorbance is proportional to concentration (based on the Beer-Lambert law), the increase in polymer volume leads to a decrease in the absorbance of the polymer. Eq 2.15 can be rewritten in terms of the infrared absorbance of the CH_3 stretching region using eq 2.16.

$$\frac{A_0}{A} - 1 = \frac{\sigma t}{\eta} + \frac{\sigma}{E}\left(1 - \exp\left(-\beta t\right)\right) \tag{2.17}$$

A late-time solution to eq 2.17 describes only the viscous loss portion of the relaxation model due to nonequilibrium, resulting in a linear expression, with a slope (σ/η) and an

intercept (σ/E), which are the mechanical constants of the relaxation model. Figure 2.13a shows the regression of the late-time CH_3 stretching absorbance of the polymer, where σ/η = 2.11 x 10^{-6} Pa/(Pa·s) and σ/E = 0.27 Pa/Pa. Using these values, the polymer relaxation data was regressed to the full relaxation model, eq 2.17. Figure 2.13a also shows this regression, where the relaxation time constant, β, is 8.85 x 10^{-5} s^{-1}. Based on Figure 2.13a, it appears that the viscoelastic model in eq 2.17 agrees with the data. The relaxation time constant, β, found using the regression shown in Figure 2.13a can now be used to regress the water diffusion data to the diffusion-relaxation model.

$$\frac{A(t)-A_0}{A_{eq}-A_0} = F_A\left[1-\frac{(8/d_p)}{\pi\left[1-\exp(-2L/d_p)\right]}\sum_{n=0}^{\infty}\frac{1}{2n+1}\times\left(\frac{\exp(-Df^2t)\left[f\exp(-2L/d_p)+(-1)^n(2/d_p)\right]}{\left((2/d_p)^2+f^2\right)}\right)\right] + F_B\left[w_2t+w_1(1-\exp(-\beta t))\right] \quad (2.18)$$

$$w_1 = \frac{\frac{\eta}{E}}{t_f+\frac{\eta}{E}} \quad (2.19)$$

$$w_2 = \frac{1}{t_f+\frac{\eta}{E}} \quad (2.20)$$

The diffusion-relaxation model shown in eq 2.18 is the weighted sum of the Fickian diffusion (eq 2.9) and the three-element relaxation model (eq 2.17). F_A is the weighting fraction for the diffusion portion and F_B is the weighting fraction for the relaxation portion. Eq 2.17 was normalized with respect to strain at long times, t_f, yielding dimensionless constants, w_1 and w_2, which can now be used in the normalized diffusion-relaxation model (eq 2.18). Eq 2.18 is now expressed as $(A(t)-A_0)/(A_{eq}-A_0)$ instead of $(A_0/A(t)-1)$. The use of equation 2.20 was further validated in work by Davis *et al.*[15] by

expressing the polymer relaxation data as both $(A(t)-A_0)/(A_{eq}-A_0)$ and $(A_0/A(t)-1)$. The average percent difference between both sets of data was less than 4% for each experiment they conducted.[15] Additionally there was a negligible difference in regressed constants from the late-time and full regressions of the polymer relaxation data using $(A(t)-A_0)/(A_{eq}-A_0)$ or $(A_0/A(t)-1)$.

Eq 2.18 was used to regress the water diffusion data for solution-cast PMMA, and similar to the polymer relaxation regression, there is a late-time solution to eq 2.18 that allows the weighing fractions, F_A and F_B, to be calculated. The late-time solution to eq 2.18 arises when the exponential terms approach zero at late times, producing a linear expression with a slope of $F_B w_2$ and intercept of $F_A + F_B w_1$. It represents the water that diffuses into the polymer due to the viscous loss due to polymer relaxation. The late-time regression of the water diffusion data (OH stretch) is shown in Figure 2.13b (dashed line). The late time slope ($F_B w_2$) was 2.82×10^{-6} s^{-1} and intercept ($F_A + F_B w_1$) was 0.79. Using regressed constants from the late-time regression of the polymer relaxation data for solution-cast PMMA (using eq 2.17), where $\sigma/\eta = 2.11 \times 10^{-6}$ Pa/(Pa·s) and σ/E = 0.27 Pa/Pa, F_A and F_B were calculated to be 0.65 and 0.35, respectively. The water diffusion data set can now be regressed to eq 2.18 (diffusion-relaxation model) using σ/η, σ/E, β, F_A and F_B, where the diffusion coefficient, D, is the only fitting parameter. The full regression of the water diffusion data to the diffusion-relaxation model (solid line) is shown in Figure 2.13b, where the diffusion coefficient, D, is 3.2×10^{-9} cm^2/s.

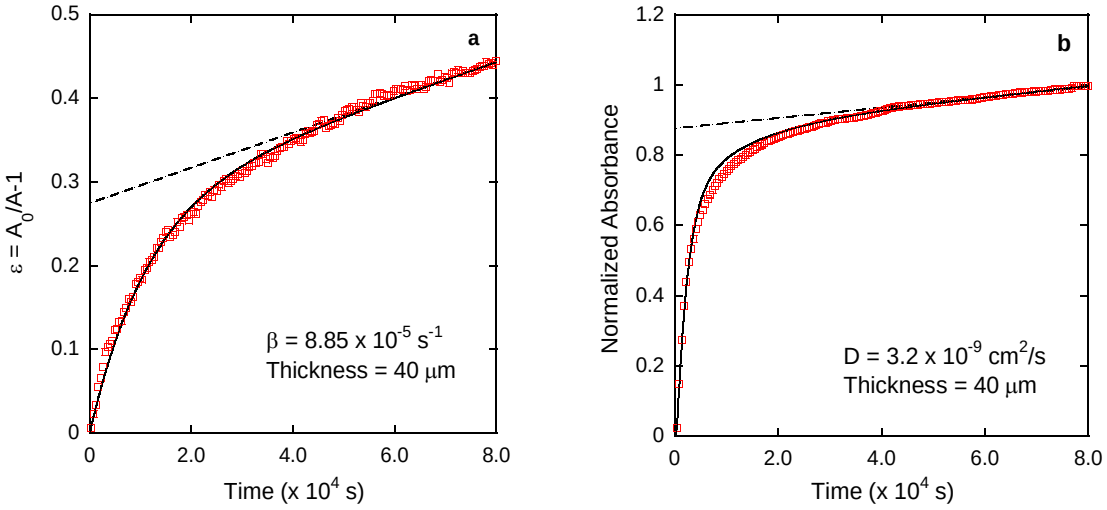

Figure 2.13 Time-resolved infrared spectroscopy data for solution-cast PMMA film at room temperature: (a) normalized integrated absorbance of CH_3 stretching region in PMMA regressed to a polymer relaxation model; the dashed and solid lines represent the late-time linear solution and full solution of eq 2.17, respectively, and (b) normalized integrated absorbance of the water O-H stretching region in PMMA regressed to the diffusion-relaxation model; the dashed and solid lines represent the late-time linear solution and full solution of eq 2.18, respectively.

The diffusion-compression behavior (shown in Figure 2.10b and Figure 2.12) has not been observed previously with ATR and therefore a new model that incorporates both phenomena for ATR was developed in this work. Several viscoelastic models were investigated to accurately describe the polymer compression data shown in Figure 2.12. A two-element viscoelastic model most accurately captured the polymer physics in this work (Figure 2.12). Therefore, the polymer compression data for the free-standing PMMA was regressed to a two-element compression model to determine a compression time constant. Using the compression time constant and a new diffusion-compression model, the water diffusion data was regressed to determine a diffusion coefficient, D.

The compression model is based on a two-element model, which consists of a dashpot and spring in parallel. The polymer compression model is shown in eq 2.21:

$$\frac{A_0}{A} - 1 = -\frac{\sigma}{E}\left(1 - \exp\left(-\beta t\right)\right) \tag{2.21}$$

A late-time solution to eq 2.21 results in -σ/E, which is a mechanical constant of the compression model. Figure 2.14a shows the regression of the late-time CH_3 stretching absorbance of the polymer, where σ/E = 0.37 Pa/Pa. Using these values, the polymer compression data was regressed to the full compression model, eq 2.21. Figure 2.14a also shows this regression, where the compression time coefficient, β, is 4.44 x 10^{-5} s^{-1}. Based on Figure 2.14a, it appears that the two-element model in eq 2.21 agrees with the data. The compression time constant, β, found using the regression shown in Figure 2.14a, can now be used to regress the water diffusion data to a new diffusion-compression model.

$$\frac{A(t) - A_0}{A_{eq} - A_0} = F_A\left[1 - \frac{\left(8/d_p\right)}{\pi\left[1 - \exp\left(-2L/d_p\right)\right]}\sum_{n=0}^{\infty}\frac{1}{2n+1}\times\left(\frac{\exp\left(-D_w f^2 t\right)\left[f\exp\left(-2L/d_p\right) + (-1)^n\left(2/d_p\right)\right]}{\left(\left(2/d_p\right)^2 + f^2\right)}\right)\right] + \left(1 - F_A\right)\left[-\frac{\sigma}{E}\left(1 - \exp\left(-\beta t\right)\right)\right] \tag{2.22}$$

Eq 2.22 was used to regress the water diffusion data for free-standing PMMA to accurately capture diffusion-compression. Using the regressed constant from the late-time regression of the polymer compression data for free-standing PMMA (using eq 2.21), σ/E = 0.37 Pa/Pa, F_A was calculated to be 0.99. This value for F_A suggests that the water diffusion data is in fact almost completely Fickian, *i.e.*, as F_A approaches 1, the diffusion-compression model approaches Fickian behavior. Once all of these constants (σ/E, β, and F_A) are obtained, the water diffusion data set can now be regressed to eq

2.22 to determine the diffusion coefficient, D. The full regression of the water diffusion data to the new diffusion-compression model is shown in Figure 2.14b, where the diffusion coefficient, D, is 5.6 x 10^{-10} cm^2/s. The diffusion coefficient obtained using the diffusion-compression model (eq 2.22) is similar to the diffusion coefficient obtained using the Fickian model (eq 2.9), which confirms the value of F_A = 0.99 from the diffusion-compression model. Several other factors also confirm this nearly Fickian behavior. The polymer compression data (Figure 2.12) mirrors the inverse of the type of polymer relaxation behavior one would observe for Fickian diffusion of a rubbery polymer, *i.e.*, rapid viscoeleastic response with short-time equilibration. Also, the Fickian regression for the diffusion data for the solution-cast PMMA from Figure 2.10a are not comparable, which differs from the Fickian regression for the diffusion data for the free-standing PMAA in Figure 2.10b. The combination of Figure 2.10b and Figure 2.14b and the subsequent parameter values from the diffusion-compression model and the compression data (Figure 2.12 and Figure 2.14a) all imply that the pressure exerted on the polymer by the anvil suppresses the polymer relaxation behavior that results in non-Fickian behavior and rather mimics a pseudo-Fickian response. This compression phenomena result in different sorption kinetics for glassy polymers that are in the nonequilibrium state, but appears to not affect rubbery polymers that are in an equilibrium state.

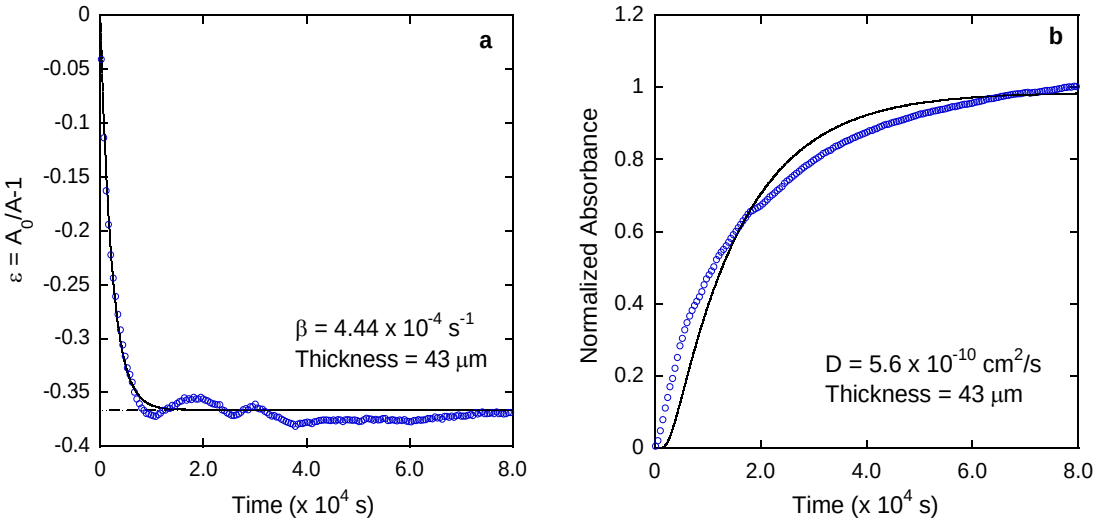

Figure 2.14 Time-resolved infrared spectroscopy data for free-standing PMMA film at room temperature: (a) normalized integrated absorbance of CH_3 stretching region in PMMA regressed to a compression model; the dashed and solid lines represent the late-time linear solution and full solution of eq 2.21, respectively, and (b) normalized integrated absorbance of the water O-H stretching region in PMMA regressed to a modified diffusion model; the solid line represents the full solution of eq 2.22, respectively.

In addition to measuring liquid diffusion in rubbery and glassy polymers, liquid sorption in a free-standing crosslinked polymer was measured using the pressure-contact FTIR-ATR apparatus. The time-resolved infrared spectra of liquid water diffusing in a crossliniked epoxy/amine free-standing film is shown in Figure 2.15a. Figure 2.15a shows the intensity of the infrared spectra of the water O-H stretching region increasing with time, indicating the diffusion of water into the crosslinked free-standing film. The integration of the data (water O-H stretching region) in Figure 2.15a is plotted in Figure 2.15b to show the sorption kinetics in the free-standing film. Regression of the water (O-H stretching) diffusion data to the Fickian model (eq 2.9) is represented by the solid line, where the diffusion coefficient was the only adjustable parameter. The regression shown

in Figure 2.15b clearly shows that liquid water diffusion in a crosslinked free-standing film exhibits Fickian behavior. The diffusion behavior shown in Figure 2.15b differs from the diffusion behavior for PIB and PMMA.

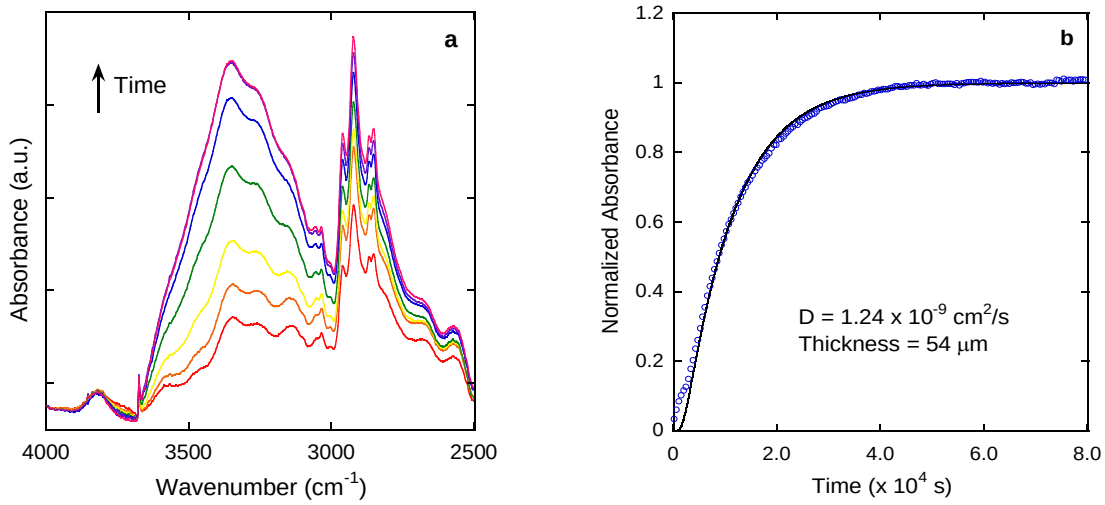

Figure 2.15 Time-resolved infrared spectroscopy data: a) infrared spectra of the water O-H stretching region, showing water diffusion in an epoxy/amine coating free-standing film and b) normalized integrated absorbance of the water O-H stretching region. The solid line represents a regression to the Fickian model (eq 2.9).

This is may be due to the crosslinking present in the epoxy of the crosslinked polymer film. Crosslinking decreases the polymer free volume and suppresses the polymer strain response to the diffusant,[100] which minimizes changes in the polymer due to the stress induced by the diffusant in the nonequilibrium state. The results obtained for the crosslinked polymer indicate that the new pressure-contact apparatus may be a suitable technique for measuring liquid sorption in free-standing films, which in some cases are difficult to adequately solution-cast onto an ATR element.

2.4 Conclusion

Time-resolved FTIR-ATR spectroscopy is a method that allows for accurate collection of liquid sorption kinetics in polymer films. Unlike gravimetric techniques, FTIR-ATR spectroscopy can capture multiple phenomena (diffusion, polymer relaxation, and polymer compression). The *in situ* pressure-contact FTIR-ATR spectroscopy apparatus developed in this work provides accurate measurement of liquid water diffusion in free-standing polymer films. The measurement of liquid diffusion in free-standing polymer films cannot be accomplished with the conventional time-resolved FTIR-ATR spectroscopy technique, because it requires the polymer film to be solution-cast onto the ATR crystal. Liquid transport in a rubber polymer (PIB) using this apparatus showed similar results to those obtained with the conventional solution-cast FTIR-ATR spectroscopy method, demonstrating the pressure-contact apparatus may be suitable to accurately measure sorption kinetics of liquids in free-standing rubbery polymer films.

Non-Fickian behavior was observed for the rubbery (PIB) and glassy (PMMA) polymers in this study, while Fickian behavior was observed for the free-standing crosslinked polymer film. The non-Fickian behavior observed for PIB in this study may be due to the clustering behavior in water due to self-associating hydrogen bonding.[50] The non-Fickian behavior observed for solution-cast PMMA in this study was due to water diffusion and water-induced polymer relaxation occurring on the same time scale, and both of these phenomena were modeled and quantified. Non-Fickian behavior observed for free-standing PMMA in this study was attributed to water diffusion and polymer compression. Diffusion-compression had not been observed *via* ATR before

and therefore a new mathematical model incorporating both of these phenomena was developed to quantify and model the sorption kinetics observed for free-standing PMMA. The Fickian behavior observed for the crosslinked polymer is attributed to a suppression of the polymer strain response. The results obtained for the crosslinked polymer indicates that the *in situ* pressure-contact apparatus may be a suitable technique for measuring liquid sorption in free-standing films (*e.g.*, commercial films).

CHAPTER III

LIQUID WATER TRANSPORT IN POLYMER-IONIC LIQUID MIXTURES

3.1 Introduction

The diffusion (*i.e.*, sorption kinetics) of liquid water in glassy polymers is of interest for the development of materials for multiple applications[1-9] However, due to their nonequilibrium state (i.e., the glass transition temperature of the polymer is much higher than the experimental temperature), difficulties can arise when measuring water sorption in glassy polymers.[29-30] The nonequilibrium state of glassy polymers results in non-Fickian diffusion behavior, where concentration-gradient driven diffusion of water in the polymer results in time-dependent, stress-induced polymer relaxation. [44, 83, 101-102] The relaxation of the polymer chains allow for continuous gradual uptake of water at extended experimental times.[44, 101-102]

Many studies have observed non-Fickian or anomalous diffusion of water in glassy polymers. [15, 35-37, 41, 83, 103-105] Recently, Davis *et al.* [15, 41] studied water vapor and liquid water transport in poly(lactide) (PLA) using quartz crystal microbalance (QCM), quartz spring microbalance (QSM) and Fourier transform infrared-attenuated total reflectance (FTIR-ATR) spectroscopy. Non-Fickian diffusion behavior was observed using all techniques, which is due to the nonequilibrium state of PLA.[15, 41] It was observed that water vapor diffusion in PLA can appear Fickian if the time scale of the sorption step is fast in reference to the polymer film thickness. At longer experimental times, two-stage kinetics, or polymer relaxation would be observed. Additionally, Davis *et al.*[44] studied

water vapor transport in glassy polymer poly(methyl methacrylate) (PMMA) using QSM and FTIR-ATR spectroscopy. As seen with water diffusion in PLA, water diffusion in PMMA has previously been observed to be non-Fickian or two-stage, where the data appears Fickian if the time scale of the sorption step is fast in reference to the polymer film thickness, but at longer experimental times, two-stage kinetics is observed. Sundfors *et al.*[50] studied liquid water sorption in copolymers of methyl methacrylate with n-butyl acrylate, decyl acrylate and isodecyl acrylate using FTIR-ATR spectroscopy. They observed that liquid water diffusion was non-Fickian for all PMMA copolymers, and unlike water vapor sorption, two-stage kinetics was not observed.

The nonequilibrium nature of glassy polymers is attributed to the fact that the glass transition temperature, T_g, is much higher relative to the experimental temperature, leading to anomalous, or non-Fickian diffusion. Since the T_g has a direct effect on diffusion behavior, understanding how T_g affects diffusion (sorption kinetics) can lead to a better understanding of diffusion behavior in glassy polymers. One way to change the T_g of a glassy polymer is by the addition of a plasticizer, *e.g.*, ionic liquid (IL). There is significant interest in ILs because they are non-volatile plasticizers, but more importantly have unique physiochemical properties that make them attractive for a variety of applications, such as supercapacitors, solar cells, fuel cells, sensors, and membranes for gas separations[51-56] Recently, Gwee *et al.*[57] studied the effect of morphology on ion transport in polymer-IL (1-ethyl-3-methylimidazolium bis(trifluoromethylsulfonyl) imide; EMIm-TFSI) mixtures. Ionic conductivity is low at low IL content because of the presence of the polymer, but at high IL content, ionic

conductivity approaches that of that bulk IL.[57] However, plasticization of the polymer results from increasing IL content.[57] This is because as IL content increases, the T_g decreases, causing the polymer-IL mixture to transition from a glassy mixture to a rubbery mixture. Gwee *et al.* [57] found that there was a sharp increase in conductivity in polymer-IL mixtures that contained approximately 0.15 mol ratio IL. They observed that the Tg of this polymer-IL mixture is at room temperature, which was the temperature of the conductivity experiments. The significant increase in conductivity for the PMMA-IL mixtures is due to the transition from a glassy to a rubbery state where the free volume and segmental motion of the PMMA chains increases therefore significantly impacts transport.

In addition to facilitating ion transport, polymer-IL mixtures have also demonstrated high water transport properties.[58] Magana *et al.*[58] studied the impact of imidazolium tetrafluoroborate ILs (IL = EMIm-BF_4) on the water vapor transport properties of Pebax copolymer. They observed that the T_g of the Pebax-IL films decreased with increasing IL content, however every T_g observed was well below the experimental temperature (25 °C), indicating that every Pebax-IL mixture was not in the glassy state. Their results showed that water sorption increased as IL content in the Pebax-IL films increased.[58] The increase in water sorption is due to the fact that as IL increases, T_g decreases, causing the Pebax-IL mixture to transition towards a more equilibrium state (i.e., rubbery phase), where the free volume and segmental motion of the Pebax chains increases, facilitating increased water transport. The effect of water vapor on ionic liquid materials and water vapor uptake in ionic liquid materials has been explored in

literature.[53, 55, 58-62] However, understanding the molecular interactions between water and polymer mixtures of varying T_gs would be of interest for the development of materials for various applications. [26] In this work, liquid water transport in PMMA-IL mixtures with varying concentrations (0 to 50 % w/w) of IL (IL = EMIm-TFSI) was studied using FTIR-ATR spectroscopy. By varying IL content, polymer-ionic liquid films with temperatures above and below the experimental temperature, T, were fabricated. The effect of varying IL concentration of the PMMA-EMIm-TFSI mixture T_g was determined using differential scanning calorimetry (DSC). FTIR-ATR spectroscopy was used to determine the impact of T_g on water diffusion behavior in the PMMA-EMIm-TFSI mixtures.

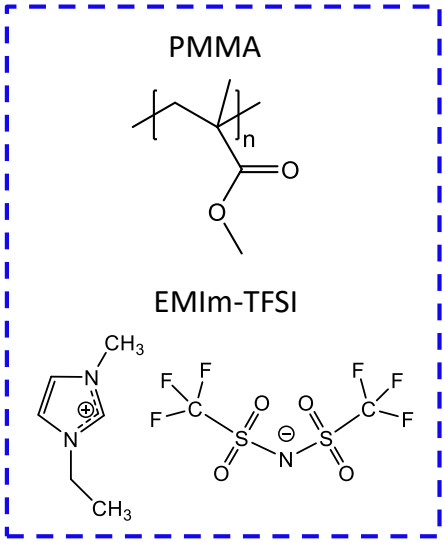

Figure 3.1 Poly(methyl methacrylate) (PMMA) and EMIm-TFSI

3.2 Experimental

3.2.1 Materials

Poly(methyl methacrylate) (PMMA) was purchased from Polysciences, Inc. (M_w = 100,000 kg/mol, atactic beads) and Scientific Polymer Products (M_w = 75,000 kg/mol, powder); chemical structure shown in Figure 3.1. 1-Ethyl-3-methylimidazolium bis(trifuoromethylsulfonyl) imide (EMIm-TFSI) (mol. wt. = 391.31 g/mol; 99% purity) was purchased from Io-li-tec; chemical structure shown in Figure 3.1. Nitrogen (N_2) gas was purchased from Airgas and used for polymer film fabrication. Tetrahydrofuran (THF; anhydrous, ≥ 99.9% inhibitor-free) was purchased from Sigma Aldrich. Deionized water (resistivity ca. 16 MΩ) was used for all experiments.

3.2.2 Film Preparation

PMMA/THF solutions for film fabrication were prepared by dissolving PMMA (M_w = 100,000 kg/mol, atactic beads) in THF at 5 % w/w and mixing for 24 h to ensure clear, homogenous solutions. The PMMA films were fabricated by drop casting the solution onto an ATR crystal surface at room temperature for 24 h and then holding under vacuum at room temperature for 24 h. The PMMA films were then annealed under vacuum at 70 °C for 3 h and then at 120 °C for an additional 3 h. PMMA/EMIm-TFSI/THF solutions for film fabrication were prepared by dissolving PMMA (M_w = 75,000 kg/mol, powder) in THF at 5 % w/v and mixing for 24 h to ensure clear, homogenous solutions. After stirring for 24 h, a specified amount of EMIm-TFSI was added to the solutions and allowed to stir for an additional 2 h to form a clear,

homogeneous solution. Films were then fabricated by drop casting each solution onto an ATR crystal surface under nitrogen atmosphere for 2 days at 50 °C. The films were then annealed under vacuum at 110 °C for 2 days. The thickness of each polymer film was measured before each experiment with a digital micrometer (Mituyo, 1 μm accuracy).

3.2.3 Differential Scanning Calorimetry

Glass transition temperatures (T_gs) were determined by differential scanning calorimetry (DSC, TA Instruments, Q200) over a temperature range of -40 to 180 °C, at a heating/cooling rate of 10 °C/min under a N_2 environment using a heat/cool/heat method. The T_g was determined using the midpoint method from the second thermogram heating cycle.

3.2.4 Time-Resolved FTIR-ATR Spectroscopy

Time-resolved infrared spectra were collected for all water diffusion experiments using an FTIR spectrometer (Nicolet 6700 Series; Thermo Electron). PMMA and PMMA-EMIm-TFSI films were solution cast onto a multiple reflection, trapezoidal zinc selenide (ZnSe, refractive index = 2.4, Specac Inc.) ATR crystals with 45° beveled faces. The polymer-coated ATR crystal was mounted and sealed in a horizontal, temperature-controlled ATR cell (Specac, Inc.) with a Kalrez gasket. FTIR-ATR experiments were conducted at 25 °C, controlled *via* a temperature jacket (circulated water bath) on the ATR flow through cell. Prior to each experiment, the polymer-coated ATR crystal was equilibrated at 25 °C for approximately 4 h, with dry air flowing across the polymer

surface. Right before the start of the experiment, the dry air was removed and the space in the ATR cell above the polymer film (V = 550 µL) was filled with DI water *via* pipette and sealed to prevent evaporation.

As water diffused from the water/polymer side to the polymer/crystal side, time-resolved spectra were collected in the region close to the polymer/crystal interface to quantify the diffusion of water through the polymer film. Spectra for all diffusion experiments were corrected by a background subtraction of the ATR crystal spectrum and were collected using a liquid nitrogen-cooled mercury-cadmium-telluride (MCT) detector with 32 scans per spectrum at a data spacing of 2 cm^{-1} resulting in spectrum collected every 19 seconds. More details regarding the experimental apparatus and procedures can be found in Chapter 2.

3.3 Results and Discussion

Figure 3.2 shows the infrared spectra of EMIm-TFSI and solution cast PMMA, and PMMA-EMIm-TFSI (41 % w/w IL) films before exposure to water. The key infrared bands that appear in Figure 3.2 are listed in Table 3.1. [91-99, 106]

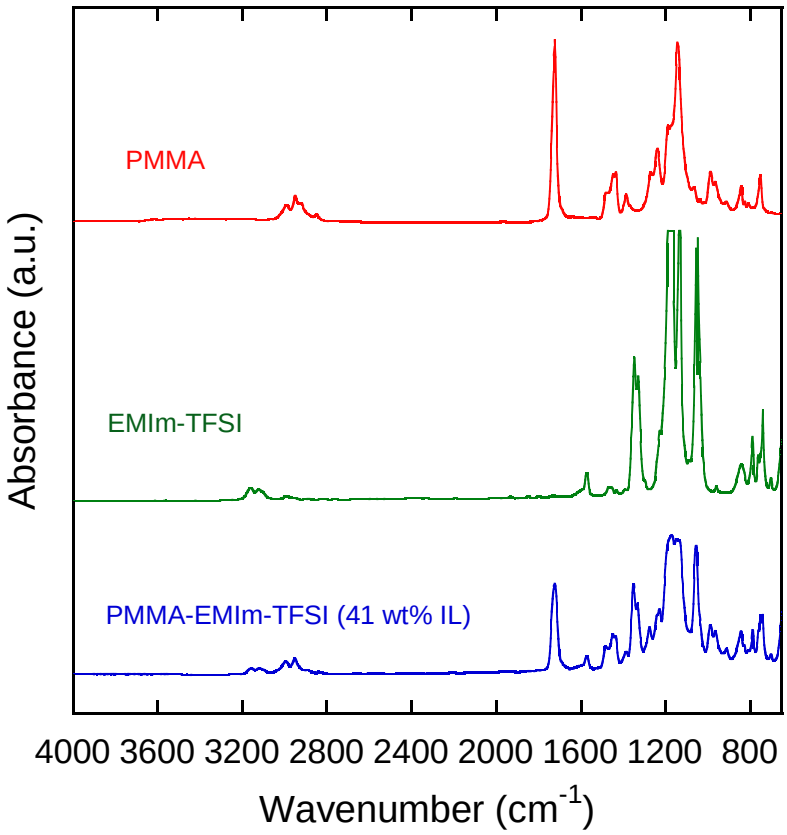

Figure 3.2 Infrared spectra of PMMA, EMIm-TFSI, and PMMA-EMIm-TFSI (41 % w/w ionic liquid). Spectra are offset for clarity.

Table 3.1 Infrared Band Locations for PMMA and PMMA-EMIm-TFSI.

Bond Vibrations	Band Location (cm^{-1})	References
H-C-C-H ring asymmetric, ring in plane symmetric stretch	3163	106-107
CH stretching, CH_3 asymmetric stretching	2900, 2927, 2951, 2960	91-92, 94, 96-99
C=O stretching	1723	91, 93-99
OH bending/deformation	1650	91
ring in-plane CH_2(N)/CH_3(N) symmetric/asymmetric stretching	1577	106-108
CH_3 asymmetric stretching	1483	92, 97
CH_3, CH_2 stretching	1446	94-97
O-CH_3 deformation, CH_3 stretching	1434	92, 97-98
O-CH_3, CH_3 stretching	1386	92, 94, 97, 99
ring symmetric stretch, CH_3 (N) stretch, CH_2 (N) stretch, CF_3 asymmetric stretch	1177	106-108
Ring in plane asymmetric stretch, (N) CH_2 and (N)CH_3CN stretch, C-C stretch	1168	106-108
- C-O stretching, C-CH_3 stretching, and COC vibration	1062, 1143, 1195, 1238, 1272	92-99
CH_3, CH_2 stretching	841	94, 96-97, 99
C-C backbone skeletal vibration	750	96-97, 99

Figure 3.3 shows the glass transition temperatures of the polymer-ionic liquid mixture films measured by DSC. The PMMA-EMIm-TFSI mixtures exhibit decreasing glass transition temperatures with increasing ionic liquid content. The dotted line represents

the Fox-Flory equation, which predicts the glass transition temperature for a miscible system from pure component glass transition temperatures (eq 3.1):[108]

$$\frac{1}{T_g} = \frac{w_1}{T_{g,1}} + \frac{w_2}{T_{g,2}} \tag{3.1}$$

where w_1 and w_2 are the weight fractions of EMIm-TFSI and PMMA respectively, and $T_{g,1}$ and $T_{g,2}$ and T_g are the glass transition temperatures of EMIm-TFSI, PMMA, and the mixture, respectively. $T_{g,1}$ and $T_{g,2}$ are -87 and 97 °C, respectively.[108-109] Table 3.2 shows the T_gs for PMMA-EMIM-TFSI determined by DSC and predicted by the Fox-Flory equation (eq 3.10).

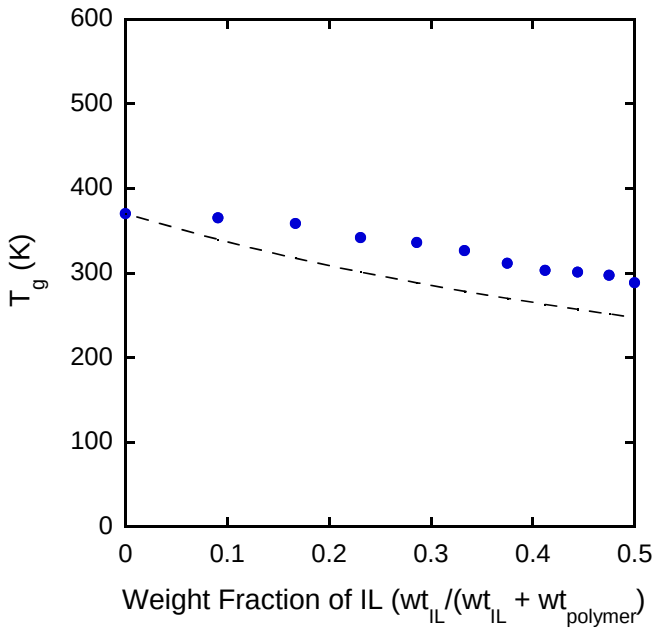

Figure 3.3 Glass transition temperatures of PMMA-EMIm-TFSI (0, 9, 16, 23, 28, 33, 37, 41, 33, 47, and 50 % w/w IL), where the dotted line represents a regression to the Flory-Fox Equation (eq 3.1).

Table 3.2 Glass Transition Temperatures for PMMA-EMIm-TFSI.

IL (wt fraction)	T_g (K)	T_g-T (K)	T_g (Flory Fox) (K)
0	370	72	370
0.091	365	67	339
0.167	358	61	317
0.231	342	44	301
0.286	336	38	288
0.333	326	28	278
0.375	311	13	269
0.412	303	8	263
0.444	301	3	257
0.475	297	-1	251
0.5	287	-9	247

The time resolved infrared spectra of the O-H stretching region of water in PMMA and the CH_3 stretching region of PMMA is shown in Figures 3.4a and b, respectively. Figure 3.4a shows the intensity of the infrared spectra of the water O-H stretching region increasing with time, indicating the diffusion of water into PMMA. Figure 3.4b shows the intensity of the infrared spectra of the CH_3 stretching region of PMMA decreasing with time. The normalized integrated absorbance of the bands for the OH stretching of water and the CH_3 stretching of PMMA is shown in Figure 3.4c. In Figure 3.4c, the integrated absorbance of each band is normalized to their final value. Regression of the

water (O-H stretching) diffusion data to the Fickian model (eq 2.9) is represented by the solid line, where the diffusion coefficient was the only adjustable parameter.

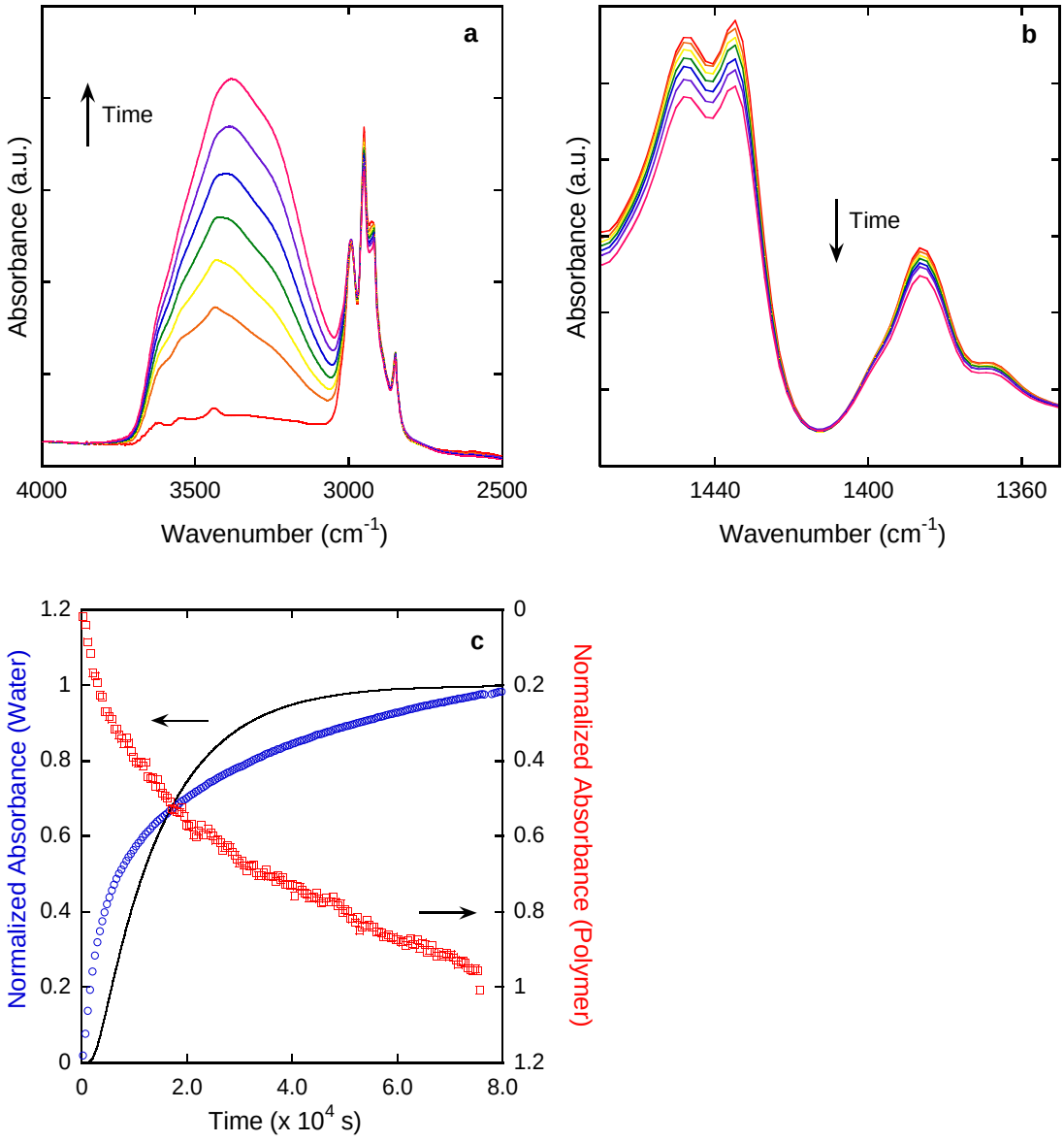

Figure 3.4 Infrared spectra of the (a) O-H stretching region, and (b) the CH_3 stretching region of PMMA at 25 °C. (c) Normalized, integrated absorbance of the OH stretching of water (blue circles) and the ester stretching (red squares) as a function of time at 25 °C. The line represents a regression to the Fickian model (eq 2.9).

The regression shown in Figure 3.4c clearly indicates that liquid water diffusion in PMMA is not adequately described by the Fickian model. Non-Fickian sorption profiles (*via* gravimetry and ATR) for transport in glassy polymers similar to that shown in Figure 4c have also been observed in other studies.[15, 42] The non-Fickian behavior observed in Figure 3.4c has been associated with diffusion and polymer relaxation occurring at similar time scales. The concentration gradient of the liquid water, the diffusant, is the driving force for diffusion while polymer relaxation is the response to the stress imposed by the diffusant. Figure 3.4c shows both of these phenomena.

In order to describe the sorption kinetics of liquid water in the polymer ionic liquid mixtures, the polymer relaxation was examined. In Chapter 2, for the diffusion of liquid water in PMMA using FTIR-ATR spectroscopy, the CH_3 stretching absorbance band associated with the polymer was quantified as a function of time as a measure of the polymer relaxation, and this data was regressed to a three-element viscoelastic model (eq 2.17) to obtain a relaxation time constant, β. The non-Fickian water diffusion data was then regressed using a diffusion-relaxation model (eq 2.18) to obtain a diffusion coefficient, D. Similarly, the CH_3 stretching absorbance band (1386 cm^{-1}) associated with the polymer-ionic liquid mixtures (Figure 3.4b) was quantified using eq 2.17 and is shown in Figure 3.5a, where the relaxation time constant, β, is 1.29 x 10^{-4} s^{-1}. Based on Figure 3.5a, it appears that the viscoelastic model agrees with the data. Using this data, the non-Fickian water-diffusion data (Figure 3.4a) was regressed using the diffusion-relaxation model (eq 2.18). The full regression of the water diffusion data to the

diffusion-relaxation model (solid line) is shown in Figure 3.5b, where the diffusion coefficient, D, is 2.6 x 10^{-9} cm^2/s.

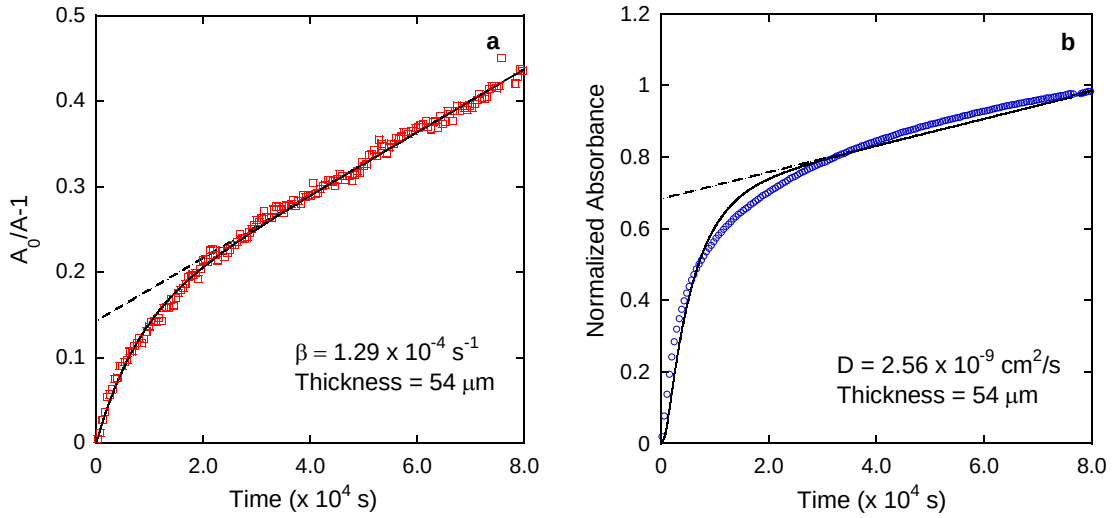

Figure 3.5 (a) Regression of the time-resolved PMMA CH_3 stretching infrared absorbance data (red squares) to the polymer relaxation model at 25 °C. The dashed and solid lines represent the late-time linear solution and full solution (eq 2.17), respectively, where the relaxation time constant, β, was the only fitting parameter for the full regression. (b) Regression of the time-resolved O-H stretch stretching infrared absorbance data (blue circles) to the diffusion-relaxation model at 25 °C for PMMA. The dashed and solid lines represent the late-time linear solution and full solution (eq 2.18), respectively, where the diffusion coefficient of water, D, was the only fitting parameter for the full regression.

The time resolved infrared spectra of the O-H stretching region of water and the CH_3 stretching region of PMMA-EMIm-TFSI (41 % w/w IL) is shown in Figures 3.6a and b, respectively. Figure 3.6a shows the intensity of the infrared spectra of the water O-H stretching region increasing with time, indicating the diffusion of water into PMMA-EMIm-TFSI. Figure 3.6b shows the intensity of the infrared spectra of the CH_3

stretching region of PMMA-EMIm-TFSI decreasing with time. The normalized integrated absorbance of the bands for the OH stretching of water and the CH_3 stretching of PMMA-EMIm-TFSI is shown in Figure 3.6c. Like Figure 3.4c, the integrated absorbance of each band is normalized to their final value. Regression of the water (O-H stretching) diffusion data to the Fickian model (eq 2.9) is represented by the solid line, where the diffusion coefficient was the only adjustable parameter. The regression shown in Figure 3.6c shows that liquid water diffusion in 41 % w/w PMMA-EMIm-TFSI (T_g = 30 °C) exhibits behavior that is more Fickian than the sorption kinetics shown in Figure 4.4c for PMMA (T_g = 97 °C) The T_g of PMMA is much higher and farther from the experimental temperature, T (25 °C), than the T_g of 41 % w/w PMMA-EMIm-TFSI. Since the T_g of 41 % w/w PMMA-EMIm-TFSI is so close to the experimental temperature, T, it is closer to an equilibrium state than PMMA, making water diffusion behavior less anomalous or non-Fickian, and exhibiting more Fickian behavior. This is because as T_g decreases and approaches the experimental temperature, the free volume of the polymer increases and the polymer becomes more rubbery, and approaches a more equilibrium state.

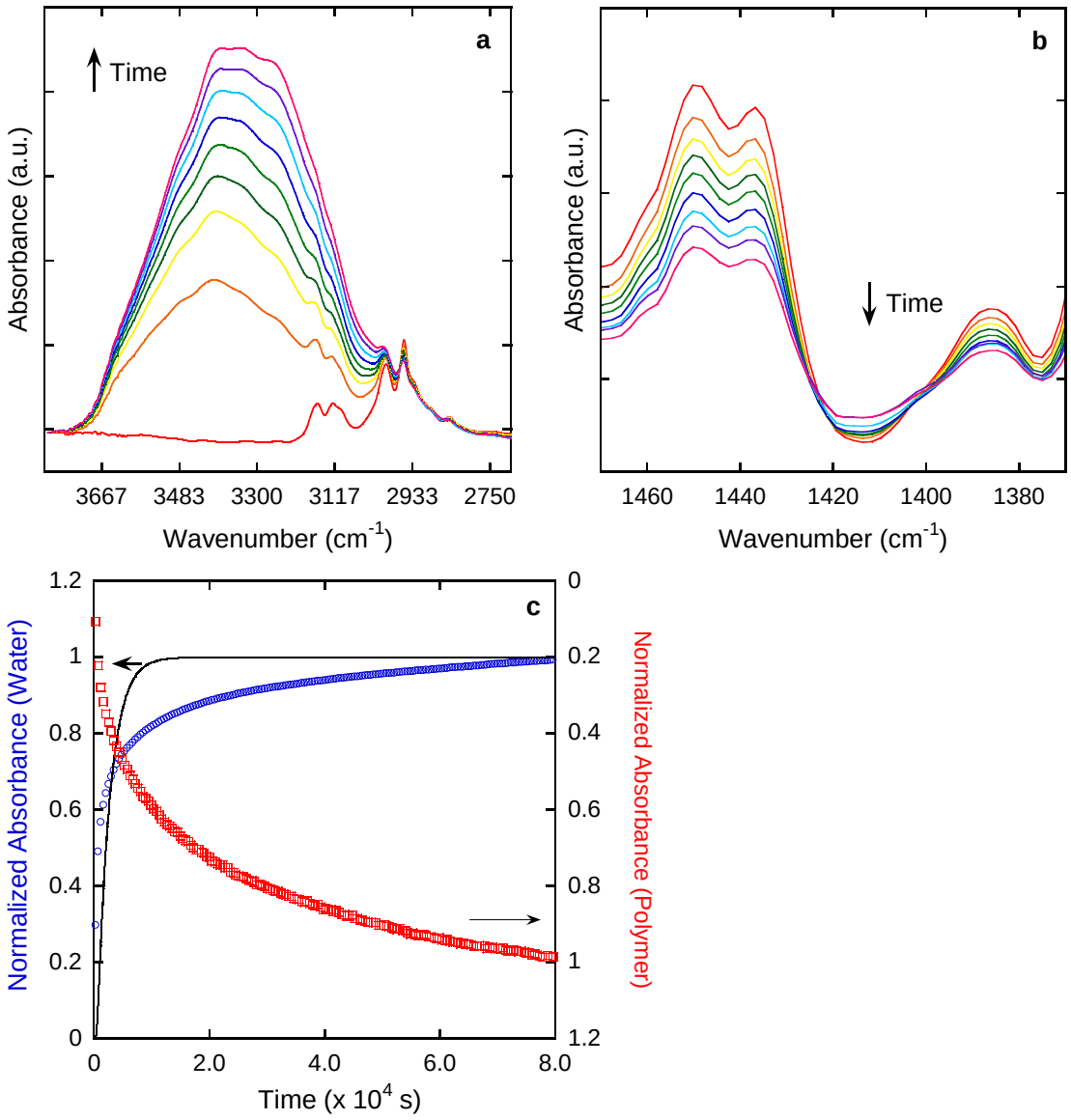

Figure 3.6 Infrared spectra of the (a) O-H stretching region, and (b) the CH_3 stretching region of PMMA-EMIm-TFSI (41 % w/w IL) at 25 °C. (c) Normalized, integrated absorbance of the OH stretching of water (blue circles) and theCH_3 stretching (red squares) as a function of time at 25 °C. The line represents a regression to the Fickian model (eq 2.9).

Figure 3.7a shows the regression of CH_3 stretching absorbance of the polymer using the three-element viscoelastic model (eq 2.17) described in Chapter 2, where the

relaxation time constant, β, is 1.13 x 10^{-4}. Using this data, the non-Fickian water-diffusion data (Figure 3.6a) was regressed using the diffusion-relaxation model (eq 2.18). The full regression of the water diffusion data to the diffusion-relaxation model (solid line) is shown in Figure 3.7b, where the diffusion coefficient, D, is 2.99 x 10^{-8} cm^2/s.

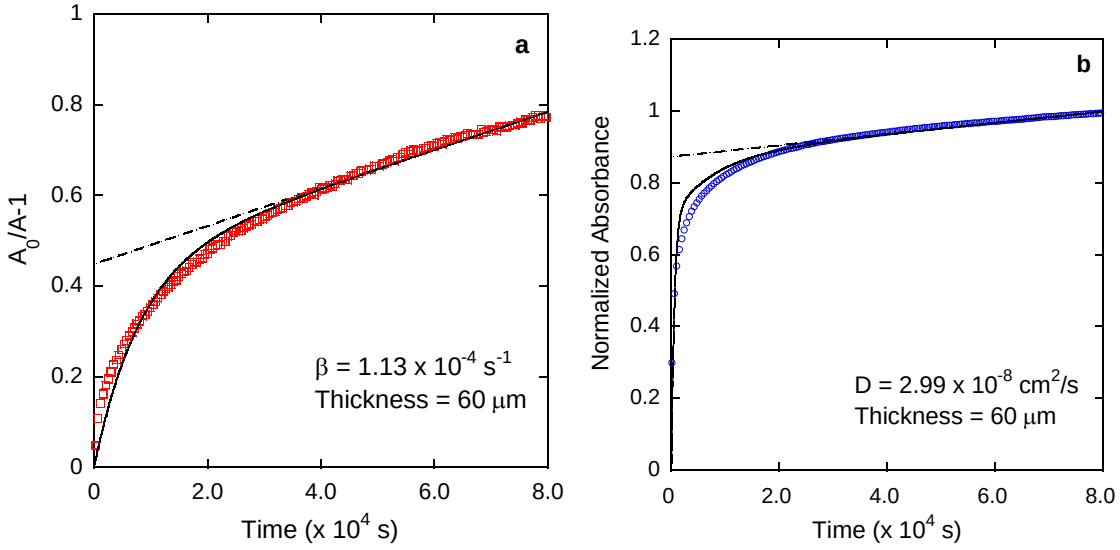

Figure 3.7 (a) Regression of the time-resolved PMMA-EMIm-TFSI (41 % w/w IL) CH_3 stretching infrared absorbance data (red squares) to the polymer relaxation model at 25 °C. The dashed and solid lines represent the late-time linear solution and full solution (eq 2.17), respectively, where the relaxation time constant, β, was the only fitting parameter for the full regression. (b) Regression of the time-resolved O-H stretch stretching infrared absorbance data (blue circles) to the diffusion-relaxation model at 25 °C for PMMA-EMIm-TFSI (41 wt% IL). The dashed and solid lines represent the late-time linear solution and full solution (eq 2.18), respectively, where the diffusion coefficient of water, D, was the only fitting parameter for the full regression.

Figure 3.8 shows a plot of the normalized absorbance of the OH stretch for each PMMA-EMIm-TFSI mixture versus time, and it shows that as IL content increases, the water diffusion behavior becomes more Fickian. As IL content increases, or T_g of the PMMA-EMIm-TFSI mixture decreases relative to the experimental temperature, the water diffusion behavior deviates from the expected anomalous behavior. Figure 3.8 shows that for IL content of 37 % w/w and higher, the water diffusion behavior differs significantly from the PMMA-EMIm-TFSI mixtures of 0-33 % w/w. This is due to the fact that the glass transition temperatures of 37, 41, 44, 47, and 50 % w/w IL are close or less than the experimental temperature, T. The water diffusion behavior exhibited in Figure 3.8 is the transition from glassy to rubbery.

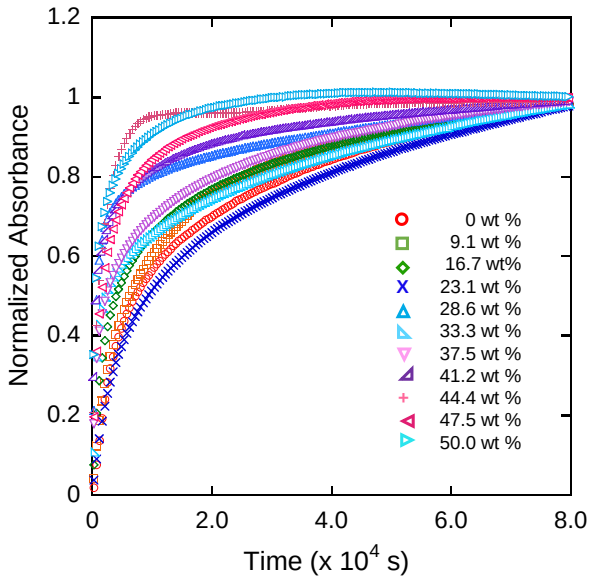

Figure 3.8 Time-resolved FTIR-ATR spectroscopy data; normalized, integrated absorbance of the OH stretching band in PMMA at room temperature for % w/w IL contents of 0, 9, 16, 23, 27, 33, 37, 41, 44, 47, 50 % w/w.

To better understand the absorbance trends shown in Figure 3.8, the diffusion-relaxation model was applied to all water diffusion experiments to determine a relaxation time coefficient, β, and diffusion coefficient, D, for each PMMA-EMIm-TFSI mixture. However because the nonequilibrium nature of the polymer-ionic liquid mixture changes as IL content increases, or T_g decreases, the diffusion relaxation model could not be accurately applied to water diffusion in PMMA-EMIm-TFSI mixtures of 44, 47, and 50 % w/w. This is because as seen in Table 3.2, as IL content increases, the T_g approaches and decreases below the experimental temperature, T. This change in T_g caused a transition in the PMMA-EMIM-TFSI mixtures from the glassy to the rubbery state. Furthermore, since the T_gs of these polymer-ionic liquid mixtures are not significantly above or below the experimental temperature, the polymer-ionic liquid mixtures with IL content 44, 47 and 50 % w/w are in a transition state between the glassy and rubbery state. As the polymer approaches equilibrium, the free volume and segmental motion of the PMMA chains increases, causing water sorption to approach Fickian behavior. The Fickian model was used to determine diffusion coefficients for those polymer-ionic liquid mixtures. The diffusion time ($\tau_D \approx L^2/D$) and the relaxation time ($\tau_R \approx 1/\beta$) were calculated using the diffusion coefficients and relaxation time constants determined using the diffusion-relaxation model. The Deborah number, D*e*, was determined by taking the ratio of both of these times. The values for β, D, τ_D, τ_R, D*e*, and F_A are shown in Table 3.3. The values for the relaxation time coefficient and relaxation time, β and τ_R, respectively, are relatively constant with varying IL content. The diffusion time, τ_D, decreases with increasing IL content. Table 3.3 shows that as IL

content increases, or as the T_g decreases, the values for F_A are relatively constant until it reaches 41 w/w %. The values for D, and D*e* increase with increasing IL content, or decreasing T_g.

Table 3.3 Diffusion-Relaxation Model Results for Water Diffusion in PMMA and PMMA-IL at 25 °C.

w/w % IL	T_g-T (K)	F_A	$\beta \times 10^5$ (1/s)	D x 10^9 (cm^2/s)	τ_R (s)	τ_D (s)	D*e*
0	72	0.59	12.4	2.9	8077	11601	0.7
9.1	67	0.61	6.9	2.6	17238	14398	1.2
16.7	61	0.61	13.3	5.8	7528	5829	1.2
23.1	44	0.55	8.8	4.2	11435	9768	1.3
28.6	38	0.57	10.7	6.9	9397	6789	1.4
33.3	28	0.55	19.0	20.8	5319	2093	2.4
37.5	13	0.61	11.1	13.3	9019	2711	3.3
41.2	8	0.72	9.9	38.0	10315	1119	9.4
44.4	3	0.78	11.1	16.9	9469	3240	3.5
47.5	-1						
50.0	-9						

Figure 3.9 shows the data from Table 3.3 plotted versus T_g-T. Figure 3.9a is a plot of F_A versus T_g-T, showing that F_A is relatively constant with increasing IL content (decreasing T_g) up until 41 % w/w IL and then increases as IL content increases to 47 w/w%. F_A is the weighing fraction for diffusion, and so an increase in F_A indicates that water diffusion approaches Fickian behavior, since Fickian behavior occurs when F_A is 1. Figure 3.9b is a plot of β versus T_g-T, demonstrating that the values for the relaxation

time, β, are relatively constant with varying IL content. Figure 3.9c shows the diffusion coefficient, D, plotted versus T_g-T. The blue dots are diffusion coefficients obtained using the diffusion-relaxation model and the red dots for PMMA-EMIm-TFSI mixtures of 44, 47, and 50 % w/w are diffusion coefficients obtained using the Fickian model. Figure 3.9c shows that the diffusion coefficient increases with increasing IL content, up until 41 % w/w IL. At 44 % w/w IL, the diffusion coefficient obtained using the diffusion-relaxation model decreases significantly, and is close to the diffusion coefficient obtained using the Fickian model. This is attributed to the transitional state (*i.e.*, glassy to rubbery state) mentioned earlier with increasing IL. For 44, 47, and 50 % w/w IL, the diffusion coefficients obtained using the Fickian model are relatively constant. Figure 3.9d is a plot of the relaxation time, τ_R versus T_g-T. Like the data shown in Figure 3.9b, τ_R is relatively constant with varying IL content. Figure 3.9e shows a plot of the diffusion time, τ_D versus T_g-T, where τ_D was calculated based on the diffusion coefficients calculated using the diffusion-relaxation model. The diffusion time, τ_D, decreases with increasing IL content, or decreasing T_g. Figure 3.9f is a plot of the Deborah number, D*e*, versus T_g-T. Since De is a ratio between τ_R and τ_D, as IL content increases (up until 41 % w/w IL) or T_g decreases, D*e* increases. τ_D decreases because as IL increases, and T_g decreases (polymer approaches an equilibrium state), the free volume and segmental motion of the PMMA chains increases, facilitating increased water transport, where water sorption kinetics approaches Fickian behavior.

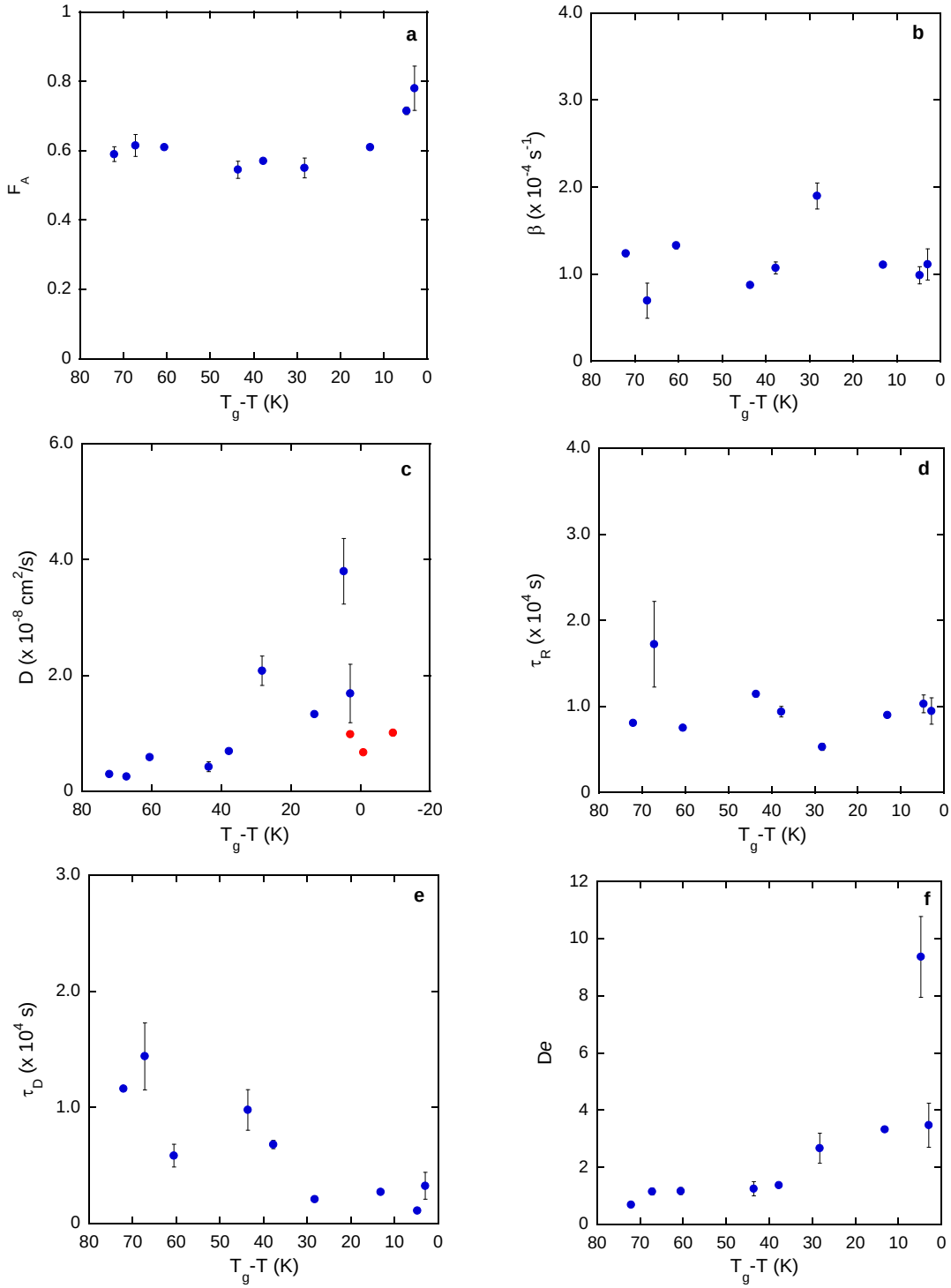

Figure 3.9 (a) F_A, (b) β (s^{-1}), (c) D (cm^2/s) (where solid red circles refer to diffusion coefficients for 44, 47, 50 w/w % IL regressed to Fickian model), (d) τ_R (s), (e) τ_D (s), and (f) D*e* for IL contents of 0, 9, 16, 23, 27, 33, 37, 41, 44 w/w % versus T_g –T .

3.4 Conclusions

In this study, time-resolved FTIR-ATR spectroscopy was used to elucidate the effect of T_g on liquid water diffusion in glassy polymer-ionic liquid mixtures (PMMA-EMIm-TFSI). This work demonstrated that the addition of ionic liquid lowers the glass transition temperature of the polymer-ionic liquid mixture and changes liquid water diffusion behavior. The non-Fickian behavior was observed for PMMA-EMIm-TFSI mixtures of 0 to 41 % w/w IL was modeled and quantified using a diffusion-relaxation model. Results from the diffusion-relaxation model indicated that after 41 % w/w IL, F_A increased, indicating that water diffusion became more Fickian as IL content increased. The relaxation time and the relaxation time constant remained constant with varying IL content. The diffusion time decreased with increasing IL content. The diffusion coefficient and the Deborah number increased with increasing IL content. While non-Fickian behavior was observed for all PMMA-EMIm-TFSI mixtures in this study, as the glass transition temperature approached and decreased below the experimental temperature, diffusion behavior became less non-Fickian, approaching Fickian-like behavior. The water diffusion data for PMMA-EMIm-TFSI mixtures of 44, 47, and 50 % w/w could not be adequately modeled using the diffusion-model and were modeled using the Fickian model. This is attributed to the fact that as T_g decreases, the free volume of the polymer increases and the polymer approaches equilibrium.

CHAPTER IV

HIGHLY POROUS TI_4O_7 REACTIVE ELECTROCHEMICAL WATER FILTRATION MEMBRANES FABRICATED *VIA* ELECTROSPINNING/ELECTROSPRAYING[*]

4.1 Introduction

Effective water treatment technologies need to treat a broad range of water contaminants, which typically is accomplished by using multiple technologies in a treatment train. In order to reduce the cost and complexity of water treatment, research has focused on the development of novel technologies that can incorporate multiple treatment methods into a single technology. Recent work has focused on the integration of membrane filtration with electrochemical advanced oxidation processes (EAOPs) to create a hybrid technology known as reactive electrochemical membranes (REMs).[12-13] This novel REM technology utilizes a ceramic porous substoichiometric Ti_nO_{2n-1} ($4 < n < 6$) material (known as Magnéli phases) that can serve as both a membrane for filtration and a reactive electrode surface that can oxidize contaminants by a combination of hydroxyl radical ($OH^{\bullet}$) production from water oxidation and direct electron transfer reactions.[12-13]

The REMs are synthesized by the conversion of nonconductive TiO_2 precursors to conductive Magnéli phases, where Ti_4O_7 is the most electrically conductive phase. Due

[*] Reprinted with permission from "Highly Porous Ti4O7 Reactive Electrochemical Water Filtration Membranes Fabricated via Electrospinning/Electrospraying" by M.C.Santos, Y. Jing, L. Fang, B.P. Chaplin, and Y.A.Elabd, 2015. *AIChE Journal.*62, 508-524, Copyright 2015 by the American Institute of Chemical Engineers.

to their stability under anodic polarization and resistant to oxidation and corrosion,[71-72, 110-111] conductive Ti_4O_7 electrodes have been utilized for the cathodic protection of metal structures[110] and electrodes for a variety of applications, including lead-acid batteries,[112-113] rechargeable zinc-air batteries,[71-72] and fuel cells.[111, 114-116]

While only few studies have been reported on the use of Ti_4O_7 for water purification,[12-13, 117-122] Zaky and Chaplin[12-13] have expanded the use of Ti_4O_7 for water treatment by utilizing it as a REM to study the removal of a series of *p*-substituted phenolic compounds that were used as model organic contaminants. In their studies, they demonstrated that the REM was active for both direct anodic oxidation and generation of $OH^{\bullet}$ that resulted in efficient removal of phenolic compounds.[12-13] Although the porous rigid cylindrical REM used in these studies was effective, it had a limited morphology (*e.g.*, limited porosity, geometry, flexibility) for filtration experiments. In order to expand the potential applications of REMs for water treatment, it is desirable to develop flexible REMs with tailored porosities that will facilitate the development of new hybrid membranes for use in compact filtration systems (*e.g.*, spiral wound membrane modules and point-of-use devices).

Towards this goal, a simultaneous electrospinning and electrospraying method was pursued to develop Ti_4O_7 REMs that are highly porous, flexible, durable, and inexpensive. Simultaneous electrospinning and electrospraying is a recent method that can fabricate highly porous membranes by electrospinning organic polymer nanofibers and electrospraying inorganic nanoparticles in tandem from two separate needles (see Figure 4.1). The resulting membranes produced from this method result in a network of

nanofibers and nanoparticles with intimate contact between both materials throughout the porous matrix, where changing the various electrospinning and electrospraying parameters and solution properties allows for membranes with various porosities, fiber sizes, and particle sizes. Membranes fabricated from the electrospinning/electrospraying (E/E) method have recently been explored in a variety of applications, including batteries,[123] tissue engineering,[124-129] fuel cells,[130-131] composites,[132-134] and water purification.[133, 135-137] To date, few studies have explored the E/E method to develop membranes for water purification and to our knowledge studies have not been conducted that have utilized the E/E method to develop REMs.

In this study, the simultaneous E/E method was employed to fabricate highly porous REMs consisting of poly(sulfone) (PSU) fibers and Ti_4O_7 particles using the two needle system shown in Figure 4.1. PSU is a commonly used polymer in filtration membranes[137-140] and Ti_4O_7 has previously been used for REMs due to its high conductivity and corrosion resistant properties.[71-72, 110] Characterization of the E/E REMs was performed using X-ray diffraction (XRD), scanning electron microscopy (SEM), and Hg porosimetry analysis. The electrochemical properties and water filtration performance of these E/E REMs were evaluated using electrical impedance spectroscopy (EIS), cyclic voltammetry (CV), and cross-flow filtration experiments.

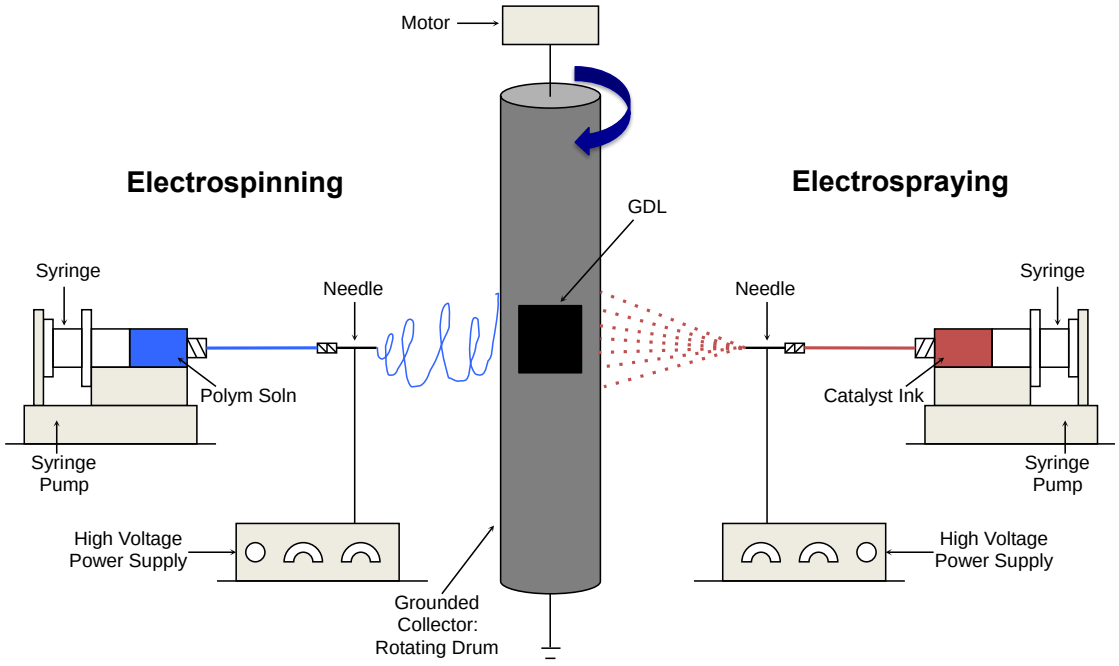

Figure 4.1 Schematic of simultaneous electrospinning/electrospraying (E/E) apparatus. Figure adapted from ref [131].

4.2 Experimental

4.2.1 Materials

TiO_2 (99.9%, 32 nm particles) nanopowder was purchased from Alfa Aesar. Ethanol (EtOH) (≥99.997%, anhydrous), poly(sulfone) (PSU; average M_n ~ 22,000 g/mol, beads), and dichloromethane (DCM) (≥99.8%, anhydrous) were purchased from Sigma Aldrich. High purity H_2 gas was purchased from Airgas and was used for Ti_4O_7 powder synthesis. Carbon cloth gas diffusion layers (GDL; ELAT LT 1400W and ELAT H) were purchased from Fuel Cells Etc. and were used as received for membrane fabrication. All other chemicals were reagent-grade and obtained from Sigma-Aldrich or Fisher and were used as received. All solutions used in this study were made using

deionized water obtained from a NANOPure water purification system (Barnstead) with resistivity greater than 18 MΩ·cm (25 °C).

4.2.2 Ti_4O_7 Synthesis and Structural Characterization

Ti_4O_7 powder was prepared by reducing TiO_2 nanopowder in H_2 gas at 950 °C in a tube furnace (Mode F21135, Barnstead Thermolyne) for 4 hrs.[72] The chemical reaction for the production of Ti_4O_7 is given:[110]

$$4TiO_2 + H_2 \rightarrow Ti_4O_7 + H_2O \quad (4.1)$$

X-ray diffraction (XRD; Bruker-D8 Advanced, Bragg Bentano) powder experiments were performed to quantify and characterize the Ti_4O_7 Magnéli phase. XRD patterns were collected from 15°-70° 2θ with a scan rate of 0.3 °/s. Scanning electron microscopy (SEM, FEI Quanta 600 FE-SEM) was used to characterize the morphology of the Ti_4O_7 powder. Samples were sputter coated (Cressington 208 HR) with platinum at 40 mV to achieve a 6 nm layer thickness before SEM images were collected. SEM images of the Ti_4O_7 powder were collected at 10 kV.

4.2.3 Simultaneous Electrospinning/Electrospraying (E/E) System

A schematic of the simultaneous electrospinning/electrospraying (E/E) apparatus used is shown in Figure 4.1.[131] The apparatus consists of two high-voltage sources (Model PS/EL50R00.8, Glassman High Voltage, Inc. and Model ES40P-10W/DAM, Gamma High Voltage Research, Inc.), two syringe pumps (Model NE-1000, New Era Pump Systems), tubing (EW-30600-65, Cole Parmer and Pt. No. 86510, Hamilton), luer lock

needle adaptors (Pt. No. 86511, Hamilton), two syringe needles (i.d. = 0.061 cm, Pt. No. 90520, Hamilton), two syringes (CG-3070-03, Chemglass Life Sciences), and a grounded collector consisting of an aluminum foil covered cylindrical drum connected to a motor (Model 4IK25GN-SW2, Oriental Motor). The motor allows for drum (o.d. = 4.85 cm) rotation during E/E experiments and was set at 100 rpm. GDLs were cut into 5 cm x 5 cm pieces, and four GDL pieces were adhered onto the drum for each E/E experiment. E/E experiments consisted of simultaneously electrospinning a PSU/DCM solution and electrospraying a Ti_4O_7/EtOH solution. For the electrospinning process, the needle tip to collector distance, applied voltage, and solution flow rates were 12 cm, 12 kV, and 0.9 ml/h, respectively. For the electrospraying process, the needle tip to collector distance, applied voltage, and solution flow rates were 9 cm, 15 kV, and 3 ml/h, respectively.

4.2.4 Membrane Fabrication

PSU solutions for electrospinning were prepared by dissolving 1 g of PSU in 10 g of DCM to produce a 9.1 wt% PSU/DCM solution. The polymer solutions were mixed for 24 hrs to ensure homogeneity. The Ti_4O_7 solutions for electrospraying were prepared by dissolving 0.25 g of Ti_4O_7 powder in 9.75 g of EtOH to produce a 2.5 wt% Ti_4O_7/EtOH solution. The Ti_4O_7 solution was then sonicated for 15 min (Model Cl-18, QSonica Sonicator). The Ti_4O_7 and PSU solutions were used for E/E experiments. E/E experiments were conducted over the course of 6 hrs using either the ELAT LT1400W or the ELAT H GDLs as a substrate collector on the drum. ELAT LT1400W and ELAT

H are woven carbon cloth membranes. The ELAT LT 1400W GDL has a thickness of 454 μm, 63% porosity, is poly(tetrafluoroethylene) (PTFE) treated and has a microporous carbon layer covering the woven carbon cloth. The ELAT H GDL has a thickness of 406 μm, 80% porosity, is not PTFE treated, and does not have a microporous carbon layer covering the woven carbon cloth. The ELAT LT 1400W and ELAT H GDLs were used because they provided structural support for the E/E and solution cast PSU/Ti_4O_7 membranes, and were durable, flexible, and highly conductive. In this study, the ELAT LT 1400W and ELAT H GDLs will be referred to as ELAT 1 and ELAT 2, respectively. E/E experiments were also conducted over the course of 2 days using the ELAT H GDL (ELAT 2) to compare to the shorter 6 hr deposition E/E membranes. Several of the E/E membranes were annealed at 200 ºC for 2 hrs to investigate the impact of annealing. The resulting filtration membranes consisted of GDL coated with a layer of electrospun PSU nanofibers and electrosprayed Ti_4O_7 particles. These materials will be referred to as E/E membranes.

As a comparative control sample, PSU/Ti_4O_7 solutions were cast onto GDLs. The PSU/Ti_4O_7 solution used to create these solution cast membranes were prepared by dissolving 1 g of PSU in 10 g of DCM for 24 hrs to produce a 9.1 wt% PSU/DCM solution. The solution was mixed for 24 hrs to ensure homogeneity. Then 0.25 g of Ti_4O_7 was added to the solution and mixed for 24 hrs to ensure complete mixing. This solution concentration resulted in solution cast membranes with the same amount of Ti_4O_7 as the E/E membranes. This solution was then cast onto 5 cm x 5 cm pieces of both the ELAT 1 and ELAT 2 GDLs. The solution cast membranes were allowed to dry

in a fume hood for 24 hrs, and then were annealed at 200 ºC for 2 hrs. The resulting filtration membranes consisted of GDL coated with a layer of solution cast PSU/Ti_4O_7. These will be referred to as solution cast membranes. Table 4.1 summarizes all of the membranes fabricated in this study with an abbreviated sample name for each, which will be used throughout the manuscript from this point forward.

Table 4.1 Summary of Membranes Fabricated.

Sample Name	Membrane
ELAT 1	Bare ELAT 1 (ELAT LT 1400 W)
E/E-ELAT 1	E/E PSU/ Ti_4O_7 on ELAT 1
E/E-ELAT 1-A	E/E PSU/ Ti_4O_7 on ELAT 1 – post-annealed at 200 °C for 2 hrs
SC-ELAT 1	Solution Cast PSU/ Ti_4O_7 on ELAT 1
SC-ELAT 1-A	Solution Cast PSU/ Ti_4O_7 on ELAT 1 – post-annealed at 200 °C for 2 hrs
ELAT 2	Bare ELAT 2 (ELAT H)
E/E-ELAT 2	E/E PSU/ Ti_4O_7 on ELAT 2
E/E-ELAT 2-A	E/E PSU/ Ti_4O_7 on ELAT 2 – post-annealed at 200 °C for 2 hrs
E/E-ELAT 2-A-2*	E/E PSU/ Ti_4O_7 on ELAT 2 – post-annealed at 200 °C for 2 hrs
SC-ELAT 2	Solution Cast PSU/ Ti_4O_7 on ELAT 1
SC-ELAT 2-A	Solution Cast PSU/ Ti_4O_7 on ELAT 1 – post-annealed at 200 °C for 2 hrs

***** E/E 2 day process time; all other E/E membranes 6 hrs process time

4.2.5 Membrane Characterization

Scanning electron microscopy (SEM; FEI Quanta 600 FE-SEM) was used for morphological characterization of the E/E and solution cast membranes before and after they were annealed. Samples were sputter coated (Cressington 208 HR) with platinum at 40 mV to achieve a 6 nm layer thickness before SEM images were collected. SEM

images of the membranes were collected at 10kV and a working distance of 10 mm. Additionally, E/E experiments were conducted over the course of 3 days on bare aluminum foil to create 1.17 g of free standing E/E membrane for Hg intrusion porosimetry analysis. Hg porosimetry analysis was also performed for ELAT 2, E/E ELAT 2-A, and E/E-ELAT 2-A-2. Hg intrusion porosimetry analysis was performed by Micromeritic Analytical Services (Norcross, GA).

The conductivities of each of the E/E membranes and solution cast membranes (control), and bare GDLs (control) were measured with electrical impedance spectroscopy (EIS, Solartron, 1260 impedance analyzer, 1287 electrochemical interface, Z Plot software). The in-plane conductivities were measured using a cell with four parallel electrodes. An alternating current was applied to the two outer electrodes while the resistance, R, was measured between the two inner electrodes. Conductivities of each membrane were measured over a frequency range of 0.1 Hz to 10^6 Hz with amplitude of 1 mV in the sinusoidal perturbation. The real impedance or resistance was determined from the high x-intercept of a semi-circle regression of the Nyquist plot data. The conductivity was calculated using the following equation:

$$\sigma = \frac{L}{AR} \tag{4.2}$$

where σ is the conductivity, L is the length between the two inner electrodes, R is the resistance, and A is the cross-sectional area of the membrane ($A = wl$, where w is the width of the membrane and l is the thickness of the membrane). The conductivity of each membrane and GDL (ELAT 1 and ELAT 2) was measured six times and the conductivity and error reported is an average and standard deviation of these values.

4.2.6 Electrochemical Characterization

The electrochemical characterization consisted of cyclic voltammetry (CV) and EIS and was carried out in a single compartment three-electrode glass cell using a potentiostat (Interface 1000, Gamry). The ELAT sample was used as the working electrode and immersed in 100 mM $NaClO_4$ supporting electrolyte. Electrical contact was made using copper tape (Fisher). A platinum wire (Alfa Aesar, Ward Hill, MA) was used as counter electrode and a saturated Ag/AgCl electrode (Pine Instrument, PA) was used as a reference electrode. The reference electrode was placed 1 mm away from the ELAT surface in order to reduce solution resistance and all potentials were corrected for solution resistance (measured by EIS) and are reported against the standard hydrogen electrode (SHE). Cyclic voltammetry was conducted in both the supporting electrolyte and in supporting electrolyte containing both 5 mM $K_3Fe(CN)_6$ and 5 mM $K_4Fe(CN)_6$ at a scan rate of 50 $mV \cdot s^{-1}$.

The measurement of the double layer capacitance (C_{dl}) of select ELAT samples was made within the potential region between hydrogen and oxygen evolution reactions (0.2 to 0.6 vs SHE), and at the scan rates of 2, 4, 8 and 10 mV s^{-1} in 100 mM $NaClO_4$ supporting electrolyte. In the C_{dl} measurement, an ELAT sample with a geometric surface area of 10 cm^2 was used as the working electrode, titanium mesh as counter electrode, and saturated Ag/AgCl as reference electrode. The capacitive current increases linearly with increasing scan rates so that the capacitance of each ELAT sample can be extracted from the slope of the charging current ($i_{charging}$) versus scan rate (ν) as given in equation (4.3).

$$C_{dl} = \frac{i_{charging}}{\nu} \quad (4.3)$$

EIS experiments were conducted at the open circuit potential (OCP) in a quiescent solution containing 5 mM $K_3Fe(CN)_6$ and 5 mM $K_4Fe(CN)_6$ with an amplitude of 10 mV in the sinusoid perturbation and over a frequency range of 10 mHz to 30 kHz. The validity of the EIS data was examined by Kramers-Kronig relations. An equivalent circuit model consisting of a Randles circuit with Warburg impedance was fit to EIS data, and details of the model are discussed in the Results and Discussion Section. Fitting of the Randles circuit and examination of the Kramers-Kronig relation to EIS data were performed in Gamry Echem Analyst software (version 6.23). The simplex algorithm was used to minimize the sum of squared errors between experimental and simulated data. The fitting results are reported along with error estimates at 95% confidence intervals assuming a Chi-squared distribution.

4.2.7 Membrane Filtration Experiments

The cross-flow membrane filtration experimental setup is shown in Figure 4.2a. The feed solution consisted of 100 mM K_2HPO_4 as background electrolyte (pH = 4.5) and 1 mM phenol as target reactant. The background electrolyte concentration was chosen to mimic the ionic strength of industrial wastewater streams and reverse osmosis concentrates.[141-143] Phenol was chosen because is reacts *via* both direct oxidation and $OH^{\bullet}$ oxidation ($k_{phenol,OH^{\bullet}}$ = 6.6 x 10^9 M^{-1} s^{-1}).[144] A total volume of 300 mL feed solution was continuously stirred in the feed tank and was pumped past the membrane at a

constant cross-flow rate (Q_{cross} = 25.8 $L \cdot h^{-1}$), using a bench analog drive gear pump (Cole Parmer). Two different flow configurations were tested: 1) cross-flow mode, where the REMs were placed on a stainless steel current collector and thus prevented liquid flow through the REM pores, and 2) filtration mode, where the REMs were placed on a 0.2 μm pore size polysulfone membrane support and liquid flow permeated through the membrane at a constant flux of Q_{perm} = 6.1 L h^{-1}, which corresponds to a normalized membrane flux of J = 6100 L m^{-2} h^{-1} (1.7 x 10^{-3} m s^{-1}). For both flow configurations, Q_{cross} = 25.8 L h^{-1}, the transmembrane pressure was ~14 kPa, and solutions were 100% recycled to the feed reservoir in order to characterize reaction kinetics. Constant current was supplied to the flow cell by a potentiostat with REM as anode and boron-doped diamond (BDD) plate as cathode. The electrode setup is shown in Figure 4.2b, and the flow cell assembly is shown in Figure 4.2c. The anode and cathode were 6 mm apart. The membrane was mounted between two gaskets with an exposed surface area of 10 cm^2 at the center. The electrical contact between membrane and the potentiostat was made using copper tape.

Prior to each experiment, a membrane was mounted into the flow cell and 2 L deionized water was pumped through the system in a non-recycle mode. During 3 hrs of electrolysis, samples were taken from the feed tank every 20 min, filtered through a 0.45 μm PVDF filters and analyzed in HPLC (LC-20AD Shimadzu). HPLC analysis employed a SPD-M30A variable wavelength UV-Visible detector set at 254 nm and a reverse-phase C18 column (Phenomenex, 4.6 × 250 mm, 5 μm). Methanol:water (50:50, v/v) was used as mobile phase at the total flow rate of 1 $mL \cdot min^{-1}$. The injection volume

was programmed at 5 µL. Analysis was performed in duplicate and evaluated using LabSolutions Lite Version 5.63 software. After each experiment, solutions were pumped through the system in the following sequence: 2 L deionized water (non-recycle), 200 mL 100% ethanol (recycle, 15 min) and 2 L deionized water (non-recycle) to remove adsorbed contaminants. All experiments were performed in duplicate, *i.e.*, experiments were performed on multiple samples of each membrane.

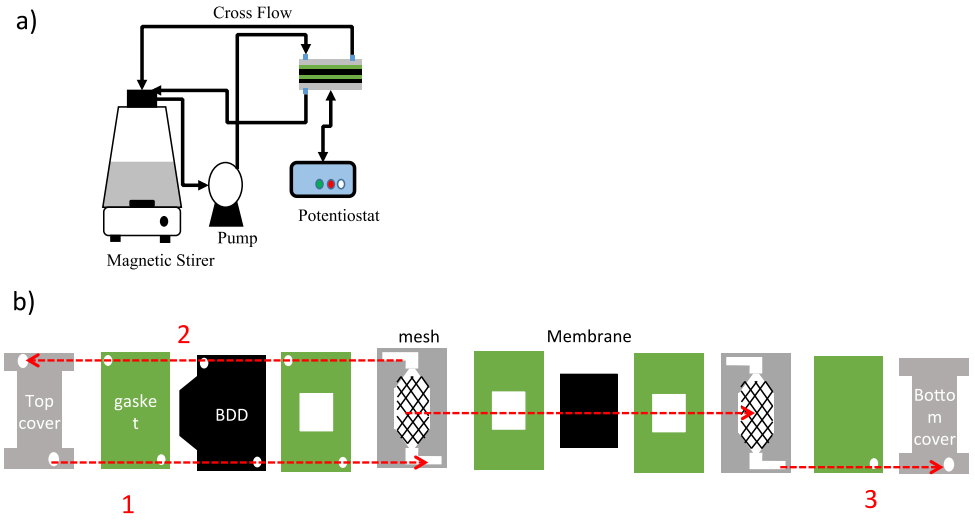

Figure 4.2 (a) Schematic of the membrane filtration setup, (b) components of the flow cell in exploded view. Line 1, 2, and 3 represent feed, retentate, and permeate streams, respectively.

4.3 Results and Discussion

4.3.1 Ti_4O_7 Powder Structure and Morphological Characterization

To fabricate E/E membranes with Ti_4O_7 particles, Ti_4O_7 powder was first synthesized by reducing TiO_2 nanopowder in hydrogen at 950 °C for 4 hrs. After reduction in H_2, the

resulting powder transitioned from a white color to a dark blue/black color. The Ti_4O_7 Magnéli phase present in the reduced TiO_2 nanopowder was confirmed by XRD. Figure 4.3 shows an XRD pattern of Ti_4O_7 powder used for creating E/E and solution cast membranes. The main peaks of interest for characterizing the Ti_4O_7 Magnéli phase occur at 20.7 °, 29.6 °, 31.7 °, and 34.1 °.[110, 145] All of these peaks are present in the XRD pattern shown in Figure 4.3, confirming the presence of the Ti_4O_7 Magnéli phase in the reduced powder, and subsequently successful synthesis of Ti_4O_7 powder for E/E and solution cast membrane fabrication.

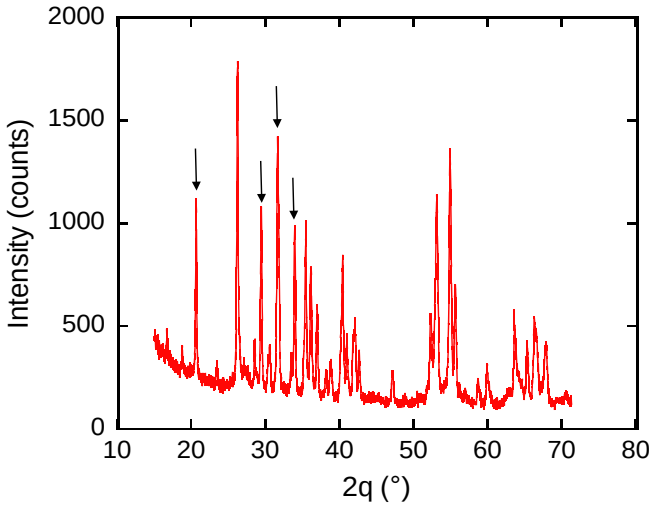

Figure 4.3. XRD pattern of synthesized Ti_4O_7 powder. Characteristic Ti_4O_7 peaks indicated by arrows.

Since the reduction of TiO_2 powder typically produces a sample with at least two or more Magnéli phases, the XRD pattern shown in Figure 4.3 can be used to quantitatively determine the percentage of Ti_4O_7 in the reduced powder. Reduced TiO_2 powder

contains more than one phase because as the reduction of TiO_2 powder proceeds, the powder undergoes successive reduction into several different Magnéli phases, and eventually Ti_4O_7 powder is produced. The other phase most commonly present in these samples is the Ti_5O_9 Magnéli phase. Goldschmidt and Watanabe determined the molecular fraction, *N*, of Ti_4O_7 in a sample by calculating the integrated intensity ratio of the corresponding peak of the Ti_4O_7 and Ti_5O_9 Magnéli phases for a specific plane.[145] The integrated intensity ratios were calculated for the 101 and 121 planes. The corresponding peaks for the 101 and 121 phases in Ti_4O_7 were 20.7 ° and 29.6 °, respectively, and for Ti_5O_9 were 21.9 ° and 29.1 °, respectively.[145] The integrated intensity ratio of each characteristic peak for a specific plane for both the Ti_4O_7 and Ti_5O_9 Magnéli phases can be represented as follows:[145]

$$\frac{N_{59}}{N_{47}} = \frac{P'_{59}\upsilon_{59}F_{47}^2 LP(\theta_{47})}{P'_{47}\upsilon_{47}F_{59}^2 LP(\theta_{59})} \tag{4.4}$$

where N_{59} and N_{47} are the molecular fractions of Ti_5O_9 and Ti_4O_7, respectively, P'_{59} and P'_{47} are the integrated intensities of the corresponding peaks for one of the phases present in Ti_5O_9 and Ti_4O_7, respectively, ν_{59} and ν_{47} are the unit-cell volumes for Ti_5O_9 and Ti_4O_7, respectively, F^2_{59} and F^2_{47} are the triclinic structure factors for Ti_5O_9 and Ti_4O_7, respectively, and LP is the Lorentz-polarization factor. The expression for the Lorentz-polarization factor can be represented as follows:[145]

$$LP(\theta) = \frac{1+\cos^2(2\theta)}{\sin(2\theta)\sin(\theta)} \tag{4.5}$$

where 2θ is the angle for the corresponding peak for the plane of interest. Values for ν_{59}, ν_{47}, F^2_{59}, and F^2_{47} were determined based on work done by LePage and Strobel;[146] ν_{59} and ν_{47} were 590 Å and 465 Å, respectively, and F^2_{59} were 5240 and 12070 and F^2_{47} were 3240 and 6990 for the 101 and 121 phases, respectively.[147] Using Equations 4.4 and 4.5, the molecular fractions of Ti_4O_7 and Ti_5O_9 were calculated in each sample of reduced TiO_2 powder produced. For the XRD pattern shown in Figure 4.3, the molecular fraction of Ti_4O_7 calculated in the powder was 94.3 % ± 4.6 %. On average, the Ti_4O_7 was 90.6 % ± 4.6 % for all the samples produced in this study.

The morphology of the Ti_4O_7 powder produced in this study was examined using SEM, and the images are shown in Figure 4.4. Figure 4.4a shows an SEM image of the Ti_4O_7 powder used to create the E/E and solution cast membranes. Figure 4.4b shows a magnified view of Figure 4.4a. Figure 4.4 shows that the Ti_4O_7 powder is highly aggregated, and the particles are neither spherical nor oblong shaped. Furthermore, unlike their precursor, TiO_2 nanopowder, Figure 4.4b shows that the Ti_4O_7 powder particle size is much larger due to the sintering process.

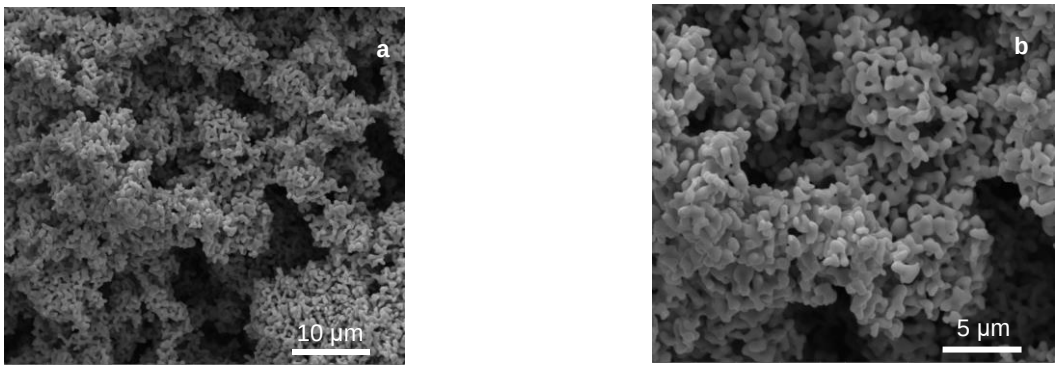

Figure 4.4 SEM images of Ti_4O_7 powder at (a) 5k X and (b) 10k X magnification.

4.3.2 E/E Membrane Characterization

Morphological characterization of the E/E membranes was also performed using SEM. Figures 4.5a and b show SEM images of E/E membranes of electrospun PSU and electrosprayed Ti_4O_7 on ELAT 1 before the membranes were annealed (E/E-ELAT 1). Figure 4.5a shows PSU nanofibers and Ti_4O_7 particles. Figure 4.5b shows a magnified view of Figure 4.5a, where both Ti_4O_7 particles and PSU nanofibers can be seen more clearly. Additionally, the highly porous structure of the E/E-ELAT 1 membranes can be observed in Figure 4.5. Also, larger agglomerates or particles of PSU were observed (see lower left hand corner of SEM image in Figure 4.5a. During electrospinning, a polymer solution is ejected out of an electrified syringe needle resulting in Taylor cone at the tip and an elongated liquid jet that forms into nanofibers.[148] Occasionally during the electrospinning process, the polymer solution can clog at the needle tip due to the high viscosity of the solution resulting in a buildup of pressure. The needle was cleaned periodically during the electrospinning process to minimize clogging, but would quickly exit the needle as a spray and not a fiber directly after cleaning leading to a combination of PSU fibers and larger particles like those shown in Figures 4.5a and b. The 9.1 wt% PSU/DCM solution for electrospinning resulted in the highest number of PSU nanofibers. A solution concentration greater than 9.1 wt% PSU/DCM would lead to a membrane largely composed of PSU microfibers and large electrosprayed PSU particles, while a solution less than 9.1 wt% PSU/DCM would result in few PSU nanofibers and many electrosprayed PSU particles. Lowering the polymer solution concentration or

viscosity results in no Taylor cone formation and thus primarily electrospraying instead of electrospinning.[148]

Figures 4.5c and d show SEM images of E/E membranes of electrospun PSU and electrosprayed Ti_4O_7 on ELAT 1 after the membranes were annealed at 200 °C (E/E-ELAT 1-A). Larger PSU fibers are observed along with a fusing of Ti_4O_7 particles to the polymer and also to the ELAT 1. Figure 4.5d is a magnified view of the E/E-ELAT 1-A membrane shown in Figure 4.5c. The images show that the highly porous structure of the E/E-ELAT 1-A membranes persists even after annealing. Therefore, annealing E/E-ELAT 1-A membranes results in highly porous, durable membranes with enhanced adhesion between materials that can subsequently be used for water filtration experiments.

Figures 4.5e and f show SEM images of the bare ELAT 1 used as the substrate for the E/E-ELAT 1 and E/E-ELAT 1-A membranes shown in Figures 4.5a-d. Figure 4.5e shows that the PTFE-treated microporous carbon layer on top of the woven carbon cloth membrane has a fairly uniform morphology across the substrate with visible cracks. Figure 4.5f shows a magnified view of Figure 4.5e, showing the morphology of the coating in more detail, highlighting the cracks in the coating, which are on the order of ~10 μm.

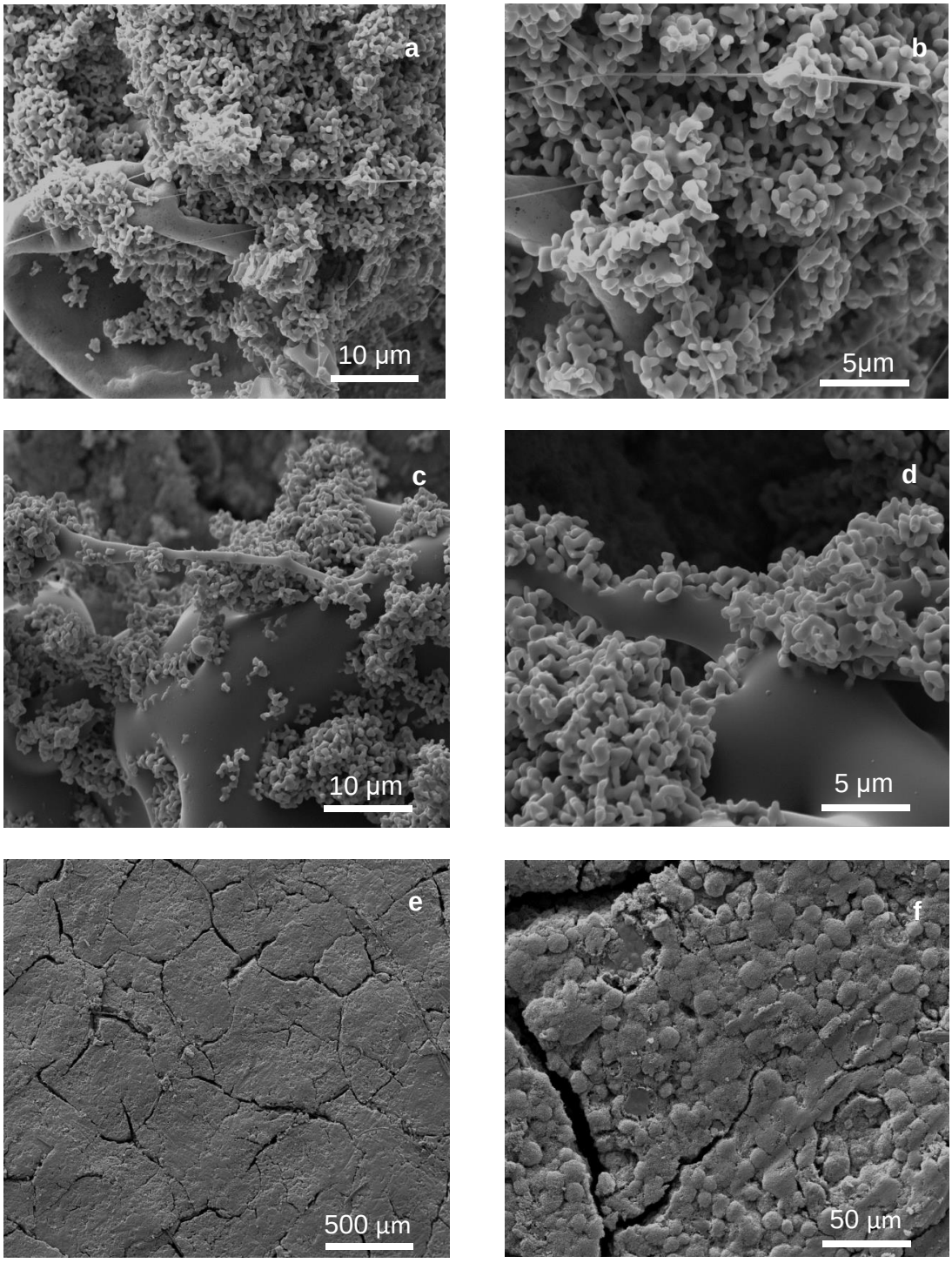

Figure 4.5 SEM images of E/E-ELAT 1 at (a) 5k X and (b) 10k X magnification and E/E-ELAT 1-A at (c) 5k X and (d) 10k X magnification and ELAT1 at (e) 100 X and (f) 1k X magnification.

Figures 4.6a and b show SEM images of E/E membranes of electrospun PSU and electrosprayed Ti_4O_7 on ELAT 2 before the membranes were annealed (E/E-ELAT 2). Figure 4.6b is a magnified view of the E/E-ELAT 2 membrane shown in Figure 4.6a, where both Ti_4O_7 particles and PSU nanofibers can be seen more clearly and the highly porous structure of the E/E PSU/Ti_4O_7 membranes can be observed. Similar to Figure 4.5, larger agglomerates, or particles of PSU were observed (see upper right hand corner of Figure 4.6a). Additionally, both Figures 4.5a and b and Figures 4.6a and b display a network of micron-sized Ti_4O_7 particles and PSU nanofibers, demonstrating that regardless of the substrate, fabrication of a nanofiber/particle network occurs.

Figures 4.6c and d show SEM images of E/E membranes of electrospun PSU and electrosprayed Ti_4O_7 on ELAT 2 after the membranes were annealed at 200 °C (E/E-ELAT 2-A). PSU fibers were not observed, but rather Ti_4O_7 particles fused to large agglomerates (melted fibers) of the polymer and also to the ELAT 2 was observed. Figure 4.6d is a magnified view of Figure 4.6c, where adhesion of the PSU and the Ti_4O_7 particles to the ELAT 2 large carbon fibers can be clearly seen. Similar to Figure 4.5, the images show that the E/E-ELAT 2-A membranes remain highly porous even after annealing, resulting in durable, highly porous membranes with enhanced adhesion between materials that can subsequently be used for water filtration experiments.

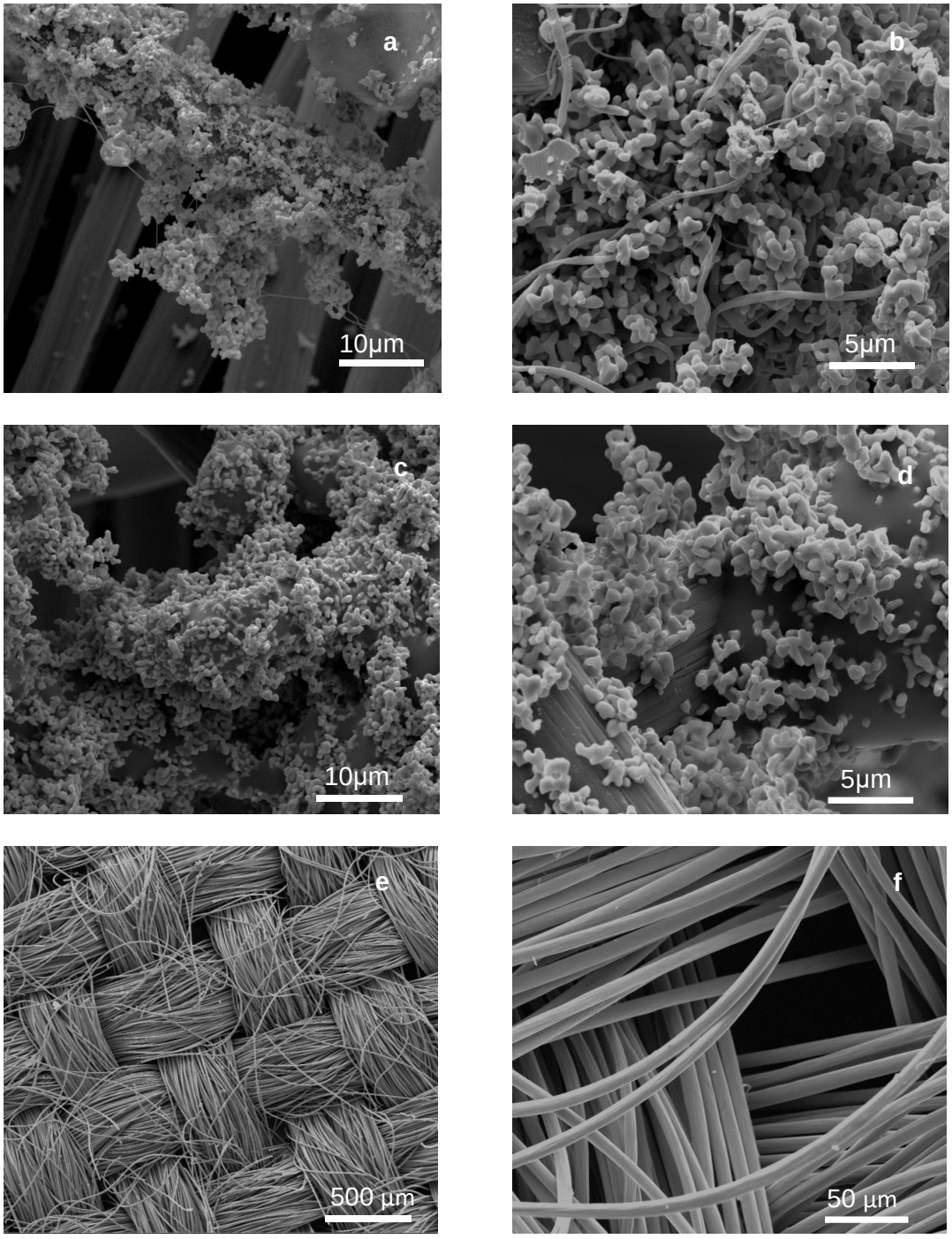

Figure 4.6 SEM images of E/E-ELAT 2 at (a) 5k X and (b) 10k X magnification and E/E-ELAT 2-A at (c) 5k X and (d) 10k X magnification and ELAT 2 at (e) 100 X and (f) 1k X magnification.

Figures 4.6e and f show SEM images of the bare ELAT 2 used as the substrate to create the E/E-ELAT 2 and E/E-ELAT 2-A membranes shown in Figures 4.6a-d. Figure 4.6e show that the ELAT 2 is comprised of a neatly woven carbon cloth membrane. Figure 4.6f shows a magnified view of Figure 4.6e clearly showing the carbon fibers and pores, which are on the order of ~50 μm. The difference in pore size between ELAT 1 and ELAT 2 is due to the PTFE-treated microporous carbon layer present in ELAT 1. ELAT 2 is a bare woven carbon cloth membrane with a porosity of 80%. The PTFE-treated microporous carbon layer on ELAT 1 shown in Figures 4.5e and f completely covered the woven carbon cloth membrane reducing the porosity to 63%.

4.3.3 Solution Cast Membrane Characterization

Figures 4.7a and b show SEM images of solution cast membranes of PSU/Ti_4O_7 on ELAT 1 before the membranes were annealed (SC-ELAT 1). Figure 4.7a shows a PSU/Ti_4O_7 film covering the PTFE-treated microporous carbon layer on the ELAT 1. Since there is only a PSU/Ti_4O_7 film covering the ELAT 1, the morphology in Figure 4.7a is similar to that of Figure 4.5e, showing the uniform morphology of the substrate with the PSU/Ti_4O_7 film sealing the cracks. Figure 4.7b is a magnified view of the solution cast membrane shown in Figure 6a showing the morphology of the film coating the ELAT 1 in detail, highlighting the Ti_4O_7 particles embedded in the PSU/Ti_4O_7 film. Figures 4.7c and d shows SEM images of solution cast membranes of PSU/Ti_4O_7 on ELAT 1 after the membranes were annealed at 200 °C (SC-ELAT 1-A). Figure 4.7d is a magnified view of the solution cast membrane shown in Figure 4.7c. Since a PSU/Ti_4O_7

film was solution cast onto the ELAT 1, there is not a significant change in the PSU morphology shown in Figures 4.7c and d. The main difference is that Ti_4O_7 particles can be seen more clearly in Figures 4.7c and d than in Figures 4.7a and b. Unlike Figures 4.5 and 4.6, Figure 4.7 shows that the solution cast membranes do not have a highly porous structure because the PSU/Ti_4O_7 film covers the PTFE-treated microporous carbon layer on the ELAT 1 completely and creates a non-porous dense membrane film.

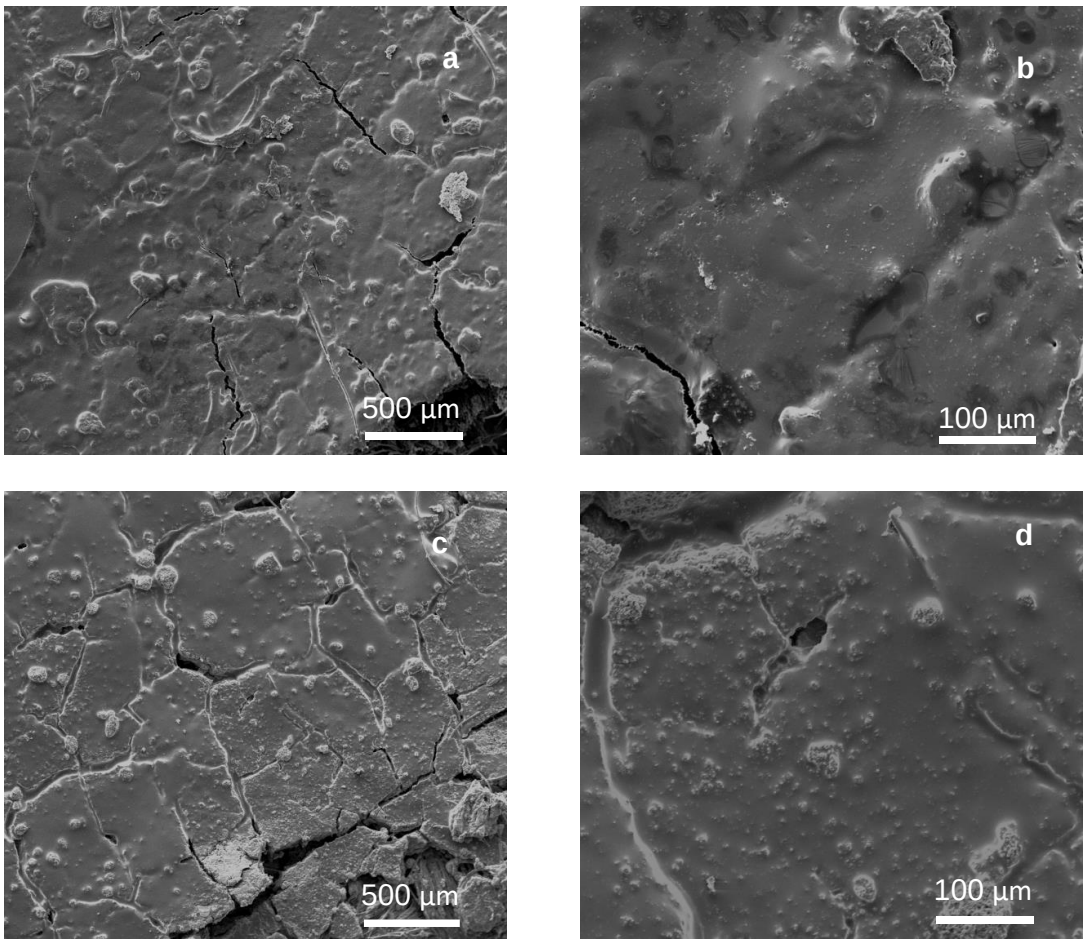

Figures 4.7 SEM images of SC-ELAT1 at (a) 100 X and (b) 500 X magnification and SC-ELAT 1-A at (c) 100 X and (d) 500 X magnification.

Figures 4.8a and b show SEM images of solution cast membranes of PSU/Ti_4O_7 on ELAT 2 before the membranes were annealed (SC-ELAT 2). Figure 4.8 shows a PSU/Ti_4O_7 film covering all the carbon fibers of the ELAT 2. Similar to Figure 4.7, the morphology in Figure 4.8b is a magnified view of the solution cast membrane shown in Figure 4.8a showing the morphology of the PSU/Ti_4O_7 film coating the ELAT 2 in detail, highlighting the Ti_4O_7 particles embedded in the PSU/Ti_4O_7 film. Figures 4.8c and d show SEM images of solution cast membranes of PSU/Ti_4O_7 on ELAT 2 after the membranes were annealed at 200 °C (SC-ELAT 2-A). Figure 4.8d is a magnified view of the solution cast membrane shown in Figure 4.8c. Since a PSU/Ti_4O_7 film was solution cast onto the ELAT 2, there is not a significant change in the PSU morphology shown in Figures 4.8c and d. The main difference is that Ti_4O_7 particles can be seen more clearly in Figures 4.8c and d than in Figures 4.8a and b. Additionally, the annealed PSU film in Figure 4.8c shows gaps between the woven fibers that were not present in Figure 4.8a before the solution cast membranes were annealed. However, these appear to be a surface effect and not a pore that extends transverse through the membrane. Unlike Figures 4.5 and 4.6, but similar to Figure 4.7, Figure 4.8 shows that the solution cast membranes do not have a highly porous structure, but rather a non-porous dense membrane that covers the ELAT 2 substrate completely. The membranes in Figures 4.7 and 4.8 were fabricated merely as control membranes for comparison purposes and not with the expectation of achieving high reactivity during filtration experiments.

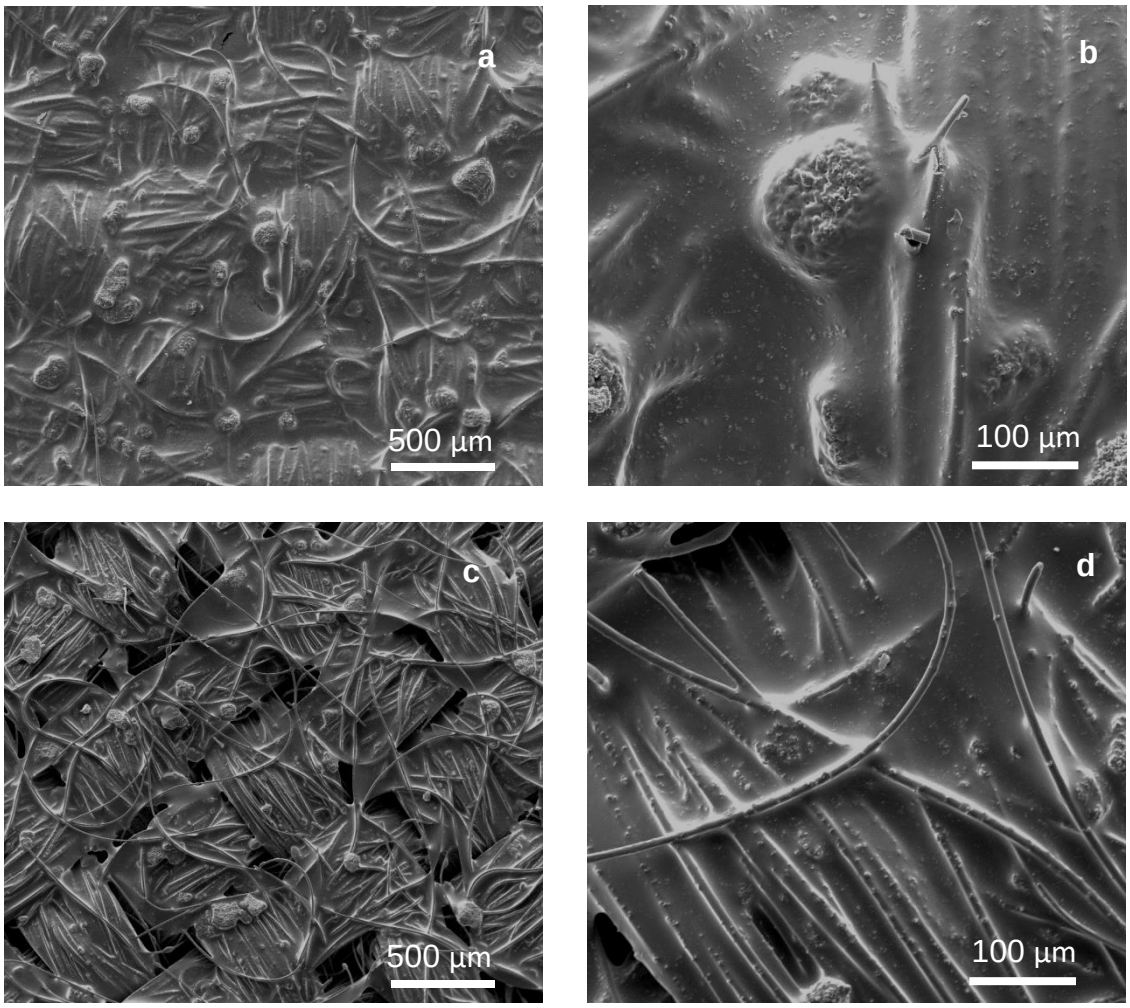

Figures 4.8 SEM images of SC-ELAT 2 at (a) 100 X and (b) 500 X magnification SC-ELAT 2-A and at (c) 100 X and (d) 500 X magnification.

4.3.4 Electrical Conductivity

Table 4.2 shows the electrical conductivity of the membranes. The solution cast membranes and bare ELAT 1 and ELAT 2 were tested as controls for the E/E membranes. The results in Table 4.2 show that the conductivity of ELAT 1 and ELAT 2 are similar in magnitude, demonstrating that the substrates used for creating the E/E and solution cast membranes were conductive. Additionally, the conductivities of the E/E

and solution cast membranes are similar to those of bare ELAT 1 and ELAT 2, indicating that the conductivities of the E/E and solution cast membranes are maintained. These results demonstrate that the E/E PSU/Ti_4O_7 membranes are not only highly porous and durable, but are also conductive, which is an important characteristic for REMs. Overall, these REMs are not resistant to electrical current and can subsequently be used for electrochemical water filtration experiments.

Table 4.2 Electrical Conductivity of Membranes.

Sample Name	Conductivity (S/cm)
ELAT 1	47.25 ± 0.05
E/E-ELAT 1-A	45.67 ± 0.67
E/E-ELAT 1-A	41.35 ± 0.02
SC-ELAT 1-A	38.38 ± 0.13
ELAT 2	46.95 ± 0.07
E/E-ELAT 2-A	50.71 ± 0.07
E/E-ELAT 2-A	46.12 ± 0.05
E/E-ELAT 2-A-2	42.35 ± 0.54
SC-ELAT 2-A	42.18 ± 0.07

4.3.5 Hg Porosimetry

The pore structure of the free-standing E/E membrane, E/E ELAT 2-A, E/E ELAT 2-A-2 and ELAT 2 were characterized using Hg intrusion porosimetry analysis. Figure 4.9 shows the cumulative pore area and the log differential intrusion as a function of the pore diameter for each membrane analyzed. Figure 4.9b shows that the majority of the pore volume of the free-standing E/E membrane consists of 16-45 μm sized pores.

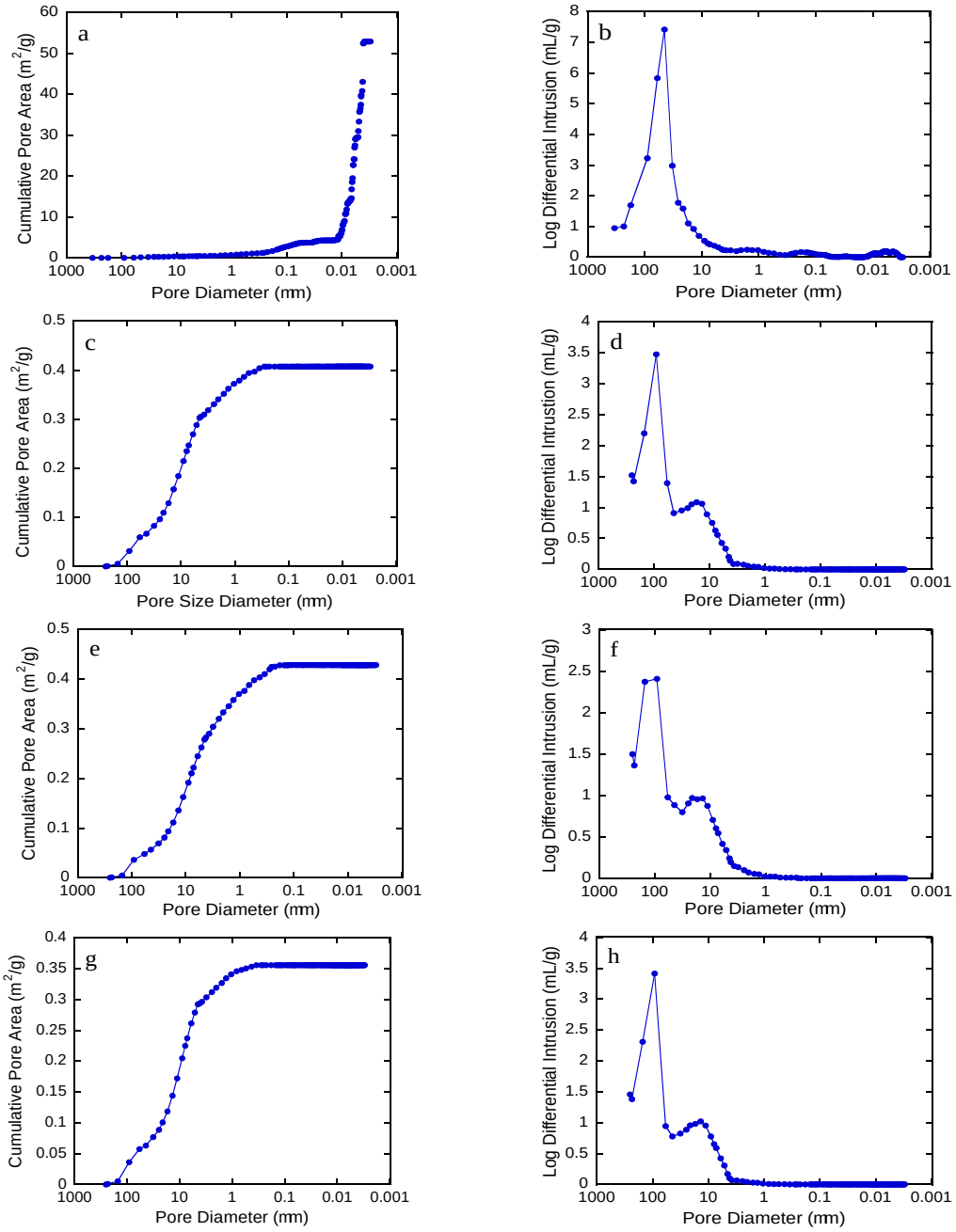

Figure 4.9 Results of Hg intrusion porosimetry analysis for (a,b) free-standing E/E membrane, (c,d) E/E-ELAT 2-A, (e,f) E/E ELAT 2-A-2, (g,h) ELAT 2. a,c,e,g refer to cumulative pore area and b,d,f,h refer to log differential intrusion pore volume (solid lines represent piece-wise linear interpolation).

Unlike the free-standing E/E membrane, the composite membranes and bare ELAT 2 alone show different patterns for the cumulative pore area and the log differential intrusion. This is due to the ELAT 2 substrate (Figures 4.9g and 4.9h), which has a vastly different pore structure than the E/E PSU/Ti4O7 adhered to it. Figures 4.9d, 4.9f, and 4.9h show significant peaks at approximately 15 μm and 100 μm. The 15 μm pore sizes are most likely due to the pores between the fibers of the bare ELAT 2 membrane, and the 100 μm pore sizes are most likely due to the pores between the bundles of fibers of the ELAT 2 membrane shown in Figures 4.6e and 4.6f.

4.3.6 Electrochemical Characterization

The CV scans were used to characterize the potential window of water stability and the electrochemical response to the $Fe(CN)_6^{4-/3-}$ redox couple. This redox couple was chosen because it undergoes a facile outer sphere electron transfer reaction and is used as a probe to assess the effect of Ti_4O_7 on the reaction kinetics towards the $Fe(CN)_6^{4-/3-}$ redox couple. Results of CV scans are shown in Figure 4.10.

Results in Figure 4.10a indicate that the ELAT 1 substrate had low activity for water oxidation and reduction reactions over the investigated potential range. By contrast, the E/E-ELAT 1-A sample showed an enhanced reactivity for both water oxidation and water reduction relative to ELAT 1, which was also much higher than for the solution cast REM (SC-ELAT 1-A). These results are attributed to the coating of the Ti_4O_7 particles by the PSU polymer, and the lower porosity created by the solution cast process

relative to the E/E fabrication technique, which is evident from SEM images (Figures 4.5 and 4.7).

The CV scans for ELAT 2, E/E-ELAT 2-A, E/E-ELAT 2-A-2, and SC-ELAT 2-A are shown in Figure 4.10b. Results for the E/E-ELAT 2-A membrane showed that the addition of the Ti_4O_7 particles caused a slightly higher overpotential for water oxidation and lower overpotential for water reduction, which is characteristic of Ti_4O_7.[149] However, the results for both the E/E-ELAT 2-A-2 and SC-ELAT 2-A membranes indicate that water oxidation and reduction reactions were less active than on E/E-ELAT 2-A. These results are again attributed to the coating of the Ti_4O_7 particles by the PSU polymer, and the lower porosity (and thus surface area) created by the solution cast technique relative to the E/E fabrication technique, which is evident from SEM images (Figures 4.6 and 4.8). Additionally, it should be noted that the current density for water oxidation and reduction was much greater for the ELAT 2 materials (Figure 4.10b) relative to the ELAT 1 materials (Figure 4.10a), this result is attributed to the higher porosity of the ELAT 2 materials and the higher activity of ELAT 2 relative to ELAT 1 for water oxidation and reduction reactions, the latter is attributed to the hydrophobic PTFE-treated microporous carbon coating that is present on ELAT 1.

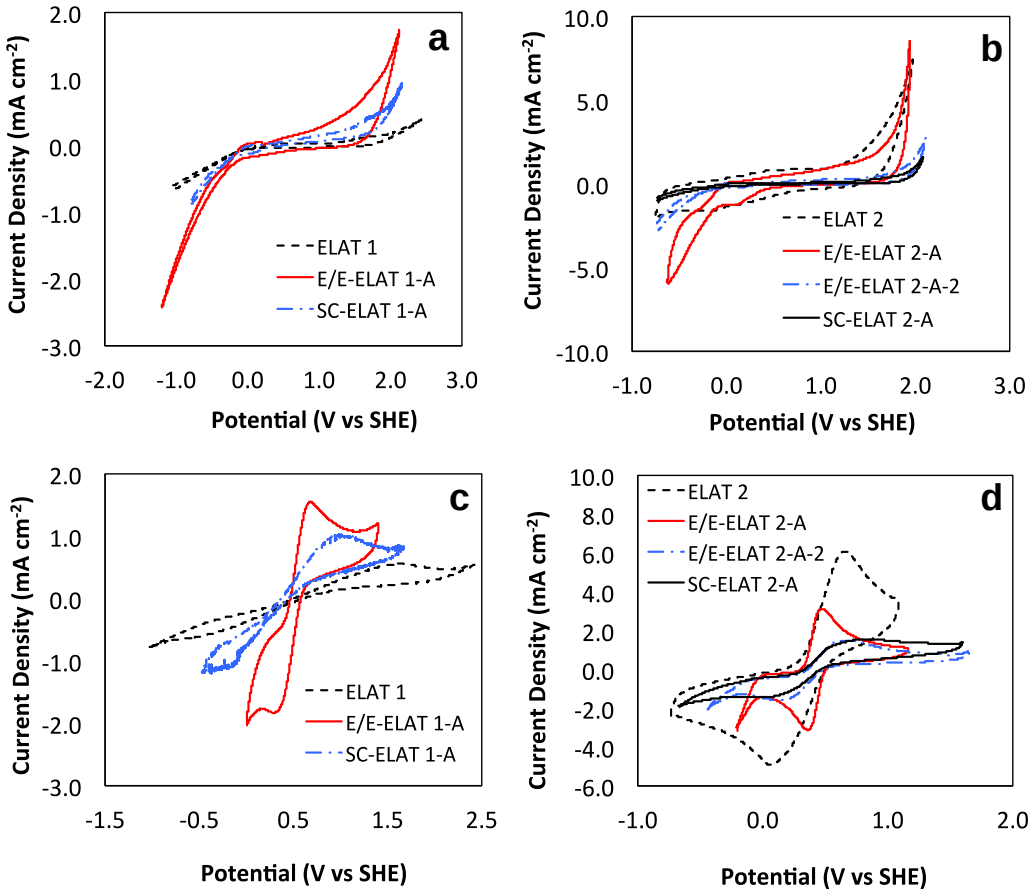

Figure 4.10 CV scans in 100 mM $NaClO_4$ supporting electrolyte for (a) ELAT 1 REMs and (b) ELAT 2 REMs. CV scans in 100 mM $NaClO_4$ supporting electrolyte and 5 mM $Fe(CN)_6^{4-/3-}$ redox couple for (c) ELAT 1 REMs and (d) ELAT 2 REMs. Scan rate: 50 mV s^{-1}.

Investigation of the $Fe(CN)_6^{4-/3-}$ redox couple on the REMs is shown in Figure 4.10c and 4.10d and data summarizing the analysis of these CV curves is included in Table 4.3. For all CV scans with the $Fe(CN)_6^{4-/3-}$ redox couple, the anodic peak current (I_{pa}) to cathodic peak current (I_{pc}) ratio was close to unity (I_{pa}/I_{pc} = 0.89 - 1.24), indicating that neither homogeneous reactions nor adsorption were occurring during these scans.[150] The CV scans with the $Fe(CN)_6^{4-/3-}$ redox couple were used to determine changes to the

reactive surface area and reaction kinetics of the $Fe(CN)_6^{4-/3-}$ redox couple. The reactive surface area was assessed by I_{pa} and reaction kinetics was qualitatively assessed by the anodic and cathodic peak separation (ΔE_p) (Table 4.3). The ELAT 1 substrate showed irreversible kinetics for the $Fe(CN)_6^{4-/3-}$ redox couple (Figure 4.10c), which was attributed to the hydrophobic PTFE-treated microporous carbon coating. The addition of the Ti_4O_7 particles by the E/E fabrication technique (E/E-ELAT 1-A) increased I_{pa} and decreased ΔE_p relative to ELAT, indicating an increase in the reaction surface area and enhancement of the reaction kinetics (Figure 4.10c and Table 4.3). SC-ELAT 1-A showed some enhancement of kinetics (ΔE_p = 1092 mV) and reactive surface area (I_{pa} = 1.03 mA cm^{-2}) compared to the ELAT 1 substrate, but not to the extent of the E/E-ELAT 1-A membrane. The response was more irreversible than the E/E-ELAT 1-A, which was attributed to the coating of the Ti_4O_7 particles by the PSU polymer in the SC-ELAT 1-A membrane (see Figure 4.7).

Table 4.3 Summary of CV Data and Data Analysis for E/E REMs.

Membrane Sample	I_{pa} (mA/cm^2)	I_{pc} (mA/cm^2)	I_{pa}/I_{pc}	ΔE_p (mV)	C_{dl} (F/cm^2)	$C_{dl,f}/C_{dl,ELAT2}$	ρ	k^o_{app} (cm/s)	k^o (cm/s)
ELAT 1	0.554	-0.570	0.97	2000	-	-	-	-	-
E/E-ELAT 1-A	1.55	-1.75	0.89	307	-	-	-	-	-
SC–ELAT 1-A	1.03	-1.04	0.99	1092	-	-	-	-	-
ELAT2	6.09	-4.92	1.24	583	$3.37x10^{-4}$	1.00	17	$3.54x10^{-3}$	$2.10x10^{-4}$
E/E ELAT 2-A	3.13	-2.92	1.07	77	$1.32x10^{-4}$	0.39	6.6	$7.71x10^{-3}$	$1.17x10^{-3}$
E/E ELAT 2-A-2	1.51	-1.65	0.92	454	$3.56x10^{-5}$	0.11	1.8	$3.67x10^{-4}$	$2.07x10^{-4}$
SC–ELAT 2-A	1.56	-1.45	1.08	782	$1.03x10^{-4}$	0.31	5.2	$3.93x10^{-4}$	$7.64x10^{-5}$

a = Determined by EIS measurements
b = Normalized by electroactive surface area determined by C_{dl} measurements (divided by ρ).

CV scans in the presence of 5 mM $Fe(CN)_6^{4-/3-}$ redox couple for ELAT 2 REMs are shown in Figure 4.10d. The uncoated ELAT 2 substrate showed the highest peak current (I_{pa} = 6.09 mA cm^{-2}) and the largest peak separation (ΔE_p = 583 mV) compared to the other ELAT 2 coated materials, except SC-ELAT 2-A (Table 4.3). Upon the addition of Ti_4O_7 to ELAT 2 by the E/E method (E/E-ELAT 2-A), it was observed that both ΔE_p and I_{pa} decreased (Figure 4.10d and Table 4.3). These results are once again attributed to the PSU polymer deposition on the ELAT 2 substrate. The E/E method operated under short deposition times (6 hrs) (E/E-ELAT 2-A) was able to deposit Ti_4O_7 particles with low PSU polymer coverage, that produced membranes with intimate contact between the Ti_4O_7 particles and the ELAT 2 porous matrix. By contrast, both the E/E method operated under extended deposition times (E/E-ELAT 2-A-2) and the solution cast method (SC-ELAT 2-A) produced membranes with excess PSU polymer coating that prevented access of aqueous solutes to the Ti_4O_7 particles and thus inhibited electron transfer rates. The SEM images in Figure 4.8 clearly show the coating of the Ti_4O_7 particles and the ELAT 2 substrate with the PSU polymer.

A more reversible reaction typically results in an increase in I_{pa}. The diminished I_{pa} observed after Ti_4O_7 addition (see Table 4.3) is attributed to reduction of the electroactive surface area during REM synthesis. The E/E-ELAT 2-A-2 membrane, which was subjected to the E/E process for 2 days, showed higher irreversibility than E/E-ELAT 2-A, which was synthesized for a shorter time (6 hrs). This result is attributed to an increase in PSU polymer deposition on the ELAT 2 substrate with E/E deposition time, which resulted in a decrease in the electroactive surface.

The ELAT 2-based REMs showed a higher reactivity for water oxidation and reduction and increased reversibility for the $Fe(CN)_6^{4-/3-}$ redox couple relative to the ELAT 1-based REMs. Therefore, ELAT 2-based REMs were chosen for further electrochemical characterization. The double layer capacitance (C_{dl}) values were measured for the ELAT 2-based REMs and were used to assess the change in electroactive surface area and to determine a roughness factor (ρ) for each of the REMs. Capacitance methods for the determination of electroactive surface area have been applied in prior studies.[151] The C_{dl} is a measure of the electroactive surface area of the materials and was highest for the bare ELAT 2 substrate (C_{dl} = 3.37 x 10^{-4} F cm^{-2}) and decreased after E/E and SC coatings. The ratio of $C_{dl,i}/C_{dl,ELAT-2}$ was 0.39, 0.11, and 0.31 for i = E/E-ELAT 2-A, E/E-ELAT 2-A-2, SC-ELAT 2-A, respectively. The values for $C_{dl,i}/C_{dl,ELAT-2}$ were similar to the $I_{pa,i}/I_{pa,ELAT-2}$ values determined from the CV data shown in Figure 4.10d, which were 0.51, 0.25, and 0.26 for i = E/E-ELAT 2-A, E/E-ELAT 2-A-2, and SC-ELAT 2-A, respectively. These results suggest that the deposition of the PSU/Ti_4O_7 decreased the electroactive surface area of the REMs, and this decrease in electro-active surface area was responsible for the decrease in I_{pa} observed in CV data (Figure 4.10d). The decrease in ΔE_p after the addition of Ti_4O_7 particles indicates that Ti_4O_7 was more active for the $Fe(CN)_6^{4-/3-}$ redox couple, than the bare ELAT 2 support.

The ρ value for each REM was estimated from the C_{dl} measurements by assuming an average double layer capacitance of 20 $\mu F\ cm^{-2}$ for the bare ELAT 2 support.[152-153] The ρ for Ti_4O_7 coated samples was determined by assuming that the $C_{dl,i}/C_{dl,ELAT-2}$ ratio was representative of the change in surface area. This approach may overestimate the actual

ρ values of the REMs, since the Ti_4O_7 particles likely have a slightly higher C_{dl} than the carbon support, but was deemed as a reasonable first order approximation. Results indicate that ELAT 2 had a ρ value of 17, and ρ decreased to 6.6, 1.8, and 5.2 for the E/E-ELAT 2-A, E/E-ELAT 2-A-2, and SC-ELAT 2-A REMs, respectively. The decrease in surface roughness is related to polymer deposition, which is apparent from SEM images. Figure 4.6 shows the deposition of large polymer deposits on the ELAT 2 coating when using the E/E deposition method, and Figure 4.8 shows a uniform coating when using the SC method.

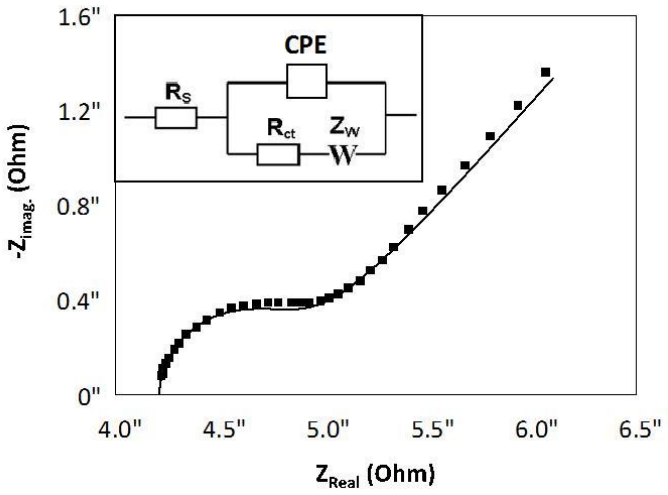

Figure 4.11 Electrochemical impedance spectra for E/E-ELAT 2-A over the frequency 30 kHz – 0.4 Hz in the presence of 5 mM redox couple in 100 mM $NaClO_4$.

EIS measurements were used to estimate the charge transfer resistance (R_{ct}) of the of 5 mM $Fe(CN)_6^{4-/3-}$ redox couple and to estimate a reaction rate constant. Figure 4.11 contains EIS data and an equivalent circuit model fit for the E/E-ELAT 2-A REM. A

summary of all the regressed parameters from the equivalent circuit model fits of all the ELAT 2-based REMs are shown in Table 4.4. The EIS results support the results obtained from the CV data. The apparent standard heterogeneous rate constant (k^{o}_{app}) was determined for the tested redox couple using the measured value of R_{ct} and the following equation:[154]

$$k^{\circ}_{app} = \frac{RT}{R_{ct}ACF^{2}} \tag{4.6}$$

where R is the ideal gas constant, T is temperature, C is the concentration of the redox couple, A is the membrane geometric surface area, and F is Faraday's constant. The standard rate constant (k^{o}) was also estimated by dividing by the roughness factor to normalize by the "real" electroactive surface area. Results are shown in Table 4.3. The comparable k^{o} values show that the difference in CV curves for ELAT 2 and E/E-ELAT 2-A-2 are attributed to surface area changes, and also that the C_{dl} ratio is an accurate approximation of the change in electroactive surface area. The E/E-ELAT 2-A material showed changes to reversible behavior, which increased the surface area normalized rate constant (k^{o}) by a factor of > 5, which is attributed to enhanced kinetics on Ti_4O_7 particles relative to the ELAT 2 support.

Overall the results from CV and EIS analyses indicate that the ELAT 2 substrate was more active for water electrolysis reactions and reaction with the $Fe(CN)_6^{4-/3-}$ redox couple relative to ELAT 1, which was attributed to the hydrophobic PTFE-treated microporous carbon coating on ELAT 1 that was less active for these reactions and also acted to reduce the total surface area (per SEM images). It also was found that the

deposition of the Ti_4O_7 particles by the E/E method for 6 hrs (E/E-ELAT 2-A) produced the best membranes with respect to increased activity for water electrolysis and the $Fe(CN)_6^{4-/3-}$ redox couple. The response was highly correlated to the content of PSU polymer on the REM material, which acted to reduce the electroactive surface area for the E/E-ELAT 2-A-2 and SC-ELAT 2-A membranes.

Table 4.4 Summary of Regressed Parameters from EIS Equivalent Circuit Model. Errors Represent 95% Confidence Intervals for Fitted Parameters.

Sample Name		R_s	R_{ct}	Y_o	a	W
ELAT 2	Value	4.76	1.48	3.13×10^{-2}	0.68	5.25×10^{-1}
	Error	0.07	0.27	1.63×10^{-2}	0.11	3.5×10^{-2}
E/E-ELAT 2-A	Value	4.22	0.68	1.98×10^{-2}	0.92	7.13×10^{-1}
	Error	0.06	0.21	7.92×10^{-3}	0.19	1.31×10^{-1}
E/E-ELAT 2-A-2	Value	2.75	14.23	2.52×10^{-3}	0.79	1.51×10^{-1}
	Error	0.02	0.39	1.64×10^{-4}	0.01	1.96×10^{-2}
SC-ELAT 2-A	Value	6.92	13.3	1.27×10^{-3}	0.71	2.89×10^{-1}
	Error	0.06	0.26	1.32×10^{-4}	0.02	2.77×10^{-2}

4.3.7 Flow-through Experiments

To determine the potential of the synthesized REM materials for water treatment applications, a series of experiments were conducted to assess phenol oxidation. To determine the potential of the E/E REMs for water treatment applications, a series of experiments were conducted to assess phenol oxidation. CV scans were first conducted in batch mode to assess the direct oxidation of phenol (Figure 4.12).

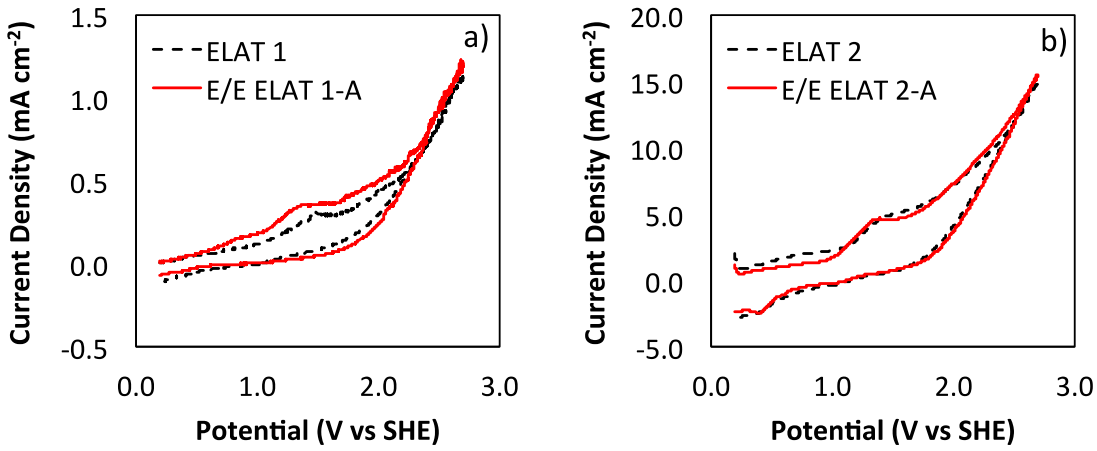

Figure 4.12 CV scans of 5 mM phenol in 100 mM $NaClO_4$ supporting electrolyte for a) ELAT 1 and E/E ELAT 1-A and b) ELAT 2 and E/E ELAT 2-A. Experimental conditions: Working electrode = ELAT (10 cm^2); Counter electrode = Pt wire; Reference electrode = Ag/AgCl; T = 20 °C; Scan rate: 50 mV s^{-1}.

Peaks associated with the direct oxidation of phenol (E ~ 1.3 V) indicate some enhancement for E/E-ELAT 1-A relative to ELAT 1 (Figure 4.12a), and results were similar for both E/E-ELAT 2-A and ELAT 2 (Figure 4.12b). Direct oxidation of phenol was much greater on the ELAT 2 materials compared to the ELAT 1 materials, which is consistent with results shown in Figure 4.10. To assess bulk phenol oxidation by both direct oxidation and reaction with $OH^{\bullet}$, the E/E REMs were tested in the flow-through reactor shown in Figure 4.2. Experiments were conducted in both cross-flow and filtration mode, and for both flow configurations the cross-flow rate was held constant (Q = 25.8 L h^{-1}) and solutions were 100% recycled to the feed reservoir in order to characterize removal kinetics. Results for phenol oxidation experiments at a current density of 1.0 mA cm^{-2} are shown in Figure 4.13a. The kinetics for phenol removal were found to be first-order, and an example of the data and the first-order model fit (k_{obs}) are

provided in Figure 4.13b. Extensive product formation was not characterized, but results from chemical oxygen demand (COD) data indicate only a modest removal of COD (~10-20 %), which indicates that phenol was oxidized to other products and neither substantial polymerization nor mineralization of phenol occurred. When the REMs were operated in filtration mode versus cross-flow mode, the k_{obs} for phenol removal changed by a factor of 1.2, 0.8, and 1.6 for the ELAT 1, E/E-ELAT 1-A, and ELAT 2 REMs, respectively (Figure 4.12a). The lack of a significant change between filtration and cross-flow operation indicates that reaction kinetics were not significantly affected by mass transport and were at or near the kinetic limit. We expected an enhancement in reaction kinetics for E/E ELAT 1, but k_{obs} was similar to ELAT 1. It therefore is possible that the dense ELAT 1 substrate, which contained the PTFE treated microporous carbon layer, created preferential flow paths and the Ti_4O_7 particles were bypassed during filtration. However, when the E/E-ELAT 2-A REM was operated in filtration mode, the k_{obs} for phenol increased by a factor of 2.6 compared to cross-flow mode experiments. These results are attributed to a significant enhancement of the mass-transfer rate of phenol to the REM surface, which thereby allowed the enhanced kinetics of phenol oxidation on the Ti_4O_7 particles to be realized. These results indicate that mass transfer in the cross-flow mode limited the k_{obs} and that filtration mode through a highly porous REM is necessary to realize the high reactivity of these materials. The E/E-ELAT 2-A-2 showed similar kinetics to the E/E-ELAT 2-A, suggesting some mass transport control existed and the change in electroactive surface area between the two materials cited prior did not significantly affect kinetics. By contrast, the SC-ELAT 2-A showed a lower rate

constant for phenol (k_{obs} = 1.85 x 10^{-5} ± 9.10 x 10^{-7} m s^{-1}) compared to the E/E-ELAT 2-A REM (k_{obs} = 2.39 x 10^{-5} ± 1.35 x 10^{-6} m s^{-1}), which is consistent with the CV and EIS results that showed slower kinetics for the $Fe(CN)_6^{4-/3-}$ redox couple (Table 4.3). Results also indicate that the ELAT 2 materials performed better than the ELAT 1 materials when operated in filtration mode, which is attributed to enhanced kinetics on ELAT 2 materials, similar to CV results with the $Fe(CN)_6^{4-/3-}$ redox couple.

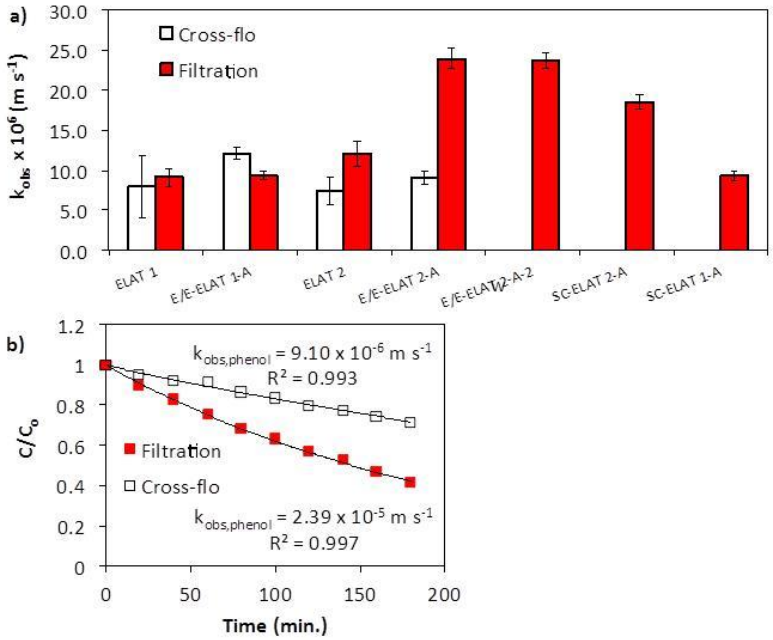

Figure 4.13 (a) Summary of phenol oxidation rate constants, (b) data of phenol versus time for E/E-ELAT 2-A. Solid lines represent model fits. All experiments conducted at 1.0 mA cm^{-2} current density. Cross-flow mode experiments were not conducted for E/E-ELAT 2-A-2, SC-ELAT 2-A, and SC-ELAT 1-A.

Based on the results that indicate the ELAT 2 materials had faster kinetics for the $Fe(CN)_6^{4-/3-}$ redox couple and phenol oxidation relative to the ELAT 1 materials,

additional filtration mode experiments were conducted to determine the effect of current density on phenol oxidation for the ELAT 2 materials. A series of experiments were conducted at various current densities (*i.e.*, 0.2 - 10 mA cm^{-2}) using the ELAT 2-based REM materials (Figure 4.14). The k_{obs} values determined for phenol oxidation were fit with the following equation:

$$k_{obs} = \frac{k_m}{1 + \frac{k_m}{k}} \tag{4.7}$$

$$k = \frac{i}{nFAC_0}\gamma \tag{4.8}$$

where k_{obs} is the normalized observed first-order reaction rate constant (m s^{-1}), k_m is the normalized mass-transport rate constant (m s^{-1}), k is the normalized kinetic rate constant (m s^{-1}), C_0 is the initial phenol concentration (mol m^{-3}), and γ is the fraction of current going towards phenol oxidation. Equation 4.8 implies that the kinetic rate constant increases linearly with the applied current, which has been observed in prior electrochemical studies.[155-156] All other symbols have their usual meanings. Equation 4.7 was fit to the k_{obs} data using least squares regression, where γ = 0.31 and k_m = 1.1 x 10^{-4} m s^{-1} were the best-fit parameter values. As shown in Figure 4.14, the model adequately represents the data, and indicates that k_{obs} for phenol oxidation at 10 mA cm^{-2} for E/E-ELAT 2-A (k_{obs} = 8.0 x 10^{-5} m s^{-1}) and E/E-ELAT 2-A-2 (k_{obs} = 7.5 x 10^{-5} m s^{-1}) were approaching the mass transfer limit. The k_{obs} values for phenol oxidation measured here are 6 to 8 times higher than measured in a previous study that utilized a ceramic Ti_4O_7

REM operated in filtration mode for *p*-substituted phenol oxidation (k_m = 1.0 x 10^{-5} to 1.4 x 10^{-5} m s^{-1}),[12-13] and is comparable to rate constants obtained with carbon nanotube flow-through reactors (1.7 x 10^{-5} to 1.0 x 10^{-4} m s^{-1}), which are among the highest reported in the literature.[75-77]

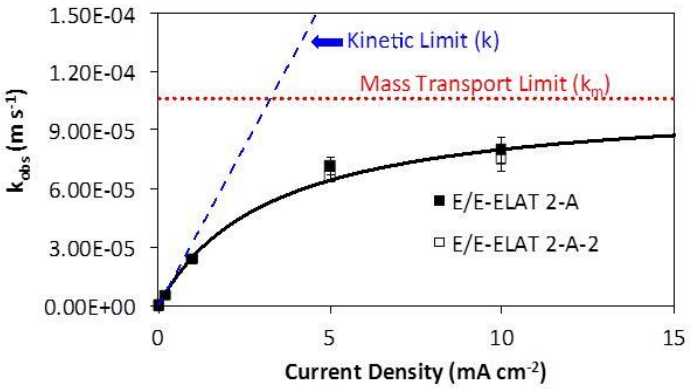

Figure 4.14 Plot of normalized observed rate constant (k_{obs}) for phenol oxidation in the flow-through reactor operated in filtration mode as a function of current density. Solid black line—model fit; Blue dashed line—kinetic limit estimated by model fit to experimental data; red dashed line—mass transport limit (k_m) estimated by model fit to experimental data. Experimental conditions: Anode = ELAT (10 cm^2); Cathode = BDD (10 cm^2); electrolyte: 0.3 L of 100 mM $NaClO_4$; T = 20 °C; Q_{cross} = 25.8 L h^{-1}; J = 6100 L m^{-2} h^{-1}.

Previous work with a ceramic Ti_4O_7 REM operated in filtration mode showed that the rate constants for oxidation of various organic compounds were convection-limited due to the ~ 1.0 micron pore size.[13] Fitting of the k_{obs} values in our experiments with equation 5.7 determined that k_m = 1.1 x 10^{-4} m s^{-1}. The normalized membrane flux (J) through the REM was 1.7 x 10^{-3} m s^{-1} (6100 L m^{-2} h^{-1}), which is an order of magnitude higher than the value determined for k_m. These results suggest that phenol oxidation was

limited by pore diffusion within the REM and not convection to the pore. The diffusion length (δ) was estimated by $\delta = D/k_m$, where D is the diffusion coefficient for phenol ($D = 8.9 \times 10^{-10}$ m^2 s^{-1})[157]. Based on $k_m = 1.1 \times 10^{-4}$ m s^{-1}, a value of $\delta = 8.4$ μm was estimated. The Hg porosimetry data (see Figure 4.9) indicated that the ELAT 2 support has pores on the order of 15 μm. The value of $\delta = 8.4$ μm is almost identical to the average pore radius of 7.5 μm found by Hg porosimetry, and indicates the pore diffusion was controlling phenol oxidation. Additionally, these results indicate that designing REM materials with smaller pore size distributions should result in enhanced removal of contaminants.

4.4 Conclusions

This study synthesized porous, flexible reactive electrochemical membranes (REMs) by a novel simultaneous electrospinning/electrospraying (E/E) technique for use in water treatment applications. REMs consisted of poly(sulfone) (PSU) fibers and Ti_4O_7 particles, supported on an ELAT gas diffusion layer substrate. SEM images of annealed samples showed that the synthesized REMs consisted of well-adhered micron-sized Ti_4O_7 particles to the ELAT substrate. Deposition of the Ti_4O_7 particles using the E/E technique resulted in an enhancement of the kinetics for water electrolysis reactions and the $Fe(CN)_6^{4-/3-}$ redox couple. By contrast, membranes synthesized by a solution cast method did not show kinetic enhancements for these reactions, which was attributed to PSU coverage of the Ti_4O_7 particles. Electrochemical impedance spectroscopy of the optimized REM measured a > 5-fold increase in the surface area normalized rate

constant for the $Fe(CN)_6^{4-/3-}$ redox couple relative to the ELAT support. Membrane filtration experiments showed that operating the REMs in filtration mode resulted in a 2.6-fold enhancement in the observed first-order rate constant for phenol oxidation ($k_{obs,phenol}$) relative to cross-flow operation at a current density of 1.0 mA cm^{-2}. This enhancement was attributed to the increased mass transfer rate that occurred in filtration mode. Phenol oxidation in filtration mode reached a $k_{obs,phenol} = 8.0 \times 10^{-5}$ m s^{-1} at 10 mA cm^{-2}, which was approaching the pore diffusion mass transfer limit, and was 6 to 8 times higher than measured in a previous study that utilized a ceramic Ti_4O_7 REM in filtration mode,[12-13] and is comparable to rate constants obtained with carbon nanotube flow-through reactors (1.7×10^{-5} to 1.0×10^{-4} m s^{-1}), which are among the highest reported in the literature to date.[75,76-77] Results suggest that further rate enhancements can be achieved by synthesizing REMs with smaller pore diameters, which will decrease the time-scale for pore diffusion.

CHAPTER V

CONCLUSIONS AND FUTURE OUTLOOK

5.1 Summary

Understanding and accurately measuring transport mechanisms of liquid water in polymer films and membranes is important for the development of materials used for many applications. In this work, liquid water sorption transport mechanisms in polymer films and membranes, and the development of polymer membranes for water purification was investigated.

The *in situ* pressure-contact FTIR-ATR spectroscopy apparatus developed in this work provided accurate measurement of liquid water diffusion in free-standing polymer films. The measurement of liquid diffusion in free-standing polymer films cannot be accomplished with the conventional time-resolved FTIR-ATR spectroscopy technique, because it requires the polymer film to be solution-cast onto the ATR crystal. Liquid transport in a rubber polymer (PIB) using this apparatus showed similar results to those obtained with the conventional solution-cast FTIR-ATR spectroscopy method, demonstrating the pressure-contact apparatus may be suitable to accurately measure sorption kinetics of liquids in free-standing rubbery polymer films. Non-Fickian behavior was observed for the rubbery (PIB) and glassy (PMMA) polymers in this study, while Fickian behavior was observed for the free-standing crosslinked polymer film. The non-Fickian behavior observed for solution-cast PMMA in this study was due to water diffusion and water-induced polymer relaxation occurring on the same time scale, and

both of these phenomena were modeled and quantified. Non-Fickian behavior observed for free-standing PMMA in this study was attributed to water diffusion and polymer compression. Diffusion-compression had not been observed *via* ATR before and therefore a new mathematical model incorporating both of these phenomena was developed to quantify and model the sorption kinetics observed for free-standing PMMA. The Fickian behavior observed for the crosslinked polymer is attributed to a suppression of the polymer strain response. The results obtained for the crosslinked polymer indicates that the *in situ* pressure-contact apparatus may be a suitable technique for measuring liquid sorption in free-standing films (*e.g.*, commercial films).

Since the nonequilibrium nature of glassy polymers is attributed to their T_g, liquid water diffusion in polymer-ionic liquid mixtures of varying T_gs was investigated. Liquid water diffusion in PMMA-EMIm-TFSI was investigated to determine the effect of T_g on diffusion behavior. This work demonstrated that the addition of ionic liquid lowers the glass transition temperature of the polymer-ionic liquid mixture and changes liquid water diffusion behavior. As the glass transition temperature approached and decreased below the experimental temperature, diffusion behavior became more Fickian. This is attributed to the fact that as T_g decreases, the free volume of the polymer approaches equilibrium.

In this work, porous, flexible reactive electrochemical membranes (REMs) for water treatment applications were synthesized. REMs consisted of poly(sulfone) (PSU) fibers and Ti_4O_7 particles, supported on an ELAT gas diffusion layer substrate, and were successfully synthesized by a novel simultaneous electrospinning/electrospraying (E/E)

technique for use in water treatment applications. The E/E technique resulted in REMs with enhanced reaction kinetics. Additionally, this work demonstrated that operating the REMs in filtration (flow-through) mode resulted in an enhancement of the rate constant for phenol oxidation, and that phenol oxidation is limited by pore diffusion.

5.2 Future Directions

Applications[1-2, 55] for liquid water transport in polymer films and membranes provide multiple opportunities to expand on the work presented in this dissertation. There has been recent interest in supported ionic liquid membranes (SILMs) for gas separations, because of the high CO_2 solubility of ILs, due to their high membrane permeability and good separation performance.[158-161] However, the SILM configuration is limited when the pressure differential across the membrane is larger than the breakthrough value, pushing the liquid phase through the pores of the support material.[55, 161-163] Because of these limitations, the use of polymerized ionic liquids (PILs) has been explored because of their suitability for a large range of operation conditions.[55] Bara *et al.* studied the permeabilities, solubilities, and diffusivities of CO_2, CH_4, and N_2 in various styrene and acrylate based PILs, and found that CO_2/CH_4 separation was favored by both selectivity and diffusivity differences and the PIL membranes could absorb twice as much CO_2 as their liquid and gas counterparts.[56] These results highlight the potential use of PILs for CO_2 separation. Recently, Ansaloni *et al.* synthesized two different imidazolium-based PILs, a homopolymer and a diblock copolymer and investigated the gas transport properties of CO_2, CH_4, N_2 and He over a range of operating parameters to characterize

the effect of water vapor on gas separation performance.[55] They demonstrated that CO_2 permeability increased in both the homopolymer and the diblock copolymer with increasing humidity, with negligible effects on gas solubility.

To better understand the interactions between CO_2 and PILs, transport studies using FTIR-ATR spectroscopy could be performed. CO_2 transport in PMMA-EMIm-TFSI at different concentrations of IL and under different RH conditions can be studied. Currently there have been no studies utilizing FTIR-ATR spectroscopy for the study of CO_2 separations. This would be a novel study because it could provide molecular level data on interactions between CO_2, water vapor, and the polymer-ionic liquid mixture in real time.

In order to better understand the surface interactions occurring on the Ti_4O_7 REMs, a *in situ* pressure-contact apparatus developed in Chapter 2 can be modified to obtain molecular transport, kinetic, and electrochemical data simultaneously. Polymer nanofiber/inorganic particle membranes can be fabricated using simultaneous E/E. Using combined EIS-ATR, the molecular interactions at the REM surface can be studied to obtain data on kinetic and electrochemical mechanisms. Recently work by Richey *et al.* expanded on this work to create a technique to study ion transport in pseudocapacitors and supercapacitors using a spectroelectrochemical technique.[164-165] The apparatus designed by Richey provided a way to study ion transport in samples that were not directly adhered to the ATR element. A similar apparatus could be designed by using a free-standing membrane fabricated *via* simultaneous E/E and a modified version of the *in situ* pressure-contact apparatus developed in Chapter 2.

REFERENCES

1. van der Wel, G. K.; Adan, O. C. G., Moisture in Organic Coatings - A Review. *Prog. Org. Coat.* **1999,** *37* (1-2), 1-14.

2. Rodríguez, O.; Fornasiero, F.; Arce, A.; Radke, C. J.; Prausnitz, J. M., Solubilities and Diffusivities of Water Vapor in Poly(methylmethacrylate), Poly(2-hydroxyethylmethacrylate), Poly(N-vinyl-2-pyrrolidone) and Poly(acrylonitrile). *Polymer* **2003,** *44* (20), 6323-6333.

3. Auras, R.; Harte, B.; Selke, S., An Overview of Polylactides as Packaging Materials. *Macromolecular bioscience* **2004,** *4* (9), 835-64.

4. Williams, C.; Hillmyer, M., Polymers from Renewable Resources: A Perspective for a Special Issue of Polymer Reviews. *Polymer Reviews* **2008,** *48* (1), 1-10.

5. Cath, T.; Childress, A.; Elimelech, M., Forward Osmosis: Principles, Applications, and Recent Developments. *Journal of Membrane Science* **2006,** *281* (1-2), 70-87.

6. Geise, G. M.; Lee, H.-S.; Miller, D. J.; Freeman, B. D.; McGrath, J. E.; Paul, D. R., Water Purification by Membranes: The Role of Polymer Science. *Journal of Polymer Science Part B: Polymer Physics* **2010,** *48* (15), 1685-1718.

7. Langer, R. S.; Peppas, N. A., Present and Future Applications of Biomaterials in Controlled Drug Delivery Systems. *Biomaterials* **1981,** *2* (4), 201-214.

8. Arce, A.; Fornasiero, F.; Rodriguez, O.; Radke, C. J.; Prausnitz, J. M., Sorption and Transport of Water Vapor in Thin Polymer Films at 35 C. *Physical Chemistry Chemical Physics* **2004,** *6* (1), 103.

9. Mauritz, K.; Moore, R., State of Understanding of Nafion. *Chemical reviews* **2004,** *104* (10), 4535-4586.

10. Van der Bruggen, B.; Lejon, L.; Vandecasteele, C., Reuse, treatment, and discharge of the concentrate of pressure-driven membrane processes. *Environmental Science & Technology* **2003,** *37* (17), 3733-3738.

11. Santos, M. C.; Elabd, Y. A.; Jing, Y.; Chaplin, B. P.; Fang, L., Highly Porous Ti4O7 Reactive Electrochemical Water Filtration Membranes Fabricated via Electrospinning/Electrospraying. *AIChE Journal* **2016,** *62* (2), 508-524.

12. Zaky, A. M.; Chaplin, B. P., Mechanism of p-Substituted Phenol Oxidation at a Ti4O7 Reactive Electrochemical Membrane. *Environmental Science & Technology* **2014,** *48* (10), 5857-5867.

13. Zaky, A. M.; Chaplin, B. P., Porous Substoichiometric TiO2 Anodes as Reactive Electrochemical Membranes for Water Treatment. *Environmental Science & Technology* **2013,** *47* (12), 6554-6563.

14. Hancock, B. C.; Zografi, G., The Use of Solution Theories for Predicting Water-Vapor Absorption by Amorphous Pharmaceutical Solids - A Test of the Flory-Huggins and Vrentas Models. *Pharm. Res.* **1993,** *10* (9), 1262-1267.

15. Davis, E. M.; Theryo, G.; Hillmyer, M. A.; Cairncross, R. A.; Elabd, Y. A., Liquid Water Transport in Polylactide Homo and Graft Copolymers. *ACS Appl. Mater. Interfaces* **2011,** *3* (10), 3997-4006.

16. Goodelle, J. P.; Pearson, R. A.; Santore, M. M., Water-Uptake Kinetics in Poly(methyl methacrylate) Films with a Fluorescent Rotor Probe. *Journal of Applied Polymer Science* **2002,** *86* (10), 2463-2471.

17. Davis, E. M.; Benetatos, N. M.; Regnault, W. F.; Winey, K. I.; Elabd, Y. A., The Influence of Thermal History on Structure and Water Transport in Parylene C Coatings. *Polymer* **2011,** *52* (23), 5378-5386.

18. Elabd, Y. A., Ph.D, Dissertation, Johns Hopkins University. **2000**.

19. Elabd, Y. A.; Baschetti, M. G.; Barbari, T. A., Time-Resolved Fourier Transform Infrared/Attenuated Total Reflection Spectroscopy for the Measurement of Molecular Diffusion in Polymers. *Journal of Polymer Science Part B: Polymer Physics* **2003,** *41* (22), 2794-2807.

20. Elabd, Y. A.; Barbari, T. A., Separating Solvation from Molecular Diffusion in Polymers. *Aiche J.* **2001,** *47* (6), 1255-1262.

21. Elabd, Y. A.; Barbari, T. A., Multicomponent Diffusion of Hydrogen-Bonding Solutes in a Polymer. *Aiche J.* **2002,** *48* (8), 1610-1620.

22. Hallinan, D. T.; Elabd, Y. A., Diffusion and Sorption of Methanol and Water in Nafion Using Time-Resolved Fourier Transform Infrared-Attenuated Total Reflectance Spectroscopy. *J. Phys. Chem. B* **2007,** *111* (46), 13221-13230.

23. Hallinan, D. T.; De Angelis, M. G.; Baschetti, M. G.; Sarti, G. C.; Elabd, Y. A., Non-Fickian Diffusion of Water in Nafion. *Macromolecules* **2010,** *43* (10), 4667-4678.

24. Nguyen, T.; Byrd, E.; Bentz, D.; Lin, C. J., In Situ Measurement of Water at the Organic Coating Substrate Interface. *Progress in Organic Coatings* **1996,** *27* (1-4), 181-193.

25. Yi, X.; Pellegrino, J., Diffusion Measurements with Fourier Transform Infrared Attenuated Total Reflectance Spectroscopy: Water Diffusion in Polypropylene. *Journal of Polymer Science Part B: Polymer Physics* **2002,** *40* (10), 980-991.

26. Wang, M.; Wu, P.; Sengupta, S. S.; Chadhary, B. I.; Cogen, J. M.; Li, B., Investigation of Water Diffusion in Low-Density Polyethylene by Attenuated Total Reflectance Fourier Transform Infrared Spectroscopy and Two-Dimensional Correlation Analysis. *Ind. Eng. Chem. Res.* **2011,** *50* (10), 6447-6454.

27. Yi, X. H.; Portnoy, J.; Pellegrino, J., Diffusion Measurements Using ATR-FTIR Spectroscopy: Acetone Diffusion in Polypropylene - Use of Penetrant Fluid Pressure to Improve Sample/IRE Contact. *J. Polym. Sci. Pt. B-Polym. Phys.* **2000,** *38* (13), 1773-1787.

28. Balik, C. M.; Simendinger, W. H., An Attenuated Total Reflectance Cell for Analysis of Small Molecule Diffusion in Polymer Thin Films with Fourier-Tansform Infrared Spectroscopy. *Polymer* **1998,** *39* (20), 4723-4728.

29. Neogi, P., Anomalous Diffusion of Vapors Through Solid Polymers.2. Anomalous Sorption. *Aiche J.* **1983,** *29* (5), 833-839.

30. Frisch, H. L., Sorption and Transport in Glassy Polymers - Review. *Polym. Eng. Sci.* **1980,** *20* (1), 2-13.

31. George, S. C.; Thomas, S., Transport phenomena through polymeric systems. *Prog. Polym. Sci.* **2001,** *26* (6), 985-1017.

32. Sperling, L. H., *Introduction to Physical Polymer Science*. Wiley: 2005.

33. Davis, E. M., Ph.D, Dissertation, Drexel University. **2013**.

34. De Kee, D.; Liu, Q.; Hinestroza, J., Viscoelastic (Non-Fickian) Diffusion. *Can. J. Chem. Eng.* **2005,** *83* (6), 913-929.

35. Turner, D. T., Poly(methyl methacrylate) Plus Water : Sorption Kinetics and Volumetric Changes. *Polymer* **1982,** *23* (2), 197-202.

36. Stannett, V.; Haider, M.; Koros, W. J.; Hopfenberg, H. B., Sorption and Transport of Water-Vapor in Glassy Poly(acrylonitrile). *Polym. Eng. Sci.* **1980,** *20* (4), 300-304.

37. Stannett, V. T.; Ranade, G. R.; Koros, W. J., Characterization of Water-Vapor Transport in Glassy Polyacrylonitrile by Combined Permeation and Sorption Techniques. *J. Membr. Sci.* **1982,** *10* (2-3), 219-233.

38. Hallinan, D. T.; Elabd, Y. A., Diffusion of Water in Nafion Using Time-Resolved Fourier Transform Infrared-Attenuated Total Reflectance Spectroscopy. *J. Phys. Chem. B* **2009,** *113* (13), 4257-4266.

39. Satterfield, M. B.; Benziger, J. B., Non-Fickian Water Vapor Sorption Dynamics by Nafion Membranes. *J. Phys. Chem. B* **2008,** *112* (12), 3693-3704.

40. Majsztrik, P. W.; Satterfield, M. B.; Bocarsly, A. B.; Benziger, J. B., Water Sorption, Desorption and Transport in Nafion Membranes. *J. Membr. Sci.* **2007,** *301* (1-2), 93-106.

41. Davis, E. M.; Minelli, M.; Baschetti, M. G.; Elabd, Y. A., Non-Fickian Diffusion of Water in Polylactide. *Ind. Eng. Chem. Res.* **2013,** *52* (26), 8664-8673.

42. Berens, A. R.; Hopfenberg, H. B., Diffusion and Relaxation in Glassy Polymer Powders .2. Separation of Diffusion and Relaxation Parameters. *Polymer* **1978,** *19* (5), 489-496.

43. Vrentas, J. S.; Jarzebski, C. M.; Duda, J. L., Deborah Number for Diffusion in Polymer-Solvent Systems. *Aiche J.* **1975,** *21* (5), 894-901.

44. Davis, E. M.; Elabd, Y. A., Water Clustering in Glassy Polymers. *J. Phys. Chem. B* **2013,** *117* (36), 10629-10640.

45. Sammon, C.; Mura, C.; Yarwood, J., *J. Phys. Chem. B* **1998,** *102*, 3402.

46. Scatena, L. F.; Brown, M. G.; Richmond, G. L., Water at Hydrophobic Surfaces: Weak Hydrogen Bonding and Strong Orientation Effects. *Science* **2001,** *292* (5518), 908-912.

47. Reiner, M., The Deborah Number. *Phys. Today* **1964,** *17* (1), 62-62.

48. Vrentas, J. S.; Duda, J. L., Diffusion in Polymer-Solvent Systems .3. Construction of Deborah Number Diagrams. *J. Polym. Sci. Pt. B-Polym. Phys.* **1977,** *15* (3), 441-453.

49. Vrentas, J. S.; Vrentas, C. M.; Huang, W. J., Anticipation of Anomalous Effects in Differential Sorption Experiments. *Journal of Applied Polymer Science* **1997,** *64* (10), 2007-2013.

50. Sundfors, F.; Lindfors, T.; Hofler, L.; Bereczki, R.; Gyurcsanyi, R. E., FTIR-ATR Study of Water Uptake and Diffusion through Ion-Selective Membranes

Based on Poly(acrylates) and Silicone Rubber. *Analytical Chemistry* **2009,** *81* (14), 5925-5934.

51. Armand, M.; Endres, F.; MacFarlane, D. R.; Ohno, H.; Scrosati, B., Ionic-liquid materials for the electrochemical challenges of the future. *Nat. Mater.* **2009,** *8* (8), 621-629.

52. Lu, J. M.; Yan, F.; Texter, J., Advanced Applications of Ionic Liquids in Polymer Science. *Prog. Polym. Sci.* **2009,** *34* (5), 431-448.

53. Restolho, J.; Mata, J. L.; Colaço, R.; Saramago, B., Moisture Absorption in Ionic Liquid Films. *The Journal of Physical Chemistry C* **2013,** *117* (20), 10454-10463.

54. Wang, P.; Zakeeruddin, S. M.; Exnar, I.; Gratzel, M., High Efficiency Dye-Sensitized Nanocrystalline Solar Cells Based on Ionic Liquid Polymer Gel Electrolyte. *Chem. Commun.* **2002,** (24), 2972-2973.

55. Ansaloni, L.; Nykaza, J. R.; Ye, Y.; Elabd, Y. A.; Giacinti Baschetti, M., Influence of Water Vapor on the Gas Permeability of Polymerized Ionic Liquids Membranes. *J. Membr. Sci.* **2015,** *487*, 199-208.

56. Bara, J. E.; Lessmann, S.; Gabriel, C. J.; Hatakeyama, E. S.; Noble, R. D.; Gin, D. L., Synthesis and Performance of Polymerizable Room-Temperature Ionic Liquids as Gas Separation Membranes. *Ind. Eng. Chem. Res.* **2007,** *46* (16), 5397-5404.

57. Gwee, L.; Choi, J.-H.; Winey, K. I.; Elabd, Y. A., Block Copolymer/Ionic Liquid Films: The Effect of Ionic Liquid Composition on Morphology and Ion Conduction. *Polymer* **2010,** *51* (23), 5516-5524.

58. Magana, S.; Gain, O.; Gouanvé, F.; Espuche, E., Influence of Different Alkyl-methylimidazolium Tetrafluoroborate Ionic Liquids on the Structure of Pebax® Films. Consequences on Thermal, Mechanical, and Water Sorption and Diffusion Properties. *Journal of Polymer Science Part B: Polymer Physics* **2016,** *54* (8), 811-824.

59. Ansaloni, L.; Minelli, M.; Baschetti, M. G.; Sarti, G. C., Effect of relative humidity and temperature on gas transport in Matrimie (R): Experimental study and modeling. *J. Membr. Sci.* **2014,** *471*, 392-401.

60. Chen, G. Q.; Scholes, C. A.; Qiao, G. G.; Kentish, S. E., Water vapor permeation in polyimide membranes. *J. Membr. Sci.* **2011,** *379* (1-2), 479-487.

61. Catalano, J.; Myezwa, T.; De Angelis, M. G.; Baschetti, M. G.; Sarti, G. C., The effect of relative humidity on the gas permeability and swelling in PFSI membranes. *Int. J. Hydrog. Energy* **2012,** *37* (7), 6308-6316.

62. Baschetti, M. G.; Minelli, M.; Catalano, J.; Sarti, G. C., Gas permeation in perflurosulfonated membranes: Influence of temperature and relative humidity. *Int. J. Hydrog. Energy* **2013,** *38* (27), 11973-11982.

63. Martinez-Huitle, C. A.; Ferro, S., Electrochemical Oxidation of Organic Pollutants for the Wastewater Treatment: Direct and Indirect Processes. *Chemical Society Reviews* **2006,** *35* (12), 1324-1340.

64. Shannon, M. A.; Bohn, P. W.; Elimelech, M.; Georgiadis, J. G.; Marinas, B. J.; Mayes, A. M., Science and Technology for Water Purification in the Coming Decades. *Nature* **2008,** *452* (7185), 301-310.

65. Yang, Y.; Wang, H.; Li, J. X.; He, B. Q.; Wang, T. H.; Liao, S. J., Novel Functionalized Nano-TiO2 Loading Electrocatalytic Membrane for Oily Wastewater Treatment. *Environmental Science & Technology* **2012,** *46* (12), 6815-6821.

66. Chaplin, B. P., Critical Review of Electrochemical Advanced Oxidation Processes for Water Treatment Applications. *Environ Sci Process Impacts* **2014,** *16* (6), 1182-203.

67. Sharifian, H.; Kirk, D. W., Electrochemical Oxidation of Phenol. *J. Electrochem. Soc.* **1986,** *133* (5), 921-924.

68. de Sucre, V. S.; Watkinson, A. P., Anodic Oxidation of Phenol for Waste Water Treatment. *The Canadian Journal of Chemical Engineering* **1981,** *59* (1), 52-59.

69. Murphy, O. J.; Hitchens, G. D.; Kaba, L.; Verostko, C. E., Direct Electrochemical Oxidation of Organics for Waste-water Treatment. *Water Research* **1992,** *26* (4), 443-451.

70. Yang, Y.; Li, J.; Wang, H.; Song, X.; Wang, T.; He, B.; Liang, X.; Ngo, H. H., An electrocatalytic membrane reactor with self-cleaning function for industrial wastewater treatment. *Angewandte Chemie* **2011,** *50* (9), 2148-50.

71. Pollock, R. J.; Houlihan, J. F.; Bain, A. N.; Coryea, B. S., Electrochemical Properties of a New Electrode Material, Ti4O7. *Materials Research Bulletin* **1984,** *19* (1), 17-24.

72. Li, X. X.; Zhu, A. L.; Qu, W.; Wang, H. J.; Hui, R.; Zhang, L.; Zhang, J. J., Magneli Phase Ti4O7 Electrode for Oxygen Reduction Reaction and its

Implication for Zinc-Air Rechargeable Batteries. *Electrochimica Acta* **2010,** *55* (20), 5891-5898.

73. Senevirathne, K.; Hui, R.; Campbell, S.; Ye, S.; Zhang, J., Electrocatalytic Activity and Durability of Pt/NbO2 and Pt/Ti4O7 Nanofibers for PEM Fuel Cell Oxygen Reduction Reaction. *Electrochimica Acta* **2012,** *59*, 538-547.

74. Hayfield, P. C. S.; Chemistry, R. S. o., *Development of a New Material: Monolithic Ti4O7 Ebonex Ceramic*. Royal Society of Chemistry: 2002.

75. Yang, J.; Wang, J.; Jia, J. P., Improvement of Electrochemical Wastewater Treatment through Mass Transfer in a Seepage Carbon Nanotube Electrode Reactor. *Environmental Science & Technology* **2009,** *43* (10), 3796-3802.

76. Tsierkezos, N. G.; Ritter, U., Electrochemical and thermodynamic properties of hexacyanoferrate(II)/(III) redox system on multi-walled carbon nanotubes. *J. Chem. Thermodyn.* **2012,** *54*, 35-40.

77. Schnoor, M. H.; Vecitis, C. D., Quantitative Examination of Aqueous Ferrocyanide Oxidation in a Carbon Nanotube Electrochemical Filter: Effects of Flow Rate, Ionic Strength, and Cathode Material. *J. Phys. Chem. C* **2013,** *117* (6), 2855-2867.

78. Pereira, M. R.; Yarwood, J., ATR-FTIR Spectroscopic Studies of the Structure and Permeability of Sulfonated Poly(ether sulfone) Membranes .1. Interfacial Water-Polymer Interactions. *J. Chem. Soc.-Faraday Trans.* **1996,** *92* (15), 2731-2735.

79. Pereira, M. R.; Yarwood, J., ATR-FTIR Spectroscopic Studies of the Structure and Permeability of Sulfonated Poly(ether sulfone) Membranes .2. Water Diffusion Processes. *J. Chem. Soc.-Faraday Trans.* **1996,** *92* (15), 2737-2743.

80. Sammon, C.; Everall, N.; Yarwood, J., The Diffusion of Water into PET Followed In-Situ Using FT-IR ATR. *Macromol. Symp.* **1997,** *119*, 189-196.

81. Sammon, C.; Mura, C.; Yarwood, J.; Everall, N.; Swart, R.; Hodge, D., FTIR-ATR Studies of the Structure and Dynamics of Water Molecules in Polymeric Matrixes. A Comparison of PET and PVC. *J. Phys. Chem. B* **1998,** *102* (18), 3402-3411.

82. Sammon, C.; Yarwood, J.; Everall, N., A FTIR-ATR Study of Liquid Diffusion Processes in PET Films: Comparison of Water with Simple Alcohols. *Polymer* **2000,** *41* (7), 2521-2534.

83. Pogany, G. A., Anomalous Diffusion of Water in Glassy Polymers. *Polymer* **1976,** *17* (8), 690-694.

84. (MIL)-DTL-53022E, Primer, Epoxy Coating, Corrosion Inhibiting, Lead and Chromate Free. 2012.

85. Walch, E.; Gaymans, R. J., Telechelic Polyisobutylene with Unsaturated End-Groups and with Anhydride End-Groups. *Polymer* **1994,** *35* (8), 1774-1778.

86. McNally, G. M., The Effect of PIB Molecular Weight on the Cling Characteristics of Polyethylene-PIB Films for Stretch and Cling Film Applications. *Journal of Plastic Film and Sheeting* **2005,** *21* (1), 55-68.

87. Storey, R. F.; Donnalley, A. B.; Maggio, T. L., Real-Time Monitoring of Carbocationic Polymerization of Isobutylene Using In Situ FTIR-ATR Spectroscopy with Conduit and Diamond-Composite Sensor Technology. *Macromolecules* **1998,** *31* (5), 1523-1526.

88. Gao, Y. F.; Liang, X. D.; Yan, Z. P.; Wang, J. F.; Liu, Y. Y., Study on the Model Selection of Water Diffusion into Silicone Rubber by NMR and Gravimetric Technique. In *2014 Ieee Conference on Electrical Insulation and Dielectric Phenomena*, Ieee: New York, 2014; pp 433-436.

89. Gao, Y. F.; Liang, X. D.; Wang, J. F.; Yan, Z. P.; Liu, Y. Y.; Cai, Y. J., A Capacitance Study of Anomalous Diffusion of Water into HTV Silicone Rubber Materials. *IEEE Trns. Dielectr. Electr. Insul.* **2016,** *23* (1), 368-376.

90. Fieldson, G. T.; Barbari, T. A., The Use of FT.I.R.-A.T.R. Spectroscopy to Characterize Penetrant Diffusion in Polymers. *Polymer* **1993,** *34* (6), 1146-1153.

91. Sutandar, P.; Ahn, D. J.; Franses, E. I., FTIR ATR Analysis For Microstructure And Water-Uptake In Poly(methylmethacrylate) Spin Cast And Langmuir-Blodgett Thin-Films. *Macromolecules* **1994,** *27* (25), 7316-7328.

92. Rajendran, S.; Kannan, R.; Mahendran, O., An Electrochemical Investigation on PMMA/PVdF Blend-Based Polymer Electrolytes. *Materials Letters* **2001,** *49* (3-4), 172-179.

93. Yang, Y.; Dan, Y., Preparation of PMMA/SiO2 Composite Particles via Emulsion Polymerization. *Colloid Polym Sci* **2003,** *281* (8), 794-799.

94. Rajendran, S.; Uma, T., Effect of Ceramic Oxide on PMMA Based Polymer Electrolyte Systems. *Materials Letters* **2000,** *45* (3–4), 191-196.

95. Rajendran, S.; Kannan, R.; Mahendran, O., Ionic Conductivity Studies in Poly(methylmethacrylate)-Polyethlene Oxide Hybrid Polymer Electrolytes with Lithium Salts. *Journal of Power Sources* **2001,** *96* (2), 406-410.

96. Rajendran, S.; Uma, T., Lithium Ion Conduction in PVC-LiBF4 Electrolytes Gelled with PMMA. *Journal of Power Sources* **2000,** *88* (2), 282-285.

97. Willis, H. A.; Zichy, V. J. I.; Hendra, P. J., Laser-Raman and Infra-Red Spectra of Poly(methylmethacrylate). *Polymer* **1969,** *10* (9), 737-&.

98. Ramesh, S.; Leen, K. H.; Kumutha, K.; Arof, A. K., FTIR Studies of PVC/PMMA Blend Based Polymer Electrolytes. *Spectrochimica Acta Part A: Molecular and Biomolecular Spectroscopy* **2007,** *66* (4–5), 1237-1242.

99. Emmons, E. D.; Kraus, R. G.; Duvvuri, S. S.; Thompson, J. S.; Covington, A. M., High-Pressure Infrared Absorption Spectroscopy of Poly(methyl methacrylate). *Journal of Polymer Science Part B: Polymer Physics* **2007,** *45* (3), 358-367.

100. Shao, L.; Samseth, J.; Hagg, M.-B., Crosslinking High Free Volume Polymers - Effect on Gas Separation Properties. *MRS Proceedings* **2007,** *1006*.

101. Davis, E. M.; Elabd, Y. A., Prediction of Water Solubility in Glassy Polymers Using Nonequilibrium Thermodynamics. *Ind. Eng. Chem. Res.* **2013,** *52* (36), 12865-12875.

102. Berens, A. R.; Hopfenberg, H. B., Diffusion and relaxation in glassy polymer powders: 2. Separation of diffusion and relaxation parameters. *Polymer* **1978,** *19* (5), 489-496.

103. Barrer, R. M.; Barrie, J. A., Sorption and Diffusion in Ethyl Cellulose. 4. Water in Ethyl Cellulose. *Journal of Polymer Science* **1958,** *28* (117), 377-386.

104. Schult, K. A.; Paul, D. R., Water sorption and transport in blends of poly(vinyl pyrrolidone) and polysulfone. *J. Polym. Sci. Pt. B-Polym. Phys.* **1997,** *35* (4), 655-674.

105. Schult, K. A.; Paul, D. R., Water sorption and transport in blends of polyethyloxazoline and polyethersulfone. *J. Polym. Sci. Pt. B-Polym. Phys.* **1997,** *35* (6), 993-1007.

106. Sa'adun, N. N.; Subramaniam, R.; Kasi, R., Development and Characterization of Poly(1-vinylpyrrolidone-co-vinyl acetate) Copolymer Based Polymer Electrolytes. *The Scientific World Journal* **2014,** *2014*, 7.

107. Kiefer, J.; Fries, J.; Leipertz, A., Experimental Vibratnional Study of Imidazolium-Based Ionic Liquids: Raman and Infrared Spectra of 1-Ethyl-3-methylimidazolium bis(trifluoromethylsulfonyl)imide and 1-Ethyl-3-methylimidazolium Ethylsulfate. *Applied Spectroscopy* **2007,** *61* (12), 1306-1311.

108. Liang, G., Ph.D, Dissertation, Drexel University. **2010**.

109. Sharick, S.; Koski, J.; Riggleman, R. A.; Winey, K. I., Isolating the Effect of Molecular Weight on Ion Transport of Non Ionic Diblock Copolymer/lonic Liquid Mixtures. *Macromolecules* **2016,** *49* (6), 2245-2256.

110. Hayfield, P. C. S., *Development of a New Material - Monolithic Ti4O7 Ebonex Ceramic*. Royal Society of Chemistry: Cambridge, UK, 2002.

111. Senevirathne, K.; Hui, R.; Campbell, S.; Ye, S. Y.; Zhang, J. J., Electrocatalytic activity and durability of Pt/NbO2 and Pt/Ti4O7 nanofibers for PEM fuel cell oxygen reduction reaction. *Electrochimica Acta* **2012,** *59*, 538-547.

112. Kao, W. H.; Patel, P.; Haberichter, S. L., Formation enhancement of a lead/acid battery positive plate by barium metaplumbate and Ebonex (vol 144, pg 1907, 1997). *J. Electrochem. Soc.* **1997,** *144* (8), 2942-2942.

113. Loyns, A. C.; Hill, A.; Ellis, K. G.; Partington, T. J.; Hill, J. M., Bipolar batteries based on Ebonex (R) technology. *J. Power Sources* **2005,** *144* (2), 329-337.

114. Chen, G. Y.; Bare, S. R.; Mallouk, T. E., Development of Supported Bifunctional Electrocatalysts for Unitized Regenerative Fuel Cells. *J. Electrochem. Soc.* **2002,** *149* (8), A1092-A1099.

115. Ioroi, T.; Senoh, H.; Yamazaki, S. I.; Siroma, Z.; Fujiwara, N.; Yasuda, K., Stability of Corrosion-Resistant Magneli-Phase Ti4O7-Supported PEMFC Catalysts at High Potentials. *J. Electrochem. Soc.* **2008,** *155* (4), B321-B326.

116. Phillips, R.; Hansen, P.; Eisenbraun, E., Atomic Layer Deposition Fabricated Substoichiometric TiOx Nanorods as Fuel Cell Catalyst Supports. *J. Vac. Sci. Technol. A* **2012,** *30* (1), 6.

117. Chen, G.; Betterton, E. A.; Arnold, R. G., Electrolytic Oxidation of Trichloroethylene Using a Ceramic Anode. *J. Appl. Electrochem.* **1999,** *29* (8), 961-970.

118. El-Sherif, S.; Bejan, D.; Bunce, N. J., Electrochemical Oxidation of Sulfide Ion in Synthetic Sour Brines Using Periodic Polarity Reversal at Ebonex((R)) Electrodes. *Can. J. Chem.-Rev. Can. Chim.* **2010,** *88* (9), 928-936.

119. Kearney, D.; Bejan, D.; Bunce, N. J., The Use of Ebonex Electrodes for the Electrochemical Removal of Nitrate Ion from Water. *Can. J. Chem.-Rev. Can. Chim.* **2012,** *90* (8), 666-674.

120. Bejan, D.; Malcolm, J. D.; Morrison, L.; Bunce, N. J., Mechanistic Investigation of the Conductive Ceramic Ebonex (R) as an Anode Material. *Electrochimica Acta* **2009,** *54* (23), 5548-5556.

121. Bejan, D.; Guinea, E.; Bunce, N. J., On the Nature of the Hydroxyl Radicals Produced at Boron-Doped Diamond and Ebonex (R) Anodes. *Electrochimica Acta* **2012,** *69*, 275-281.

122. Scialdone, O.; Galia, A.; Filardo, G., Electrochemical Incineration of 1,2-Dichloroethane: Effect of the Electrode Material. *Electrochimica Acta* **2008,** *53* (24), 7220-7225.

123. Yanilmaz, M.; Lu, Y.; Dirican, M.; Fu, K.; Zhang, X. W., Nanoparticle-on-Nanofiber Hybrid Membrane Separators for Lithium-Ion Batteries via Combining Electrospraying and Electrospinning Techniques. *Journal of Membrane Science* **2014,** *456*, 57-65.

124. Wang, K.; Xu, M.; Zhu, M. F.; Su, H.; Wang, H. J.; Kong, D. L.; Wang, L. Y., Creation of Macropores in Electrospun Silk Fibroin Scaffolds Using Sacrificial PEO-Microparticles to Enhance Cellular Infiltration. *Journal of Biomedical Materials Research Part A* **2013,** *101* (12), 3474-3481.

125. Virovska, D.; Paneva, D.; Manolova, N.; Rashkov, I.; Karashanova, D., Electrospinning/Electrospraying vs. Electrospinning: A Comparative Study on the Design of Poly(L-lactide)/Zinc Oxide Non-Woven Textile. *Appl. Surf. Sci.* **2014,** *311*, 842-850.

126. Thayer, P. S.; Dimling, A. F.; Plessl, D. S.; Hahn, M. R.; Guelcher, S. A.; Dahlgren, L. A.; Godstein, A. S., Cellularized Cylindrical Fiber/Hydrogel Composites for Ligament Tissue Engineering. *Biomacromolecules* **2014,** *15* (1), 75-83.

127. Ignatova, M.; Manolova, N.; Rashkov, I., Electrospun Antibacterial Chitosan-Based Fibers. *Macromolecular Bioscience* **2013,** *13* (7), 860-872.

128. Bock, N.; Woodruff, M. A.; Steck, R.; Hutmacher, D. W.; Farrugia, B. L.; Dargaville, T. R., Composites for Delivery of Therapeutics: Combining Melt Electrospun Scaffolds with Loaded Electrosprayed Microparticles. *Macromol Biosci* **2014,** *14* (2), 202-14.

129. Bae, H.; Lee, J., Encapsulated Particles Attached on Electrospun Fibers by In Situ Combination of Electrospinning and Coaxial Electrospraying. *Journal of Nanoscience and Nanotechnology* **2014,** *14* (10), 7574-7580.

130. Wang, X.; Richey, F. W.; Wujcik, K. H.; Ventura, R.; Mattson, K.; Elabd, Y. A., Effect of Polytetrafluoroethylene on Ultra-Low Platinum Loaded Electrospun/Electrosprayed Electrodes in Proton Exchange Membrane Fuel Cells. *Electrochimica Acta* **2014,** *139*, 217-224.

131. Wang, X.; Richey, F. W.; Wujcik, K. H.; Elabd, Y. A., Ultra-Low Platinum Loadings in Polymer Electrolyte Membrane Fuel Cell Electrodes Fabricated via Simultaneous Electrospinning/Electrospraying Method. *Journal of Power Sources* **2014,** *264*, 42-48.

132. Lavielle, N.; Hebraud, A.; Schlatter, G.; Thony-Meyer, L.; Rossi, R. M.; Popa, A. M., Simultaneous Electrospinning and Electrospraying: A Straightforward Approach for Fabricating Hierarchically Structured Composite Membranes. *Acs Applied Materials & Interfaces* **2013,** *5* (20), 10090-10097.

133. Korina, E.; Stoilova, O.; Manolova, N.; Rashkov, I., Poly(3-hydroxybutyrate)-Based Hybrid Materials with Photocatalytic and Magnetic Properties Prepared by Electrospinning and Electrospraying. *Journal of Materials Science* **2014,** *49* (5), 2144-2153.

134. Ding, Y. C.; Wu, Q.; Zhao, D.; Ye, W.; Hanif, M.; Hou, H. Q., Flexible PI/BaTiO3 Dielectric Nanocomposite Fabricated by Combining Electrospinning and Electrospraying. *European Polymer Journal* **2013,** *49* (9), 2567-2571.

135. Lombardi, M.; Palmero, P.; Sangermano, M.; Varesano, A., Electrospun Polyamide-6 Membranes Containing Titanium Dioxide as Photocatalyst. *Polymer International* **2011,** *60* (2), 234-239.

136. An, S.; Lee, M. W.; Joshi, B. N.; Jo, A.; Jung, J.; Yoon, S. S., Water Purification and Toxicity Control of Chlorophenols by 3D Nanofiber Membranes Decorated with Photocatalytic Titania Nanoparticles. *Ceramics International* **2014,** *40* (2), 3305-3313.

137. Roso, M.; Sundarrajan, S.; Pliszka, D.; Ramakrishna, S.; Modesti, M., Multifunctional Membranes Based on Spinning Technologies: The Synergy of Nanofibers and Nanoparticles. *Nanotechnology* **2008,** *19* (28), 285707.

138. Nabe, A.; Staude, E.; Belfort, G., Surface modification of polysulfone ultrafiltration membranes and fouling by BSA solutions. *J. Membr. Sci.* **1997,** *133* (1), 57-72.

139. Zodrow, K.; Brunet, L.; Mahendra, S.; Li, D.; Zhang, A.; Li, Q. L.; Alvarez, P. J. J., Polysulfone ultrafiltration membranes impregnated with silver nanoparticles show improved biofouling resistance and virus removal. *Water Res.* **2009,** *43* (3), 715-723.

140. Chakrabarty, B.; Ghoshal, A. K.; Purkait, M. K., Ultrafiltration of stable oil-in-water emulsion by polysulfone membrane. *J. Membr. Sci.* **2008,** *325* (1), 427-437.

141. Lima, A. A.; Montalvao, A. F.; Dezotti, M.; Sant'Anna, G. L., Ozonation of a Complex Industrial Effluent: Oxidation of Organic Pollutants and Removal of Toxicity. *Ozone-Science & Engineering* **2006,** *28* (1), 3-8.

142. Li, G. Y.; An, T. C.; Chen, J. X.; Sheng, G. Y.; Fu, J. M.; Chen, F. Z.; Zhang, S. Q.; Zhao, H. J., Photoelectrocatalytic Decontamination of Oilfield Produced Wastewater Containing Refractory Organic Pollutants in the Presence of High Concentration of Chloride Ions. *Journal of Hazardous Materials* **2006,** *138* (2), 392-400.

143. Westerhoff, P.; Moon, H.; Minakata, D.; Crittenden, J., Oxidation of Organics in Retentates from Reverse Osmosis Wastewater Reuse Facilities. *Water Research* **2009,** *43* (16), 3992-3998.

144. Buxton, G. V.; Greenstock, C. L.; Helman, W. P.; Ross, A. B., Critical-Review of Rate Constants for Reactions of Hydrated Electrons, Hydrogen-Atoms and Hydroxyl Radicals (.OH/.O-) in Aqueous Solution. *J. Phys. Chem. Ref. Data* **1988,** *17* (2), 513-886.

145. Goldschmidt, D.; Watanabe, M., X-Ray Diffraction of Polycrystalline Ti4O7. *Materials Research Bulletin* **1985,** *20* (1), 65-70.

146. Andersson, S.; Jahnberg, L., Crystal Structure Studies on HOmologous Series TinO2n-1 VnO2n-1 + Tin-2 Cr2O2n-1. *Arkiv for Kemi* **1964,** *21* (5), 413-&.

147. Lepage, Y.; Strobel, P., Structural Chemistryof Magneli Phases TinO2n-1(4 <n<9).1. Cell and Structure Comparisons. *Journal of Solid State Chemistry* **1982,** *43* (3), 314-319.

148. Li, D.; Xia, Y., Electrospinning of Nanofibers: Reinventing the Wheel? *Advanced Materials* **2004,** *16* (14), 1151-1170.

149. Walsh, F. C.; Wills, R. G. A., The Continuing Development of Magneli Phase Titanium Sub-Oxides and Ebonex (R) Electrodes. *Electrochimica Acta* **2010,** *55* (22), 6342-6351.

150. Bard, A. J.; Faulkner, L. R., *Electrochemical Methods: Fundamentals and Applications*. 2nd ed.; Wiley: New York, 2000.

151. Tremblay, M. L.; Martin, M. H.; Lebouin, C.; Lasia, A.; Guay, D., Determination of the Real Surface Area of Powdered Materials in Cavity Microelectrodes by Electrochemical Impedance Spectroscopy. *Electrochimica Acta* **2010,** *55* (21), 6283-6291.

152. Shi, H., Activated Carbons and Double Layer Capacitance. *Electrochimica Acta* **1996,** *41* (10), 1633-1639.

153. Frackowiak, E.; Beguin, F., Carbon Materials for the Electrochemical Storage of Energy in Capacitors. *Carbon* **2001,** *39* (6), 937-950.

154. Bard, A. J.; Faulkner, L. R., *Electrochemical Methods: Fundamentals and Applications*. Second ed.; John Wiley and Sons: 2001; p 833.

155. Canizares, P.; Garcia-Gomez, J.; Lobato, J.; Rodrigo, M. A., Modeling of Wastewater Electro-Oxidation Processes Part I. General Description and Application to Inactive Electrodes. *Ind. Eng. Chem. Res.* **2004,** *43* (9), 1915-1922.

156. Chaplin, B. P.; Schrader, G.; Farrell, J., Electrochemical Destruction of N-Nitrosodimethylamine in Reverse Osmosis Concentrates using Boron-doped Diamond Film Electrodes. *Environmental Science & Technology* **2010,** *44* (11), 4264-4269.

157. Haynes, W. M., *CRC Handbook of Chemistry and Physics, 91st Edition*. 91st ed.; Taylor & Francis: Boca Raton, FL, 2010.

158. Hanioka, S.; Maruyama, T.; Sotani, T.; Teramoto, M.; Matsuyama, H.; Nakashima, K.; Hanaki, M.; Kubota, F.; Goto, M., CO2 Separation Facilitated by Task-Specific Ionic Liquids Using a Supported Liquid Membrane. *J. Membr. Sci.* **2008,** *314* (1-2), 1-4.

159. Hasib-ur-Rahman, M.; Siaj, M.; Larachi, F., Ionic Liquids for CO2 Capture-Development and Progress. *Chem. Eng. Process.* **2010,** *49* (4), 313-322.

160. Bates, E. D.; Mayton, R. D.; Ntai, I.; Davis, J. H., CO2 Capture by a Task-Specific Ionic Liquid. *Journal of the American Chemical Society* **2002,** *124* (6), 926-927.

161. Scovazzo, P., Determination of the Upper Limits, Benchmarks, and Critical Properties for Gas Separations Using Stabilized Room Temperature Ionic Liquid

Membranes (SILMs) for the Purpose of Guiding Future Research. *J. Membr. Sci.* **2009,** *343* (1-2), 199-211.

162. Bara, J. E.; Hatakeyama, E. S.; Gin, D. L.; Noble, R. D., Improving CO2 Permeability in Polymerized Room-Remperature Ionic Liquid Gas Separation Membranes Through the Formation of a Solid Composite with a Room-Temperature Ionic Liquid. *Polym. Adv. Technol.* **2008,** *19* (10), 1415-1420.

163. Neves, L. A.; Crespo, J. G.; Coelhoso, I. M., Gas Permeation Studies in Supported Ionic Liquid Membranes. *J. Membr. Sci.* **2010,** *357* (1-2), 160-170.

164. Richey, F. W.; Elabd, Y. A., In Situ Molecular Level Measurements of Ion Dynamics in an Electrochemical Capacitor. *J. Phys. Chem. Lett.* **2012,** *3* (22), 3297-3301.

165. Richey, F. W.; Dyatkin, B.; Gogotsi, Y.; Elabd, Y. A., Ion Dynamics in Porous Carbon Electrodes in Supercapacitors Using In Situ Infrared Spectroelectrochemistry. *J Am Chem Soc* **2013,** *135* (34), 12818-26.